UNIVERSITAT POLITÈCNICA DE CATALUNYA

Laboratory of Photonics
Electromagnetics and Photonics Engineering group
Dept. of Signal Theory and Communications

OPTICAL SOLITONS IN QUADRATIC NONLINEAR MEDIA AND APPLICATIONS TO ALL-OPTICAL SWITCHING AND ROUTING DEVICES

Autor: María Concepción Santos Blanco
Director: Lluís Torner

Barcelona, january 1998

Chapter 6

Applications to Soliton Steering

Previous chapters as primarily dealing with description of the basic features of soliton propagation in $\chi^{(2)}$ structures, although often relying on numerical simulations, have mainly put the emphasis on rather theoretical aspects aiming basically at providing a complete basic knowledge of the solitary waves existing in those structures and the characteristics of their excitation. This theoretical description has set the basis for the design of practical setups that exploit the properties of solitary wave propagation along with those of quadratically nonlinear media. Sky is the limit when thinking of applications in which solitary wave propagation excited with low input powers in materials of current use in optical technology is susceptible of improving the present state of the art in optical applications. Quadratic nonlinearities further offer the opportunity of spatial two-dimensional confinement which opens the door to a bunch of applications to the routing and steering in bulk materials such as for example interconnection matrixes.

Optical beam steering is the issue in this Thesis and therefore, practical setups which take advantage of the properties of solitary waves arising in $\chi^{(2)}$ structures for the steering control of optical beams will be analyzed in the present Chapter. Two-dimensional (2+1) geometries might be more interesting from the stand point of practical applications because of the versatility they offer and also for the greater simplicity of the setups required. However, integrated devices, which are the ultimate goal, require (1+1) configurations. In addition to that, the primary interest here is set on identifying effects and possibilities with emphasis lied on providing a basic understanding of the phenomena arising in the propagation along with assessment of the impact of the various parameters involved. Hence, the simpler even though qualitatively retaining the

main features of the nonlinear propagation one-dimensional (1+1) case is considered in the analysis.

Extensive numerical simulations centered in the more relevant from a practical viewpoint situations, serve to asses the potential for the steering control of these special nonlinear modes of the system. With the focus on providing useful guidelines to consider in the design of practical steering devices, optimum performance conditions as well as practical limitations will be identified. Attention will be payed to dependences upon system and input parameters taking into account the two fold character of the problem, namely on one side robustness before eventual slight deviations of the parameters from their nominal values is checked out setting down the problem about *tolerances*, and in the other side dependences upon system and input parameters are evaluated for functioning as *controls* of the propagation.

First section exploits the properties of walking solitons identified and analyzed in chapter 5 to achieve power controlled steering using only the fundamental field as input.

Second section deals with steering accomplished by means of incident tilted beams upon the waveguide while third section is devoted to analysis of the possibilities to perform steering control through phase modulation of the input beams accomplished by phase gratings placed at the input face of the guide.

Finally the input beam break up into solitons travelling in different directions produced inside the nonlinear waveguide in selected cases, is studied and discussed through analysis of the dynamics, and its implications for the design of power activated beam splitters are assessed.

6.1 Power dependent Poynting vector walk-off steering

6.1.1 Numerical experiments

As a consequence of birefringence inherently attached to the quadratic nonlinear response, the wave interaction in $\chi^{(2)}$ crystals typically involves extraordinary waves which with exception of on- axis and off-optical axis incidence feature distinct propagation angles for the constant phase planes and the energy flow. The degree of freedom provided by the angle of the extraordinary electric field vector is often taken advantage of to adjust the wavevector mismatch so that a certain amount of walk-off needs to be tolerated. Recalling that the transverse velocity

163

of the soliton eventually emerging from the input fields can be expressed in the spatial case approximately as

$$v \simeq \frac{\mathcal{J}}{I} - \delta \frac{I_2}{I}. \tag{6.1}$$

Even when no initial momentum is introduced into the system the soliton is expected to walk the z axis off with transverse velocity which in addition to the walk-off parameter depends upon the energy that through the dynamics is allotted to the second harmonic, namely

$$v \simeq -\delta \frac{I_2}{I}. \tag{6.2}$$

Being the energy into the second harmonic not conserved, the output position of the soliton depends on the initial conditions. This is the sought after effect, and experimental evidence of this possibility has been obtained by Torruellas et al. [119]. The focus in this section will hence be on identifying the dependences of such an steering upon input parameters in order to investigate which are the chances for an efficient steering control. Tolerances about other parameters in the system such as the wavevector mismatch as well as to slight variations of the walk-off parameter from its nominal value will be evaluated. Figure 6-1 features a sketch of the practical setup. Thinking on practical applications, attention will be primarily focused in analyzing the case in which only the fundamental field is input, although the effect of a second harmonic injected will also be investigated. For good energy efficiency that entails consideration of positive wavevector mismatch setups.

Figure 6-2 illustrates the process by which ordinary fundamental and extraordinary second harmonic waves which in a linear medium would propagate in different directions become trapped by virtue of the nonlinear interaction forming a solitary wave walking the z axis off at an intermediate angle.

These results have been obtained by integrating (2.94) by means of a split-step Fourier method. The normalized propagation length considered $\xi = 20$, corresponds to about 40 diffraction lengths which for a working wavelength of $\lambda \sim 1 \mu m$ and a typical beam width of $\eta \sim 15 \mu m$ yields a waveguide length of about $L \sim 2.8 cm$ which is in the range of the practically feasible lengths of $\chi^{(2)}$ materials samples.

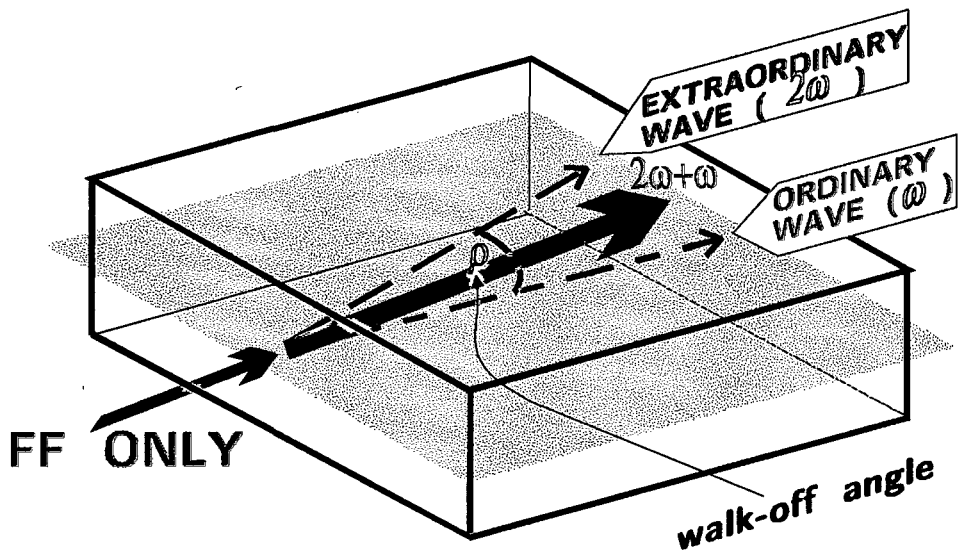A positive walk-off value causes the second harmonic energy as it is generated from the

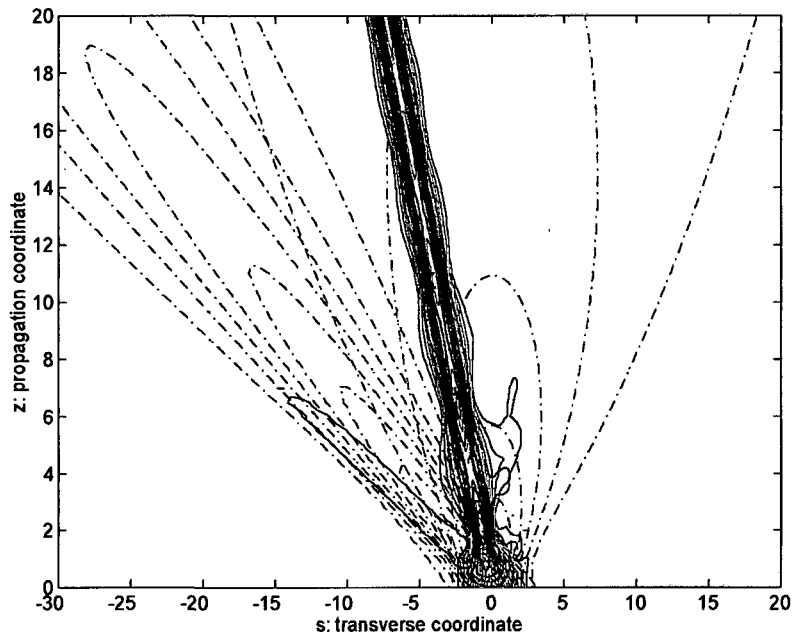Figure 6-1: Sketch of the setup.

Figure 6-2: Superposition of linear (-.) and nonlinear propagation cases. $A_1 = 4$, $A_2 = 1$, $\delta = 1.5$, $\beta = 3$. FF is in red lines and blue ones correspond to SH.

fundamental, to be dragged towards the left in the sketch in Figure 6-1. The asymmetric amplitude profile thus created induces through the nonlinear interaction some asymmetry upon the fundamental phase profile that causes its energy to be dragged to the left too. It can then be said that the second harmonic *drags* the fundamental.

Good efficiency of the dragging process requires the speed of second harmonic shift towards the left not to exceed that for efficient second harmonic influence upon the fundamental so to induce a velocity comparable with its own. That is, the interaction length should be shorter than the walk-off length. Otherwise the second harmonic progressively escapes away to the left as it is generated giving rise to a low energetic slow walking soliton as in Figure 6-3 in cyan and magenta lines. Higher power values may improve the steering by reducing the interaction length and coupling more energy into the soliton whereupon the stationary solution the system tends to has higher second harmonic content yielding better steering according to (6.2).

Figure 6-4 shows a typical outcome of the simulations featuring input and output of a 40 diffraction lengths waveguide and demonstrating the feasibility of performing power controlled steering in the presence of a moderate Poynting vector walk-off. For moderate walk-off values such as efficient nonlinear interaction between the harmonics takes place, higher amounts of power injected into the waveguide as approaching stationary solutions with higher second harmonic content yield greater soliton deviation as reflected on the numerical results displayed in Figures 6-5 and 6-6 where typical efficiencies are around 80% with output position discrimination of about 5 beam widths, well suited for the design of practical applications.

In general the tendency observed in Figure 6-6 is smaller transverse velocity but better energy efficiency as the wavevector mismatch increases due to lower content in second harmonic energy in the stationary state. The great quantity of second harmonic energy required for very low values of β, specially when the power is high causes an increase of the necessary interaction length for efficient dragging to take place which reduces both energy efficiency and soliton deviation, as reflected by the line in magenta in the plot.

The injection of a second harmonic has little effect on soliton deviation but improves the coupling of energy up to a initial fraction of energy into the second harmonic that approaches that for the stationary solution which is smaller as the wavevector mismatch is larger.

Bearing in mind that for bright amplitude profiles a negative slope on the phase profile
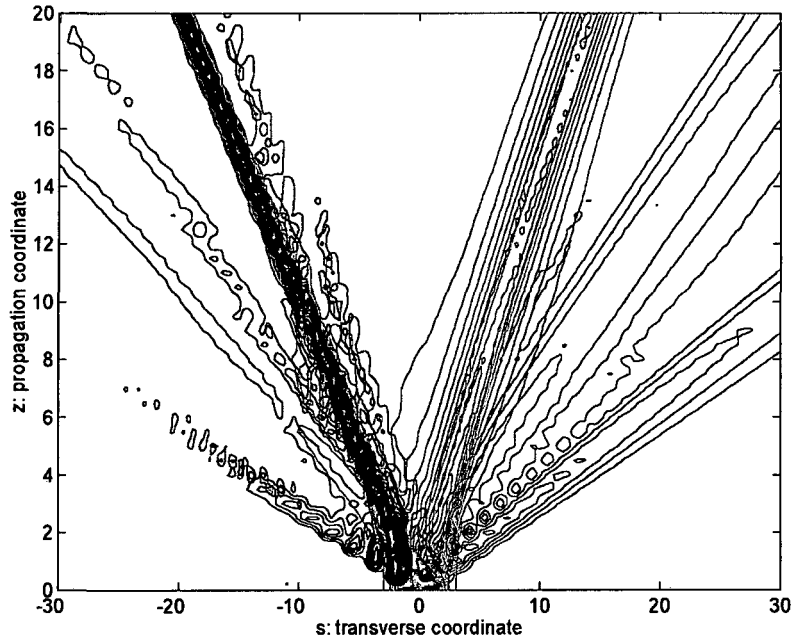
Figure 6-3: Superposition of two examples of fields propagation showing contrast between good energy efficiency and fast traveling soliton obtained for $A_1 = 8$ and $\delta = 3$ (FF: 'r' SH: 'b') and slow traveling soliton and poor energy efficiency obtained for $A_1 = 3$ and $\delta = -3$ (FF: 'm' SH: 'c'). Color scale as in Appendix B.
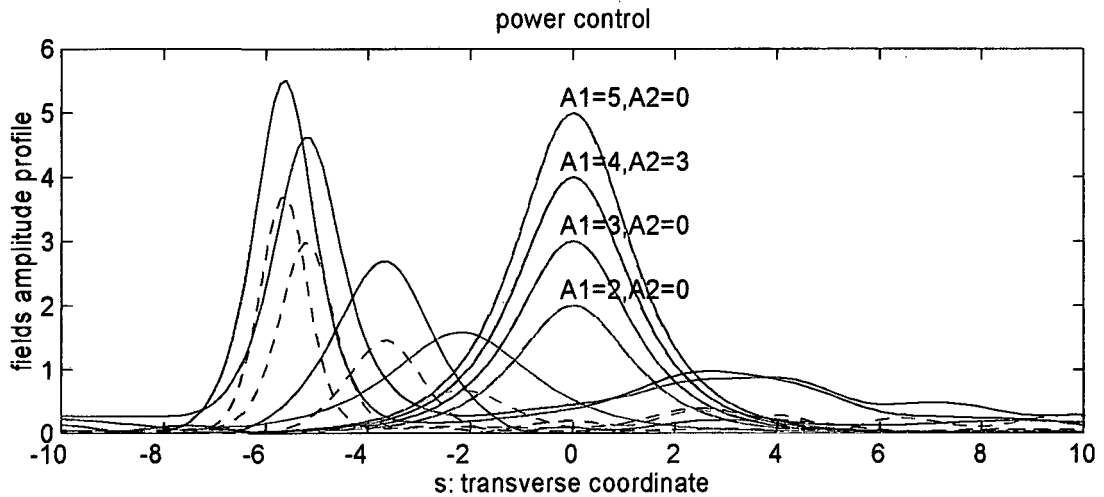

Figure 6-4: Input (black and colored lines) and output (corresponding color (-) for FF, (- -) for SH) of the 40 diffraction lengths waveguide showing some examples of power steering control with $\delta = 1$ and $\beta = 3$.
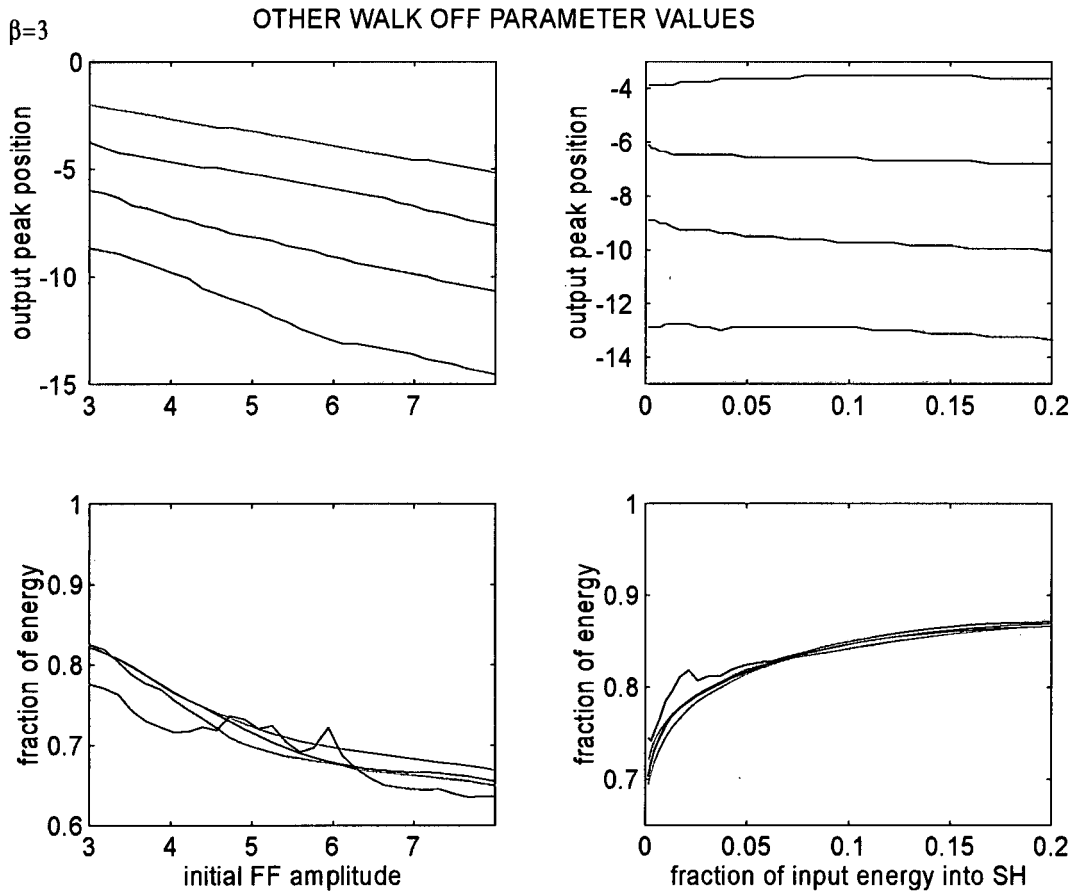
167

Figure 6-5: Features of power controlled steering for various δ values. In all cases $\beta = 3$. Left column $A_2 = 0$, right column $A_1 = 6$. 'm': $\delta = 0.5$, 'bk': $\delta = 1$, 'g': $\delta = 1.5$, 'b': $\delta = 2$. Color scale as in App. B. Top: peak position at the output of a 40 diffraction lengths waveguide; bottom: fraction of input energy coupled to the soliton.
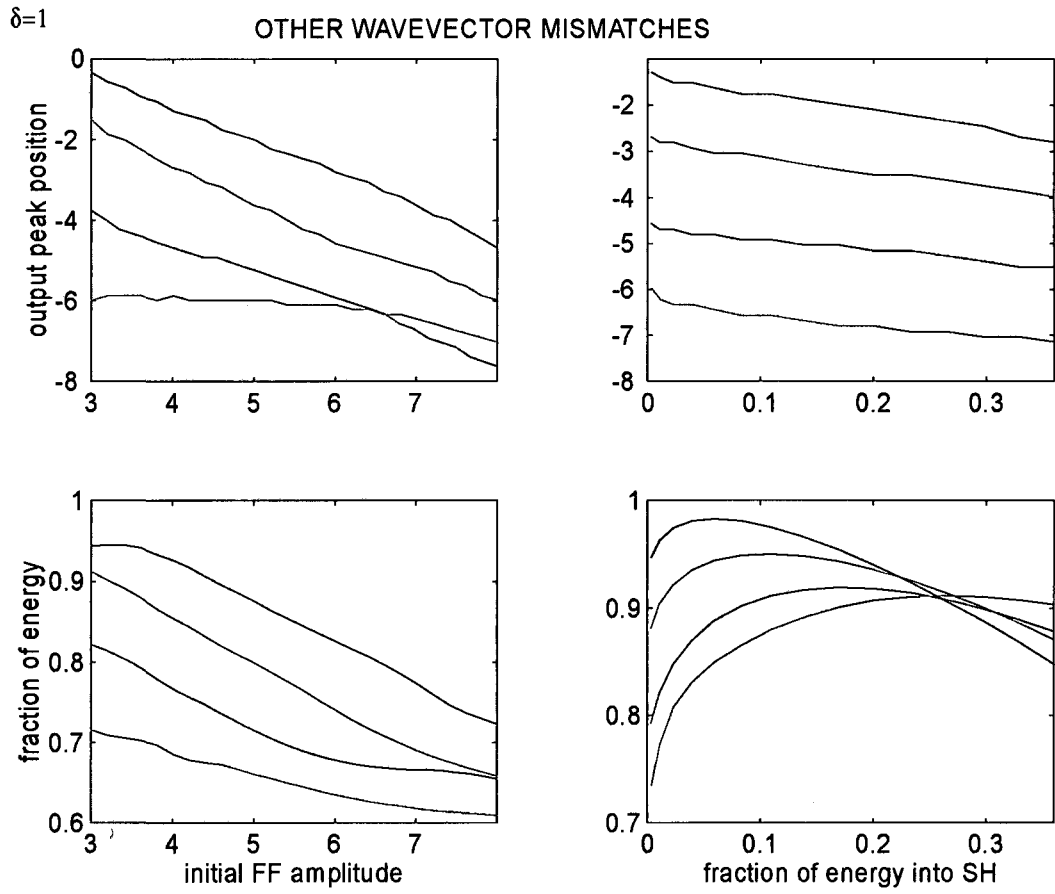
Figure 6-6: Same as Figure 6-5 considering different values of the wavevector mismatch. $\delta = 1$ in all curves, 'm': $\beta = 1$, 'g': $\beta = 3$, 'c': $\beta = 6$, 'b': $\beta = 10$. Left column $A_2 = 0$, right column $A_1 = 4$.

means internal energy flux towards the left in Figure 6-1 and towards the opposite direction if the slope is positive, a look at the amplitude and phase profiles in Figures 6-7 and 6-8 reveals that in the first steps of propagation as a consequence of walk-off the second harmonic gets an asymmetric phase modulation with overall tendency to push the second harmonic energy towards the left but the part of the profiles located most to the right receives some velocity to the right which puts it at clear risk of resulting radiated if the interaction is not fast enough to quickly drag it back to join main profile before main profile has been significantly shifted towards the left by the walk-off. As a consequence of initial nonlinear phase mismatch around $\Delta\phi \sim -\pi/2$ value when no second harmonic is injected (see section 3.6.2), no influence through the nonlinear interaction of the strong fundamental beam upon the second harmonic phase profile is observed in the initial steps. After some propagated distance a change in tendency in the second harmonic phase indicates enough detachment from $\Delta\phi \sim -\pi/2$ and significant fundamental amplitude influence upon the second harmonic phase profile through the nonlinear interaction. Through this influence the fundamental somehow tends to counteract the second harmonic phase distortion imposed by the walk-off to momentarily retain it so that the fundamental phase profile can get through the nonlinear interaction the asymmetric characteristic that may allow it to follow the second harmonic in its lateral shift towards the left. This initial fundamental power induced second harmonic slowing down for more efficient fundamental speeding up can be understood as a *velocities matching* process taking longer distances as the walk-off parameter is larger and the power injected smaller.

In figure 6-9 soliton peak position is compared with the quantity $-\delta L I_2/I$ at the waveguide output with L the length of the waveguide. The difference observed according to (6.1) cannot come but from the addition through the dynamics of some momentum to the soliton, of opposite sign to that carried by radiation.

When the walk-off is small a low velocities matching distance determines the soliton to be quickly formed and start moving to the left thus making more difficult the dragging back to main profile of the energy at the right part initially speeded up by the phase distortion induced by the walk-off. For efficient recovery of energy at the right part of the profiles to take place main profile is required to achieve $\Delta\phi \sim 0$ condition soon before a velocity agreement between the two harmonics is reached and the soliton starts to significantly walk away from the z axis.
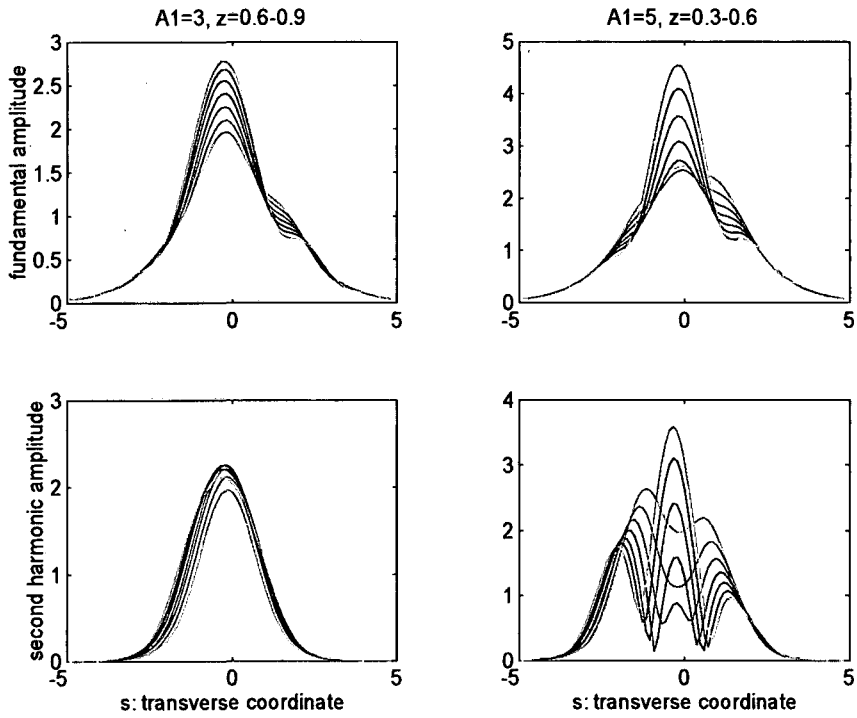
170

Figure 6-7: Evolution of amplitudes in the first steps of propagation. The z coordinate corresponding to each color increases according to the scale: 'y', 'm', 'c', 'r' ,'g' ,'b' in 0.05 steps. Color scale as in App. B.

171

Even though an increase in the power injected into the waveguide helps quick achieving of phase locking, further speeding up of the energy at the right part of the profiles produced by sharper phase distortion leads to net reinforcement of the effect of radiation to the right upon soliton deviation and hence the numerics observation of greater soliton transverse velocity with respect to that predicted by (6.2) for moderate walk-off values and high power values.

Higher wavevector mismatches as featuring a fast detachment from $\Delta\phi \sim -\pi/2$ do ease the coupling of energy to the right part of the profiles so that the effect of radiation to the right is reduced as shown in Figure 6-9.

For large values of the walk-off parameter instead, a too long velocities matching distance when compared to the walk-off length as it happens for low energy values, allows some generated second harmonic to walk the fundamental off before being significantly affected by fundamental induced phase distortion carrying away some negative momentum that causes the soliton to be found more to the right. As the power is raised, the reduction in the velocities matching distance prevents the generated second harmonic to walk the fundamental off by quick action upon its phase so that both harmonics quickly take off leaving behind the speeded up radiation to the right whose positive momentum causes the soliton speeding up towards the left. See Figures 6-8 and 6-9.

Further insight into the wavevector mismatch dependences is gained through Figures 6-10 and 6-12 where it is observed that for only the fundamental field as input, the reduction in second harmonic content in the stationary solution as β increases translates into less soliton deviation and easier coupling of energy into the soliton provided enough energy has been injected so that locking to $\Delta\phi \sim 0$ condition is quickly and easily reached. Otherwise, as making it harder to achieve, the increase in β entails poorer energy efficiency (see curve in green in left column of Figure 6-12).

Soliton deviation is shown to depend on the total energy injected and only slightly on the initial amplitude relation for all wavevector mismatches whereas for a significant fraction of the initial energy contained in the second harmonic the energy coupling as β increases displays an opposite tendency to that of the case of exclusive injection of the fundamental field (curve in magenta in left column of Figure 6-12).

Long velocities matching distance helps the recovery of radiation initially speeded up to the
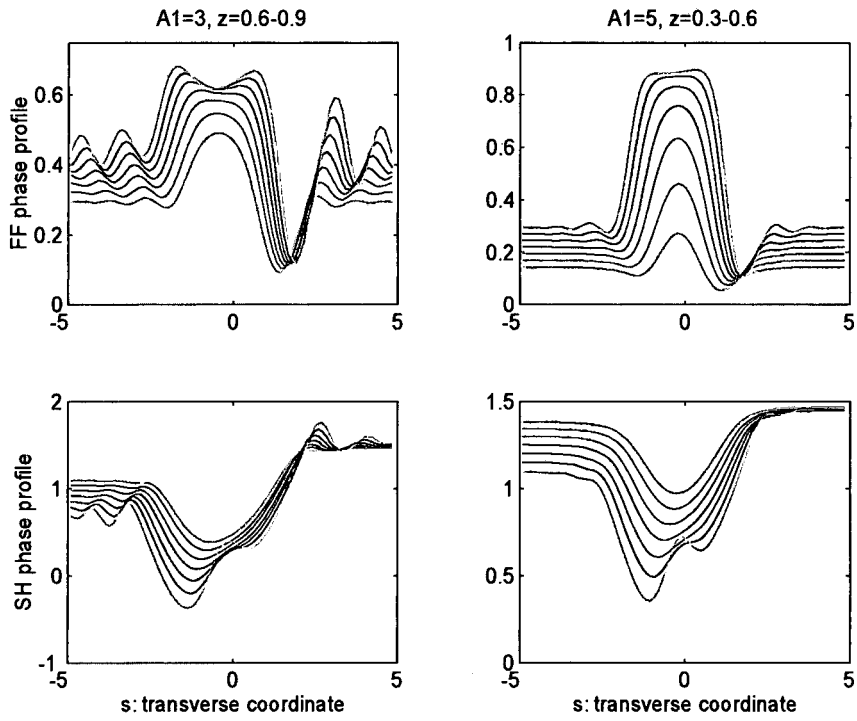
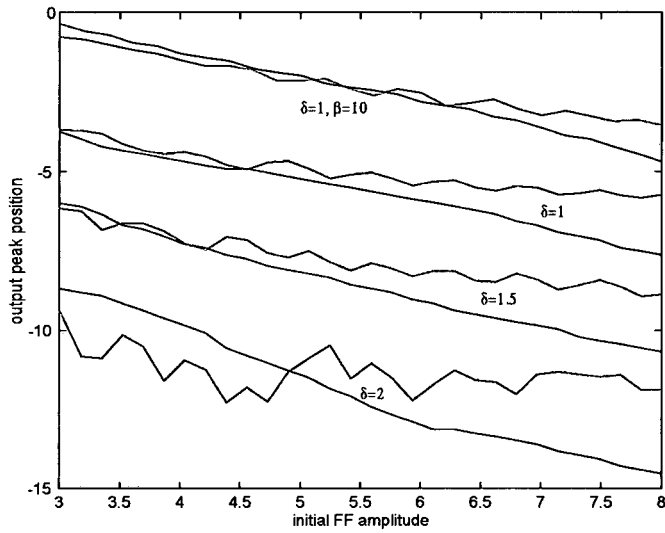Figure 6-8: Same as in Figure 6.7 but for the phase profiles.

Figure 6-9: Comparison of the actual soliton deviation obtained in the simulations at the output of the 40 diffraction lengths waveguide (black lines) and that given by computation of $-\delta I_2 L/I$ with L waveguide length at the same point (red lines).
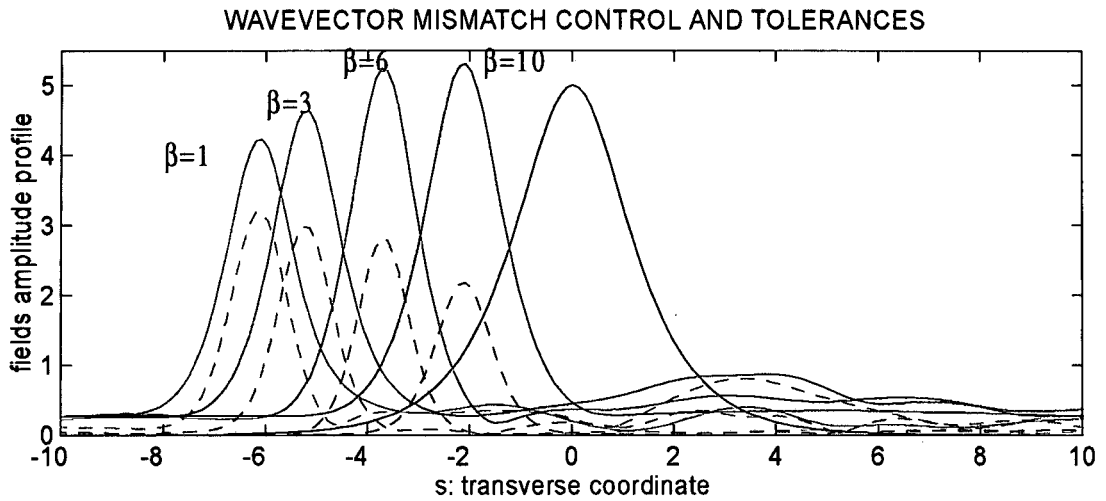
173

Figure 6-10: Input (black line) and outputs of the 40 diffraction lengths waveguide for different wavevector mismatch values. In all cases $\delta = 1$. (-) is for fundamental field and (- -) is for the second harmonic.
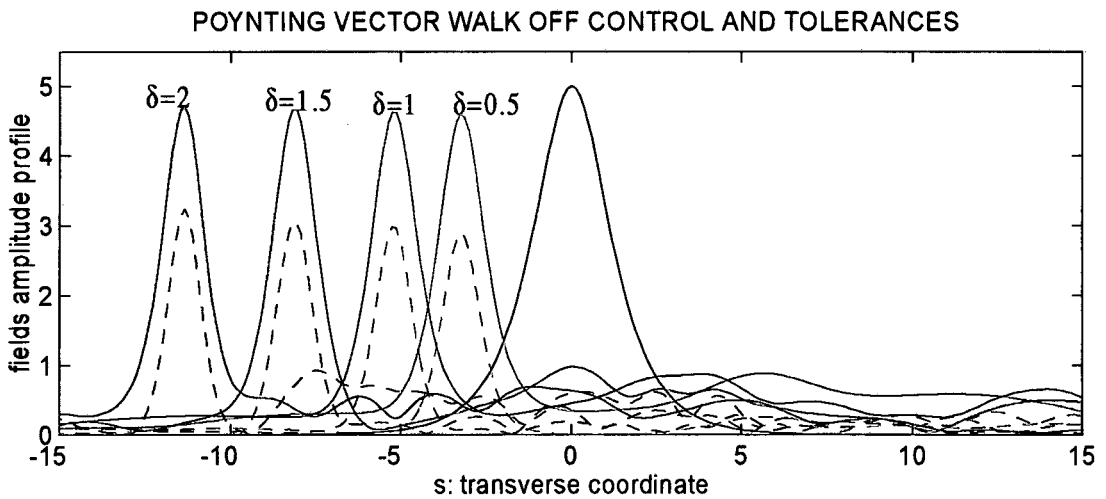
Figure 6-11: Same as in previous figure but for different Poynting vector mismatch values and $\beta = 3$.
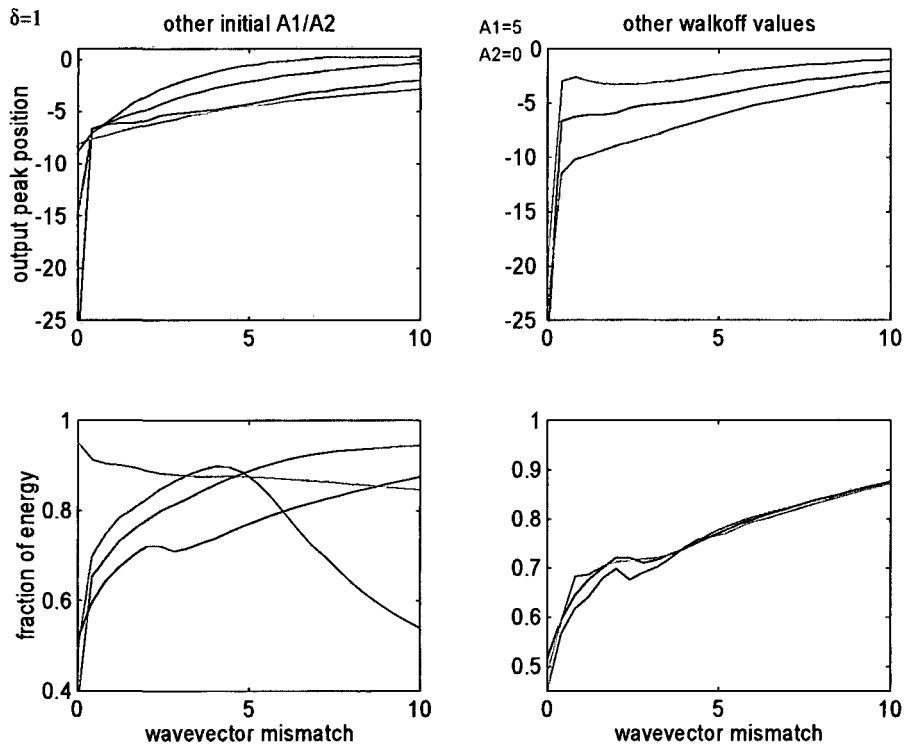
Figure 6-12: Illustration of wavevector mismatch dependences of the steering. Left column: $\delta = 1$; 'g': $A_1 = 2$, $A_2 = 0$, 'b': $A_1 = 3$, $A_2 = 0$, 'bk': $A_1 = 5$, $A_2 = 0$, 'm': $A_1 = 4$, $A_2 = 3$. Right column $A_1 = 4$, $A_2 = 0$; 'g': $\delta = 0.5$, 'bk': $\delta = 1$, 'm': $\delta = 1.5$. Color scale as in App. B. Top: peak position at the output of a 40 diffraction lengths waveguide; bottom: fraction of input energy coupled to the soliton.

175

Figure 6-13: Illustration of Poynting vector walkoff dependences of the steering. Left column: $\beta = 3$; 'g': $A_1 = 2$, $A_2 = 0$, 'b': $A_1 = 3$, $A_2 = 0$, 'bk': $A_1 = 5$, $A_2 = 0$, 'm': $A_1 = 4$, $A_2 = 3$. Right column $A_1 = 5$, $A_2 = 0$; 'g': $\beta = 1$, 'bk': $\beta = 3$, 'b': $\beta = 6$, 'm': $\beta = 10$. Color scale as in App. B. Top: peak position at the output of a 40 diffraction lengths waveguide; bottom: fraction of input energy coupled to the soliton.
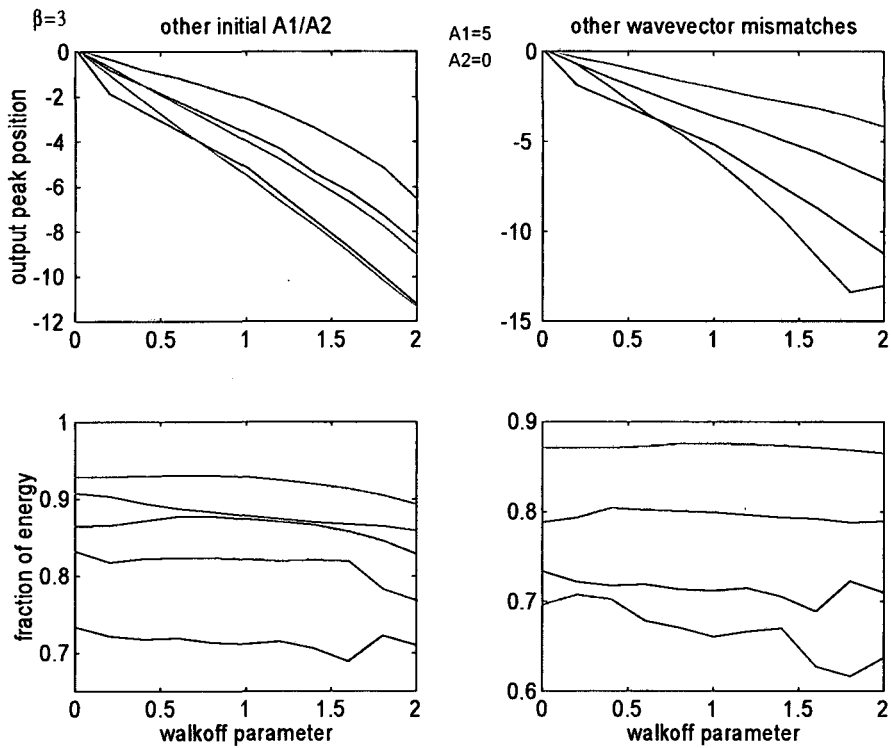
right provided fast enough reaching of $\Delta \phi \sim 0$ condition by main profile takes place. Otherwise as obtained in the $A_1 = 5$, $A_2 = 0$, $\beta = 0$ case (curve in black in left column of Figure 6-12), very fast radiation to the right produced by the combined effect of on one side a sharp initial phase distortion due to endowment of the right part of the profiles with great velocity to the right; and on the other side, sluggish detachment from initial $\Delta \phi \sim -\pi/2$, causes an extraordinary soliton speeding up towards the left.

Figures 6-11 and 6-13 illustrate dependences upon the walk-off parameter value. Very short velocities matching distance determines for low δ values quick soliton formation that hinders speeded up energy to the right be recovered by main profile specially for low β values. The increase in radiation to the right enhances soliton deviation provided β is high enough to guarantee fast enough detachment from $\Delta \phi \sim -\pi/2$ that prevents a significant part of the generated second harmonic escaping away from fundamental (compare the results for $\beta = 1$ and $\beta = 3$). For higher δ values, the increase in the velocities matching distance which eases the coupling of energy to the right causes the decrease in soliton deviation obtained for $\beta = 3$.

Save for very small δ values for which injection of a significant fraction of the energy into second harmonic while reducing the effect of radiation prevents the soliton speeding up, again it is shown that the position of the soliton at the output of the waveguide depends basically on the total energy injected and only improvement of energy efficiency calls for supply of a fraction of energy in the form of second harmonic.

6.1.2 Conclusions

This section has been devoted to analyze Power dependent steering which takes advantage of a moderate Poynting vector walk-off, δ, present in the $\chi^{(2)}$ sample. According to

$$v \approx -\delta \frac{I_2}{I},$$

the shift experienced by the soliton at the waveguide output depends basically on the energy that through the dynamics is alloted to the second harmonic. For their practical relevance, the study has focused in the case in which only the fundamental field is input and hence positive wavevector mismatch values have been considered.

177

For moderate δ values the transverse velocity acquired by the soliton has been seen to follow simple rules, namely

$$I \uparrow \longrightarrow I_1/I_2|_{STAT} \downarrow \longrightarrow v \uparrow \text{ (soliton detaches from propagation axis)}$$

$$\beta \uparrow \longrightarrow I_1/I_2|_{STAT} \uparrow \longrightarrow v \downarrow \text{ (soliton approaches propagation axis)}$$

The soliton deviation was shown to depend mainly on the amount of total power injected into the waveguide and very little in the fraction that initially was carried by the second harmonic. The effect of significant fractions of input energy in the second harmonic was seen to merely lead to some energy efficiency improvement.

With normalized values up to $\delta \sim 2$ entailing for typical conditions, i.e. $\lambda \sim 1\mu m$ and $\eta \sim 15\mu m$ with η beam width, walk-off angles of about $\rho \sim 1 - 2^0$, soliton deviations around 5 beam widths with about 80% of energy efficiency have been obtained in the simulations.

As for the effect of radiation it is summarized in the following diagram:

$$\beta \uparrow \longrightarrow I_1/I_2|_{STAT} \uparrow \qquad \left\{ \begin{array}{l} \text{reduced influence} \\ v \approx -\delta I_2/I \end{array} \right\}$$

$$\delta \uparrow \quad I \uparrow \longrightarrow I_1/I_2|_{STAT} \downarrow \qquad \left\{ \begin{array}{l} \text{initial phase distortion speeds} \\ \text{radiation to the right up} \longrightarrow v \uparrow \end{array} \right\}$$

$$I \downarrow \longrightarrow I_1/I_2|_{STAT} \uparrow \qquad \left\{ \begin{array}{l} \text{reduced SH phase distortion, generated} \\ \text{SH walks FF off} \longrightarrow v \downarrow \end{array} \right\}$$

6.2 Angle-controlled steering

6.2.1 Numerical experiments

This section gathers up all numerical results concerning steering controlled by input light incident upon the waveguide at a certain angle with respect to the optical axis. Optical steering control based on tilted input beams providing the system with a non vanishing total momentum was predicted by Torner et al [121] and some studies that consider type II geometries are found in [124]. With interest lied in identification of effects and possibilities as well as assessment of realistic orders of magnitude of the parameters involved, here the analysis is restricted to type I configurations.

Although the effect of some Poynting vector walk-off will be considered at the end of this section, configurations in which it can be neglected will constitute the main concern, having in mind non-critical or typical QPM phase matching settings. According to (4.16) soliton steering may then be achieved by endowing the system with a non-vanishing momentum, so that the solitary wave that eventually emerges has transverse velocity

$$v \approx \frac{\mathcal{J}}{I},\tag{6.3}$$

being I and $\mathcal{J}$ two conserved quantities, namely the total energy and momentum of the system respectively. Transverse linear phase modulations of the input fields corresponding in practice to simple angular tilts, i.e.

$$a_\nu\left(s, \xi = 0\right) = U_\nu\left(s\right)\exp(-j\mu\nu s),\tag{6.4}$$

with $\nu = 1, 2$, are the means by which the momentum is introduced into the system in such a way that the transverse velocity reads

$$v = \frac{\mathcal{J}}{I} = -\mu_1 \frac{I_1}{I} - \frac{\mu_2}{2}\frac{I_2}{I}.\tag{6.5}$$

The fundamental beam needs to be used if solitonic wave propagation is to be obtained through the launching of only one beam into the waveguide. In that case as a consequence of

the Galilean invariance enjoyed by the governing equations when $\delta = 0$, a soliton propagating with the same transverse velocity as the input is excited resulting in a trivial steering case. Thus interactions between tilted beams both at the fundamental and second harmonic frequencies, using one as the signal and the other as control, will be the subject of study along the present section.

With an eye to practical steering and routing applications, attention is focused to the case in which the fundamental is the signal beam to steer while the second harmonic performs steering control. Practical ways can be implemented to obtain a weak second harmonic control beam out of the incoming fundamental signal beam or other fundamental beam accompanying it acting as control, and readily get the required tilt to attack the waveguide. For that reason it is also important that significant steering is achieved with low power contained in the second harmonic control beam which advises the use of positive wavevector mismatch configurations.

According to (6.3) the soliton which eventually emerges from the interaction has approximate transverse velocity given by

$$v \approx -\frac{\mu}{2} \frac{I_2}{I}\big|_{\xi=0}, \tag{6.6}$$

where μ and I_2 are the input values.

Figure 6-14 features a sketch of a possible practical setup. A planar waveguide structure confines the fields along the vertical y axis whereas confinement along the x axis is achieved through the quadratic nonlinear interaction between fundamental and second harmonic beams. As shown, and according to the internal energy flux expressions (first terms in right hand side of (2.113), (2.114)) and to (6.4), positive values of the linear tilt, μ, entail bright beams traveling to the left in the drawing while negative values will indicate right direction for the beams.

Attacking the guide through different angles actually causes the extraordinary wave to feel different refractive indexes whereupon the linear phase mismatch value slightly varies. However for the small tilts considered in the analysis meant to keep the validity of the paraxial approximation, this variation is assumed to be negligible although overall dependences upon the wavevector mismatch will be investigated. Likewise, slanted incidence into the crystal may entail appearance of a small Poynting vector walk-off whose effect is briefly outlined at the end of the section.

Fundamental and tilted second harmonic beams which in absence of nonlinearity would

propagate inside the waveguide independently in different directions, mutually trap and lock each other as a consequence of the quadratic nonlinear response of the guiding medium and form a soliton that exits the waveguide at an intermediate position as Figure 6-15 showing the superimposition of the evolution of the field profiles of the two harmonics in a representative case in a linear and a nonlinear medium respectively, clearly illustrates.

The momentum initially carried out only by the second harmonic has to be communicated to the whole system so that the solitary wave finally formed is the result of a trade-off through which the dynamics selects among the infinite travelling wave replicas of the non walking solitary waves existing in all directions, hopefully within the limits of the paraxial approximation, the best suited for the initial conditions given. The process of progressive transfer and sharing of momentum between the harmonics is illustrated in Figure 6-16 featuring the evolution of each harmonics' energy centroid for selected cases and showing how each beam net transverse flux of energy changes direction dynamically until the fields phase fronts and amplitude relations and shapes are adjusted so to cancel nonlinear phase mismatch and form an oscillating state slightly walking the z axis off. Initial tilt, total energy and amplitudes, together with the configurations' wavevector mismatch determine the trade off value for the final propagation angle of the emerging soliton and the fraction of the initial energy that it carries.

If radiative losses are small one could naïvely take (6.3) to be a good approximation of the transverse velocity of the solitary wave finally formed and that could indeed be the case if the radiation produced by the dynamics of soliton formation was symmetric and thus the momentum stolen from the soliton had zero average. The fact that asymmetric radiation will be produced is clear from the viewpoint that the initial phase front profile imposed by the tilt creates differentiate zones with opposite signs of the initial energy exchange between harmonics (see Figure 6-26) which therefore undergo different dynamics.

An arrow in Figure 6-15 indicates the position at the waveguide output that would approximately correspond to the energy centroid had it travelled at the transversal velocity dictated by (6.6). The difference obtained is mainly due to the momentum carried by radiation which does not have zero average as reflected also by the plot in Figure 6-15, as a consequence of the asymmetry in the energy exchange between harmonics introduced by the tilt.

Once the main features of the phenomenon of beam trapping creating solitons walking in
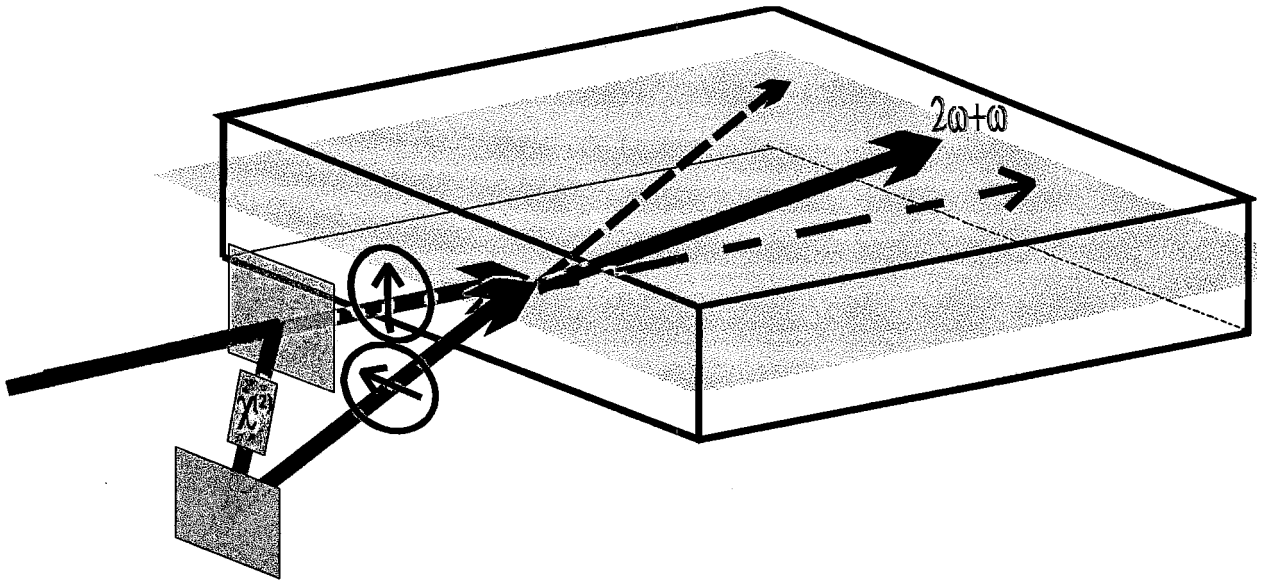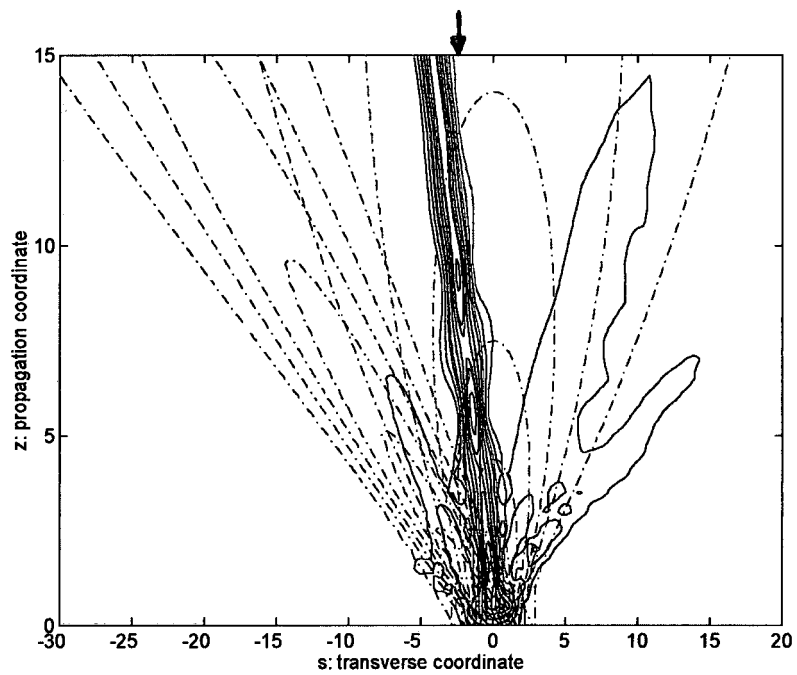
181

Figure 6-14: Sketch of the setup.

Figure 6-15: Linear (-.) and nonlinear (-) propagation for $A_1 = 4.5$, $A_2 = 1.5$, $\mu = 3$ and $\beta = 3$. As usual, red is for FF and blue for the SH.
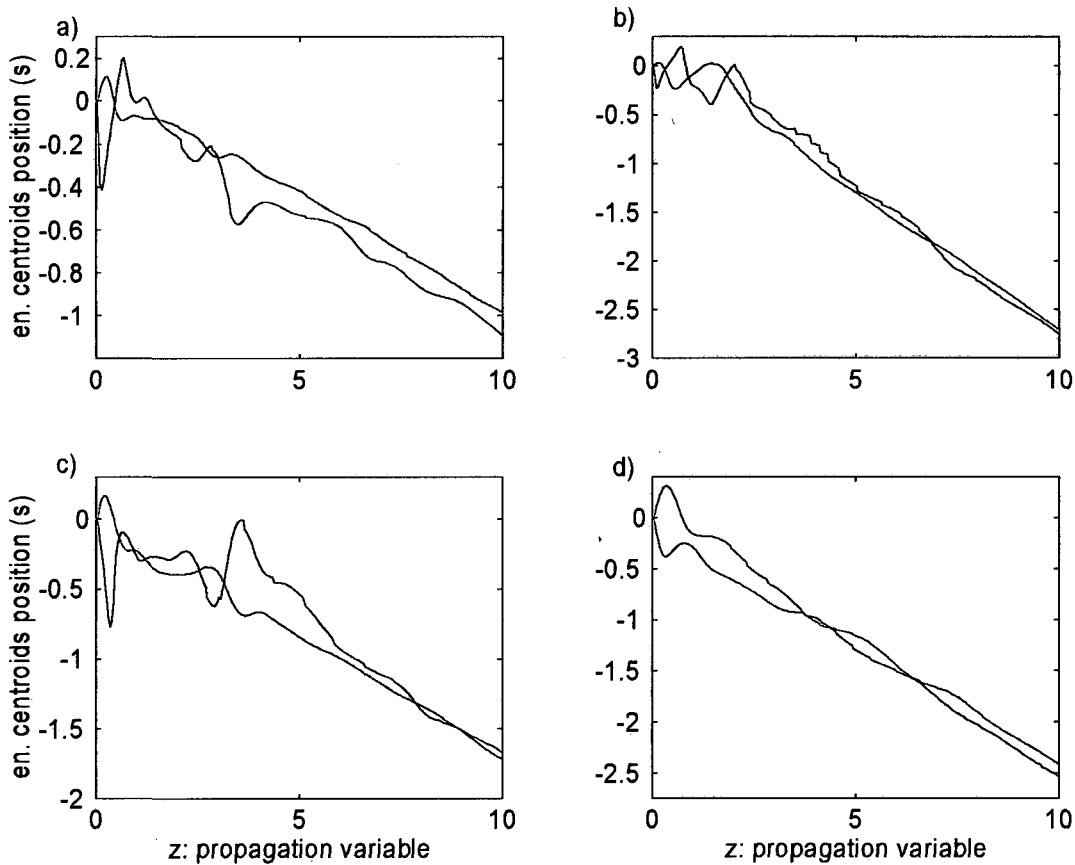
182

Figure 6-16: Evolution of energy centroids in some typical cases. As usual red is for the fundamental and blue is for the second harmonic. (a): $\beta = 3$, $A_1 = 4.5$, $A_2 = 1.5$, $\mu = 1$; (b): same but $\mu = 3$; (c): same as a) but $A_1 = A_2 = 3$; (d): same as c) but $\beta = -3$.

different directions through injection of tilted beams which introduce a certain momentum into the system have been outlined, the implications for efficient steering control are considered.

To begin with, the feasibility of input angle control of the steering is analyzed. The propagation of the fields along a waveguide 40 diffraction lengths long has been simulated using a split-step Fourier method.

A tilt value of $\mu \leq 4$, corresponding for typical conditions, $\lambda \simeq 1\mu m, \eta \simeq 15\mu m$, to an input angle of about

$$\theta = \arctan\left(\frac{\mu/\eta}{2\pi/\lambda}\right) = 1.3^0, \tag{6.7}$$

is taken as a safety limit to guarantee the applicability of the paraxial approximation.

The profiles considered have a *Sech* like transversal dependence so that the inputs provided to the numerical algorithm have the form

$$\begin{aligned} a_1(\xi = 0, s) &= A_1 Sech(s), \\ a_2(\xi = 0, s) &= A_2 Sech(s) \exp(-j\mu s), \end{aligned} \tag{6.8}$$

Some examples of angle steering control are shown in Figure 6-17.

The position in beam widths units of the soliton which eventually emerges at the output as well as the fraction of the incident energy that has been coupled to it are plotted in Figure 6-18. The curves reveal that efficient beam steering on the order of 5 beam widths with reasonable energy efficiencies on the range of 80% can be achieved. Other initial amplitudes and other wavevector mismatches yielded analogous results thus confirming the robustness of the steering method and rendering the configuration perfectly suited for the design of practical applications.

A remarkable feature pointed out by the plots in Figure 6-18 is the existence of an optimum value of the initial tilt that maximizes beam deviation. Above this optimum value the transversal velocity induced by the tilt onto the second harmonic is so high that the fundamental is not able to trap it and much of the second harmonic energy escapes carrying a significant part of the total momentum it has introduced into the system. Below this optimum value, influence of the tilt on the initial energy exchange between harmonics produces a small amount of radiation that travels in the direction opposite to the one imposed by the tilt thus enhancing the steering. This effect is more evident for small wavevector mismatch setups since the initial amplitudes
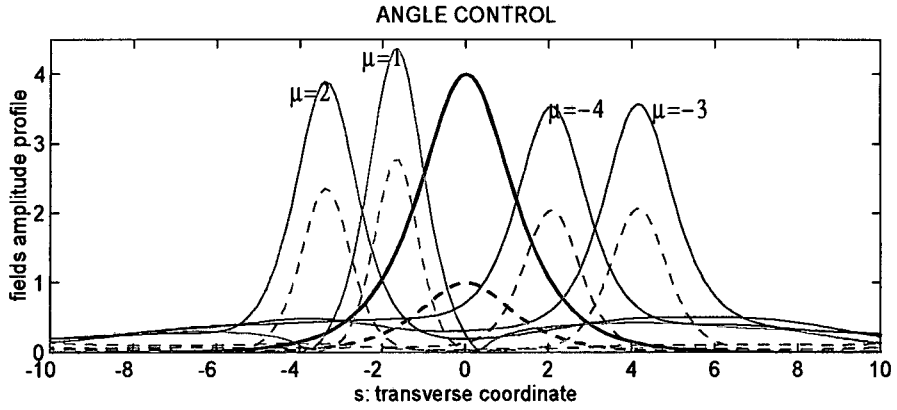
184

Figure 6-17: Input and outputs at 40 diffraction lengths demonstrating angle control of the steering. In all cases $\beta = 3$. (-) FF amplitude profile, (- -) SH amplitude profile.
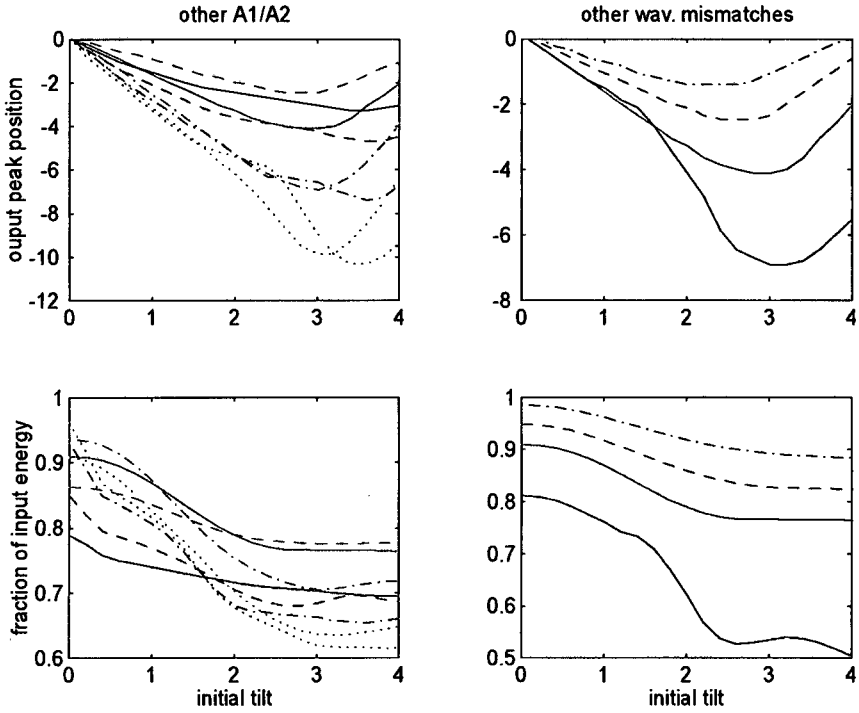

Figure 6-18: Features of angle controled steering. Left: different input amplitudes with $\beta = 3$. ('m' lines) $A_1 = 4$, (- -): $A_2 = 0.5$, (-): $A_2 = 1$, (-.): $A_2 = 2$, (:): $A_2 = 3$. ('g' lines) $A_1 = 6$, (-): $A_2 = 0.5$, (- -): $A_2 = 1$,(-.): $A_2 = 1.5$, (:): $A_2 = 2$. Right: different β values with $A_1 = 4$, $A_2 = 1$. ('m' line): $\beta = 3$, ('b'-): $\beta = 0$, ('b'- -): $\beta = 6$, ('b'-.): $\beta = 10$. Color scale as in App. B.

185

fall further away from the values needed for the stationary solution and the dynamics of beam trapping requires a longer propagation length.

Next series of numerical experiments aimed at demonstrating the possibility of controlling the deviation of the trapped beam through control of the energy contained in the second harmonic control beam yielded the results shown in Figures 6-19, 6-20 and 6-21.

These results evidence great sensibility of the steering on the initial power content in the second harmonic due both to influence on the momentum introduced into the system according to $\mathcal{J} = -\mu I_2/2$ and also due to its effect on the dynamics towards the reach of a stationary state.

Specifically, Figure 6-21 shows in its top row plots whose curves all feature the same value of expected velocity according to (6.6), that when the total energy flow, I, is increased, due to the reduction in nonlinear interaction length easing momentum sharing between the harmonics, faster solitons are obtained. The increase in soliton velocity is less evident for small second harmonic energy fractions of the total energy due to the decrease in the stationary energy flow relation, $I_1/I_2|_{STAT}$, which takes place with an increase of I and that tends to enlarge the nonlinear interaction length. A similar argument considering the influence of the wavevector mismatch, β, on the nonlinear interaction length explains the curves obtained in 6-21 bottom row. In this sense it is observed for very low total input powers and high wavevector mismatches in Figure 6-21 that the difficulties that an input second harmonic power increase poses as for the reaching of a stationary solution that features a very low second harmonic power content lead to obtention of very small soliton deviations and of course poor energy efficiencies in spite of the total momentum into the system being increased. Finally, also thinking on the feasibility to perform temperature control of the steering, the dependences upon the wavevector mismatch present in the system were evaluated. The results in Figures 6-22 demonstrate the robustness of the steering effect although the deviation of the peak obtained as well as the energy coupled to it strongly depend on the wavevector mismatch value. Mind that, opposite to initial tilt value and initial power or power fraction which determine different values for the expected velocity as given by (6.6), the wavevector mismatch dependence of soliton steering steams uniquely from its influence upon the parametric interaction through which the initial momentum is introduced into the system. In short, the conclusion extracted from these plots is that as the wavevector
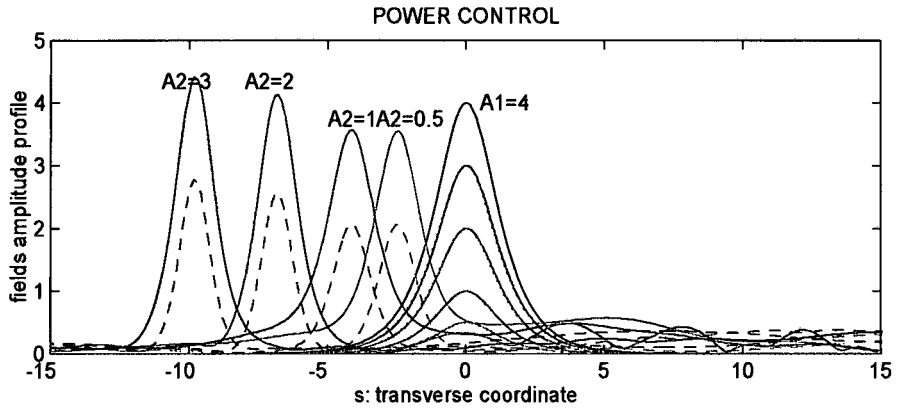
POWER CONTROL

Figure 6-19: Inputs and outputs at 40 diffraction lengths demonstrating power control of the steering. In all cases $\beta = 3$, $\mu = 3$.
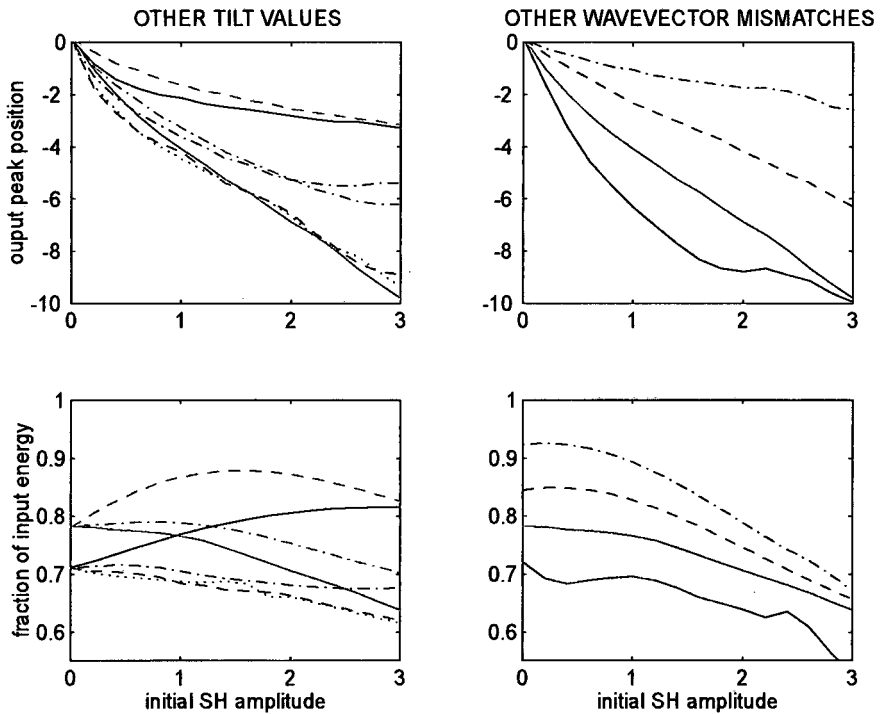

Figure 6-20: Features of power controlled steering for other values of the initial tilt and other wavevector mismatches. 'm' lines: $A_1 = 4$, $A_2 = 1$; 'g' lines: $A_1 = 6$, $A_2 = 1$. Left: (- -) $\mu = 1$; (-.) $\mu = 2$; (-) $\mu = 3$; (:) $\mu = 4$. Right: ('b-') $\beta = 1$; ('m') $\beta = 3$; ('b- -') $\beta = 6$; ('b-.') $\beta = 10$. Color scale as in App. B.
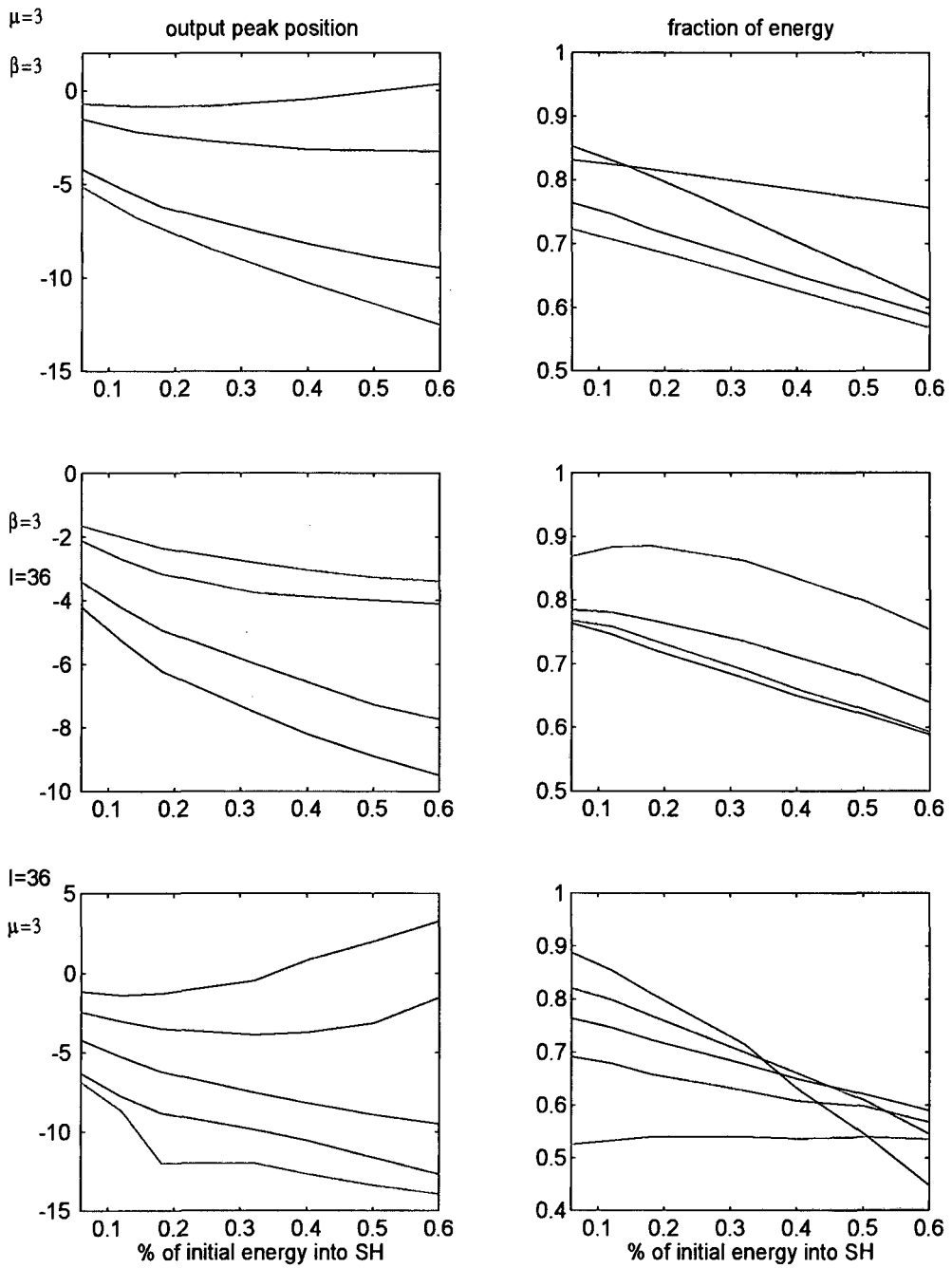
Figure 6-21: Features of power controlled steering. $\beta = 3$, $I = 36$, $\mu = 3$ unless stated otherwise. Top ('r'): $I = 8$; ('g'): $I = 18$; ('bk'): $I = 36$; ('m'): $I = 50$. Middle ('m'): $\mu = 1$; ('c'): $\mu = 2$; ('bk'): $\mu = 3$; ('g'): $\mu = 4$. Bottom ('m'): $\beta = 0$; ('g'): $\beta = 1$; ('bk'): $\beta = 3$; ('r'): $\beta = 6$; ('b'): $\beta = 10$. Color scale as in App. B.

obtained at the expense of a poorer energy efficiency due to the influence of radiation whose direction opposes that of the tilt.

For getting a feeling on how radiation impacts upon the transverse velocity of the soliton finally formed and recalling that for a given total power, proximity to the stationary solution depends basically on the harmonics amplitude relation in such a way that to a great extent it determines the amount of radiation to be expected, in the next set of numerical experiments inputs with the same total power I but different amplitude relation between harmonics A_1/A_2 are considered (Fig 6-23).

In all cases an optimum value of μ for which the steering is maximum is obtained which is smaller and gives better deviation than predicted by (4.16) for big A_1/A_2 while slightly greater and giving worst steering than predicted for small A_1/A_2 (see the curves in bottom row). The existence of this point of maximum soliton deviation and its dependence upon the initial amplitude values is understood by considering that for efficient nonlinear coupling of first and second harmonic which enables the momentum carried by the second harmonic to be shared with the fundamental, the second harmonic left shifting tendency needs to be initially slowed down under the influence of the fundamental amplitude. The faster and more powerful the second harmonic the more powerful has to be the fundamental to realize the trapping and consequently this maximum steering initial tilt value is smaller as the relation A_1/A_2 is decreased.

A too fast and powerful relative to the fundamental second harmonic beam is shown to be detrimental for the steering because as not efficiently slowed down by nonlinear interaction with the fundamental, a great part of its energy walks the main fundamental beam off so that only a small fraction of fundamental wave is able to follow it. The fast traveling second harmonic along with the portion of fundamental that it has somehow managed to pull up from the main profile selfishly retain a significant part of the momentum injected into the system and may form a soliton above a threshold power as shown in Figure 6-24 bottom row, but in any case abandon the main part of injected fundamental beam so that solitons carrying a significant part of the injected energy are necessarily slow.

The fact that the second harmonic literally abandons the fundamental is evident in Figure 6-25 bottom row where the amplitudes evolution in symmetric waveguide longitudinal cuts

6-25 bottom row where the amplitudes evolution in symmetric waveguide longitudinal cuts located far away from the area where soliton propagation takes place, yields analogous behavior of radiation in the case of a too fast second harmonic beam and that of no injection of any second harmonic with the difference of some fast radiation to the left observed in the second harmonic amplitudes plot indicating the injected second harmonic is leaving the scene.

It is important to note that since the total momentum in the system has to be conserved the initial second harmonic slowing down effect needs to be payed for so that it takes place in a reduced central part of the profile while outer parts actually result speeded up, see Figure 6-26. If the velocity imprinted to these outer parts is small compared with that of the nonlinear interaction, a great deal of their energy can eventually be recovered by the main profile.

On the other hand, the initial transverse linear phase front variation imposed on the second harmonic input beam yields differentiate areas at each side of the $s = 0$ point with opposite signs of the inter harmonics energy flow and therefore it severely influences the dynamics in such a way that for the input conditions considered here, soliton formation is eased for $s < 0$ whereas it is hindered for $s > 0$, Figure 6-26.

The effect is more pronounced for big A_1/A_2 values and that is seen in Fig 6-23 in the increase of energy coupled to the output soliton for small values of μ as the relation A_1/A_2 is decreased. The added loss observed for big values of μ as the A_1/A_2 relation decreases corresponds to radiation to the left produced by a strong second harmonic pushing hard to the left and a weak fundamental not capable of trapping it.

The plots in Figure 6-25 constitute a good illustration of the influence of the initial tilt on the asymmetry displayed by radiation. In Figure 6-24 it is shown how when the total power is increased the small fraction pulled up by the second harmonic from main profile is able to form a soliton for large initial left traveling speeds, whereas when this initial velocity is small a soliton traveling to the right is formed by the residual radiation produced at the right part of the profiles because of the asymmetry in energy exchange.

Figure 6-23 bottom row, shows the soliton peak position shift with respect to the one expected if the momentum carried by radiation had zero average. As a consequence of radiation being minimized, the steering observed is almost equal to the expected until a too big value of the initial tilt makes it impossible for the fundamental beam to slow the second harmonic down

190

Likewise, when taking equal values of the relation A_1/A_2 but different total input powers as in Fig 6-23 right column, which is equivalent to consider equal values for the nominal velocity as given in 4.16, it is observed that the value of μ for which the steering is maximum decreases as the total power is increased and that is explained by the fact that for higher total power the amplitudes stationary values are further away from the initial A_1/A_2 relation considered in this case which as entailing a longer time required to realize the trapping, ease second harmonic walking the fundamental beam off. The plot for the fraction of energy into the soliton in Figure 6-23 right column, bottom row, shows agreement giving less energy coupled for higher input powers.

Enhanced coupling of energy initially located at the $s > 0$ side of the profiles into the soliton takes place when a value of μ is reached which causes the appearing in a transversal coordinate to the right side of the profiles with relevant field amplitudes, of an additional area to be initially affected by an energy flow from fundamental to second harmonic which fast enough is capable of getting close to $\Delta\phi = 0$ condition. On the other hand for the same initial tilt value, an increase of radiation to the left is produced as a consequence of swift escaping to the left of an area of second harmonic to fundamental energy exchange at the $s > 0$ part of the profiles not efficiently influenced by the initial phase distortion. The combination of both effects causes the decrease in soliton deviation with energy efficiency maintenance observed in the curves for large μ values.

In other words, it is the existence of two zones with opposite sign of the energy flow at each side of $s = 0$ for a large value of μ as illustrated in Figure 6-26 which gives fast left travelling and hence stealing part of the initial momentum radiation for $s < 0$ and big left travelling fluxe and hence coupling more of the energy initially located at the right part of the profiles into the soliton for $s > 0$ causing the soliton to slow its left shift down while keeping the fraction of input energy it carries for large values of μ.

At this point it is useful to analyze in detail the process of beam trapping. Figure 6-26 illustrates how under the influence of the strong fundamental beam through the nonlinear response of the medium, the second harmonic undergoes a phase front smoothing that slows its left shift tendency down. Also the asymmetric energy exchange (gain for $s < 0$, loss for $s > 0$) becomes apparent. These two features are captured by analytically solving the governing

191

$s > 0$) becomes apparent. These two features are captured by analytically solving the governing equations under the assumption of no significant variation of the fundamental frequency beam. One readily finds

$$a_2(\xi, s) = a_2(0, s)\exp(-j\beta\xi) + \frac{1}{\sqrt{\beta}}a_1(0, s)^2 * \exp\left(-2\sqrt{\beta}|s|\right)(1 - \exp(-j\beta\xi)). \qquad (6.9)$$

For the specific input field profiles analyzed here, and phase mismatch values on the range of $\beta \sim 3 - 10$, by writing the fields in the form $a = U\exp(j\phi)$ the above may be approximated by

$$a_2(\xi, s) \simeq U_2\exp(-j(\mu s + \beta\xi)) + \frac{U_1^2}{\beta}(1 - \exp(-j\beta\xi)). \qquad (6.10)$$

Fig 6-27 demonstrates the accuracy of this approximation in modelling the evolution of the second harmonic beam for small propagated distances.
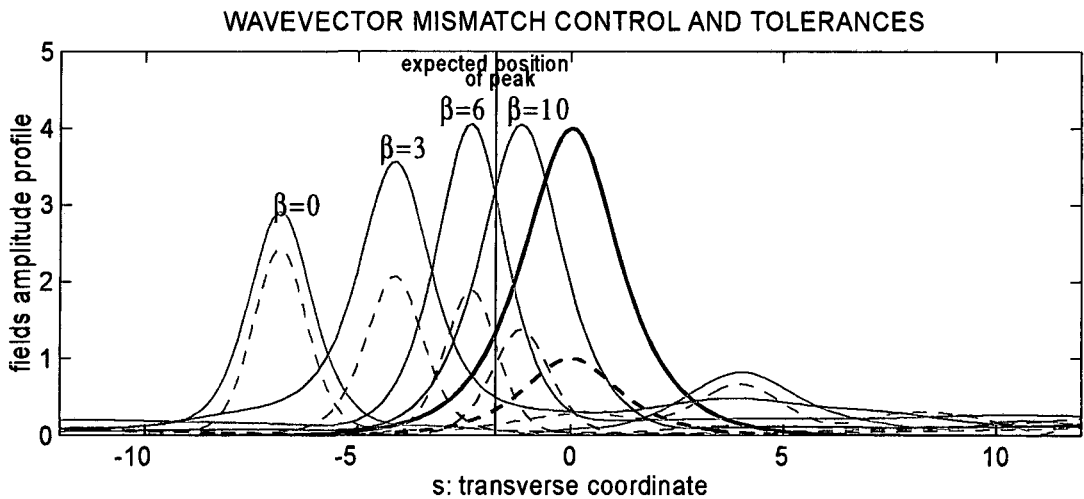

Figure 6-22: Input and outputs of a 40 diffraction lengths waveguide illustrating wavevector mismatch dependences of the steering. $A_1 = 4$, $A_2 = 1$, $\mu = 3$.
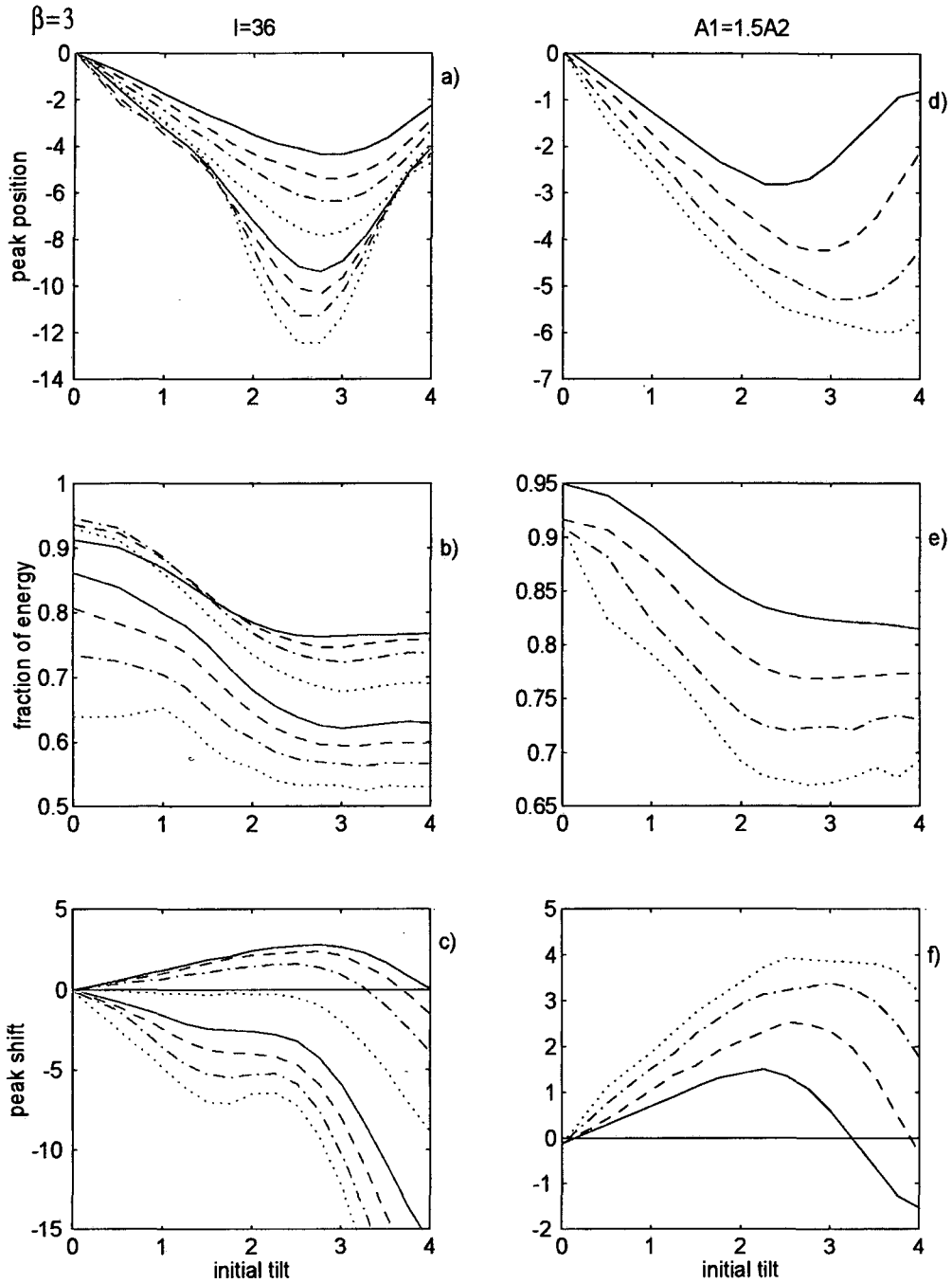
Figure 6-23: Features of the steering for $\beta = 3$. Left: ('g' lines): $A_1 > A_2$; ('m' lines): $A_1 \leq A_2$. ('g'-): $A_1 = 4.12$, $A_2 = 1$; ('g'- -): $A_1 = 4$, $A_2 = 1.4$; ('g'-.): $A_1 = 3.85$, $A_2 = 1.8$; ('g':): $A_1 = 3.5$, $A_2 = 2.4$; ('m'-): $A_1 = A_2 = 3$; ('m'- -): $A_1 = 2.7$, $A_2 = 3.25$; ('m'-.): $A_1 = 2.4$, $A_2 = 3.5$; ('m':): $A_1 = 2$, $A_2 = 3.25$. Right: ('b'-): $I = 19.12$; ('b'- -): $I = 34$; ('b'-.): $I = 53.12$; ('b':): $I = 76.5$. Color scale as in App.B.
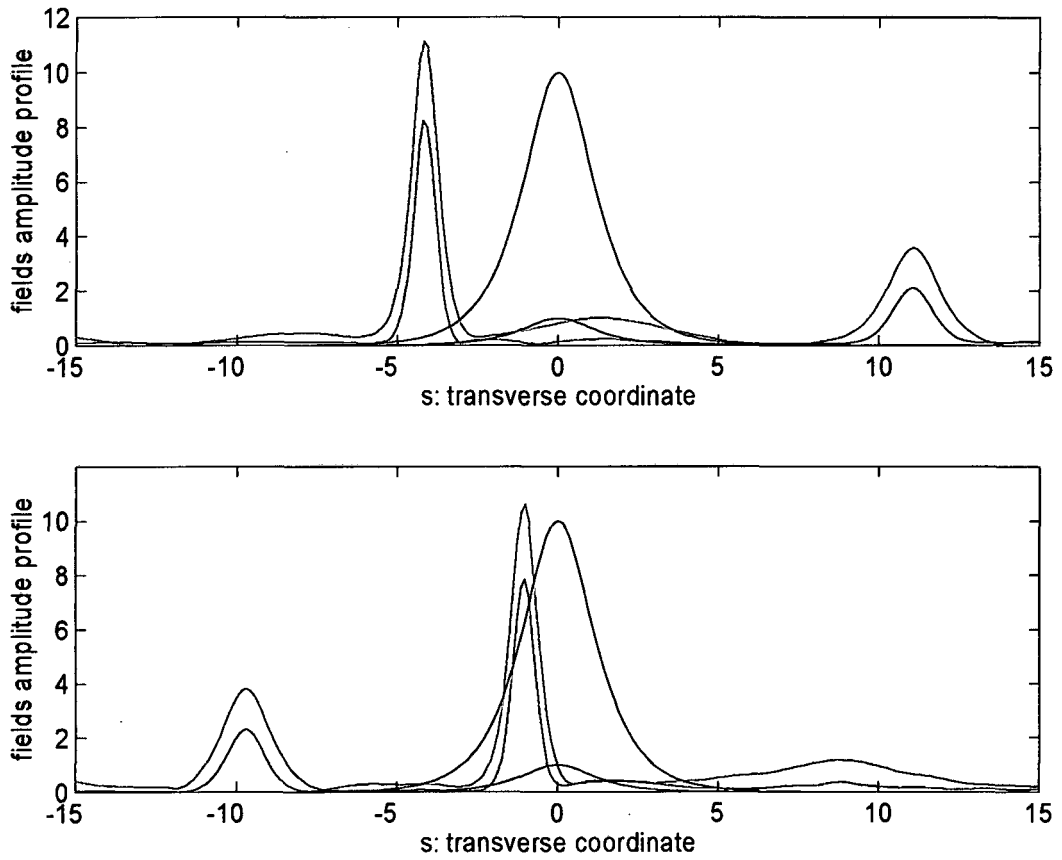
Figure 6-24: An additional low energetic soliton is formed travelling to the right for $\mu = 2$ and to the left for $\mu = 3.5$. In both cases $A_1 = 10$, $A_2 = 1$, $\beta = 3$ and the outputs are taken at 40 diffraction lengths.
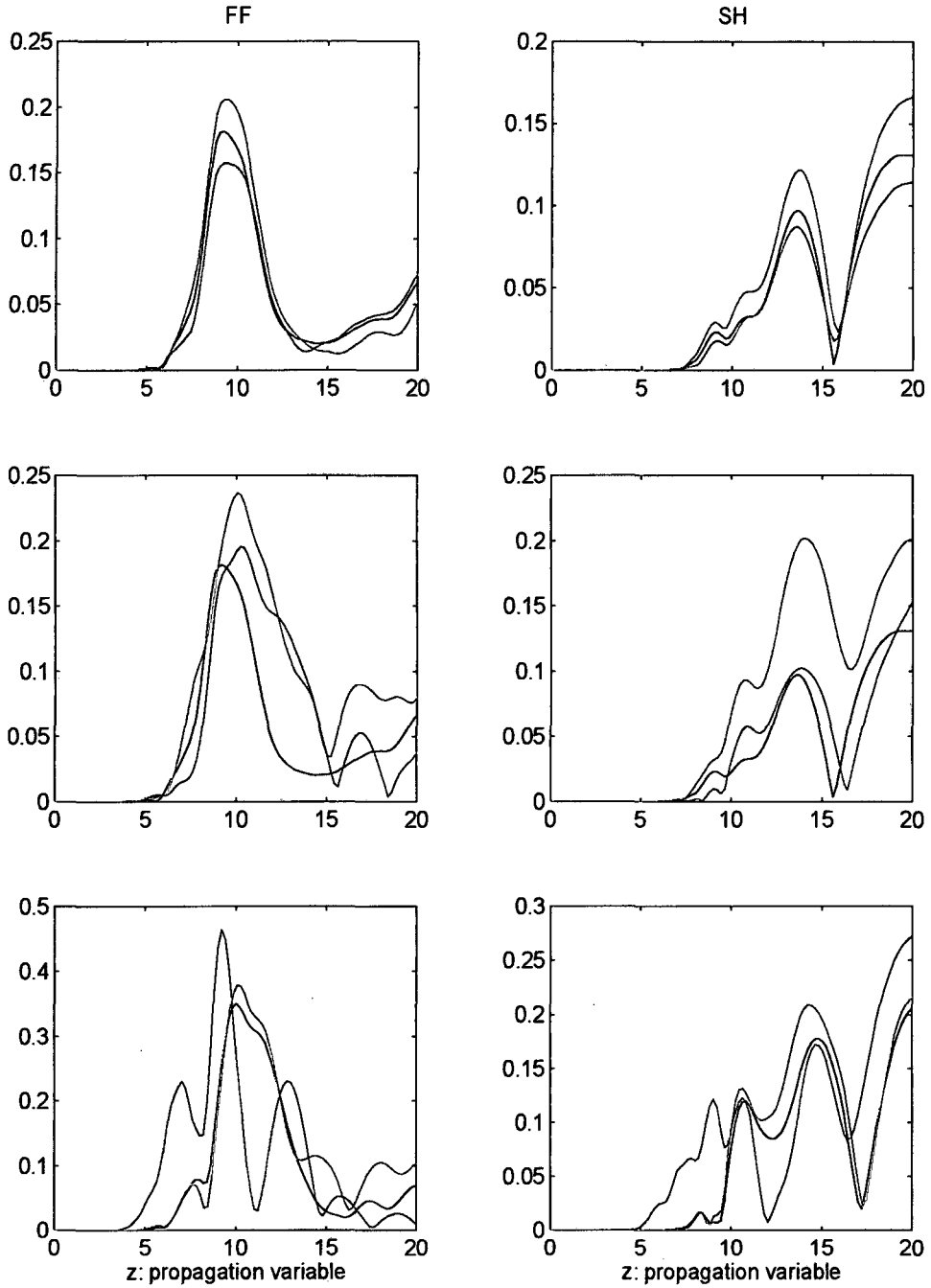
Figure 6-25: Amplitudes evolution in longitudinal waveguide cuts in symmetric transverse points $s = -30$ ('g'), $s = 30$ ('m') to illustrate the behavior of radiation. $A_1 = 4$, $A_2 = 1$, $\beta = 3$, and $\mu = 0.5$ (top), $\mu = 2$ (middle) and $\mu = 4$ (bottom). In top an middle row the 'm' line corresponds to the same amplitude evolution in the no tilted case and in bottom row, it shows the case $A_1 = 4$, $A_2 = 0$. Color scale as in App. B.

π units

FF to SH   SH to FF

s: transverse coordinate

SH to FF   FF to SH
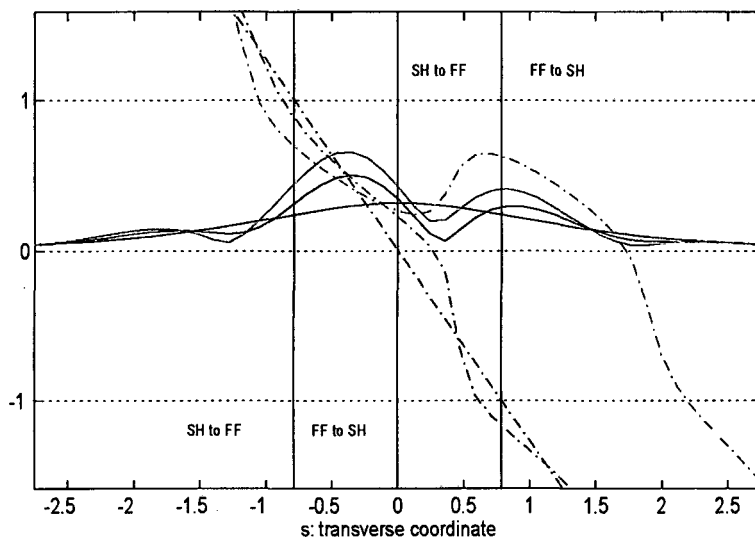
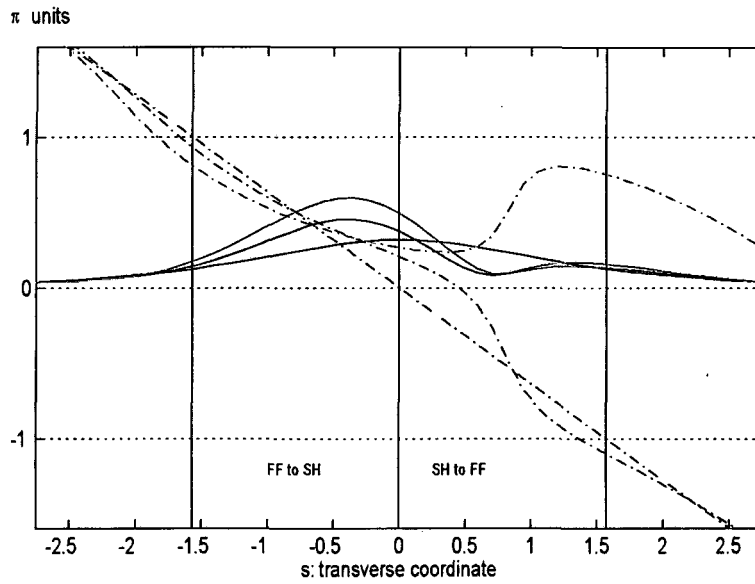SH to FF   FF to SH

s: transverse coordinate

Figure 6-26: Second harmonic amplitude and phase profiles in the first steps of propagation for $A_1 = 4$, $A_2 = 1$, $\beta = 3$. 'bk': input; ('m'-): $\xi = 0.05$; ('m'-.): $\xi = 0.1$. Top: $\mu = 2$. Bottom: $\mu = 3$. Color scale as in App. B.
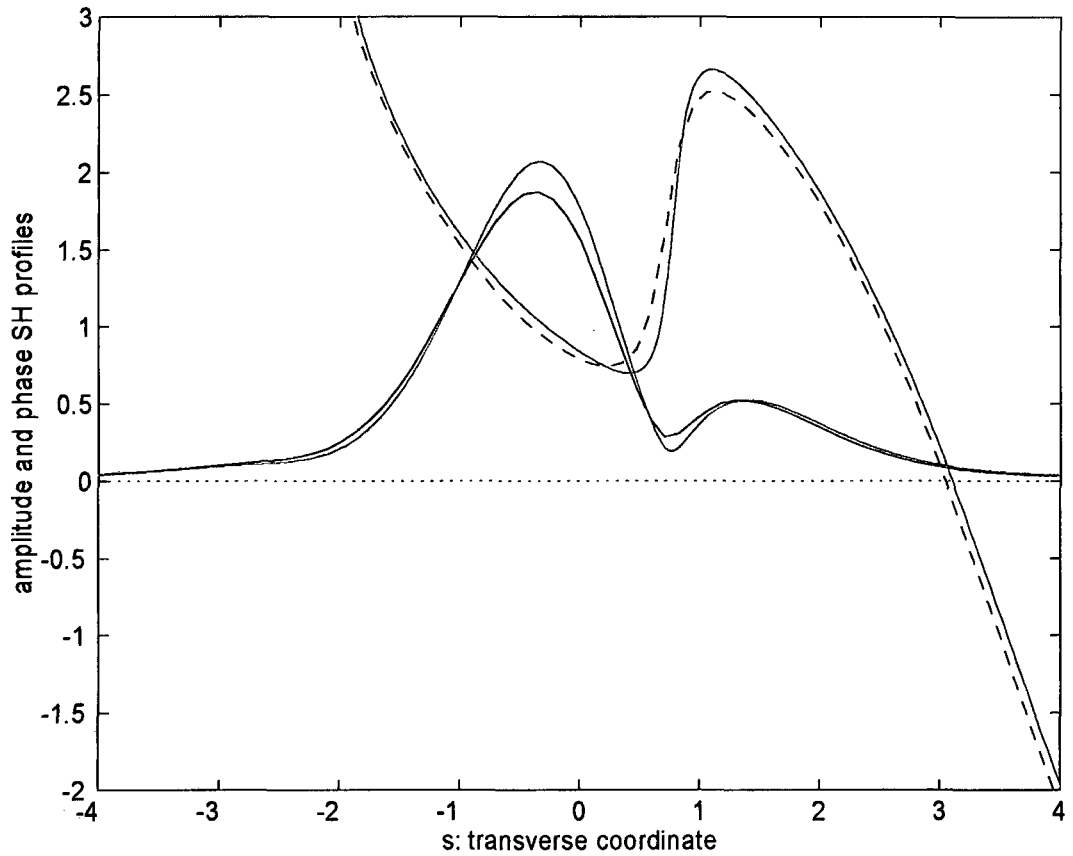
Figure 6-27: SH amplitude and phase profiles for $\xi = 0.05$ for the same case as previous figure, top row, as obtained from the numerical bpm ('b'), and using the approximation of undepleted fundamental ('m').

Soliton steering for other values of the wavevector mismatch is illustrated by the plots in Fig 6-28. The previous analysis explains worst steering but more energy coupled to the soliton for $\beta = 10$ because being the initial amplitudes closer to the values for the stationary solution in this case, the influence of radiation is minimized.

As usual it will be the requirements of any given practical application to decide whether one needs to save energy and hence would rather choose a large mismatch value or should worry further about achieving a significant soliton deviation whereupon a lower β value should be pursued.

To complete the analysis of the wavevector mismatch dependence, the case of zero wavevector mismatch configurations is also analyzed using the plots in Figure 6-29.

As expected, the slowness of the nonlinear interaction causes a lot of radiation of both signs resulting in an almost constant steering with also almost constant energy coupled to the soliton for initial tilt values above $\mu \simeq 2.5$ very becoming for practical applications because no precise control of the input angle is required, allowing even its use as an angle stabilizator. The sudden drop in soliton energy accompanied by significant enhancement of the steering observed in the plots was confirmed to steam from formation of another less energetic soliton travelling to the right.

The case of tilted fundamental beams was also investigated setting $\beta = 3$ yielding the results in Figure 6-30.

Being the initial energy exchange imposed by the tilt second harmonic to fundamental at the $s < 0$ part of the profiles, soliton deviation is expected to result reduced for $A_1/A_2 > A_1/A_2|_{STAT}$ while enhanced for $A_1/A_2 < A_1/A_2|_{STAT}$, just as the plots show. It is worth emphasizing the fact that because the momentum acquired by asymmetric radiation produced for lower A_1/A_2 relations introducing lower total momentum into the system and therefore expected to yield slower solitons, enhances the momentum finally coupled to the soliton formed, an almost constant output soliton position is obtained almost regardless the initial A_1/A_2 considered.

Next the case of negative phase mismatch configurations is briefly examined.

First, attention is focused to the case in which the tilt is applied to the weaker beam which for the sake of energy efficiency needs to be the fundamental. The results in Figure 6-31 quite
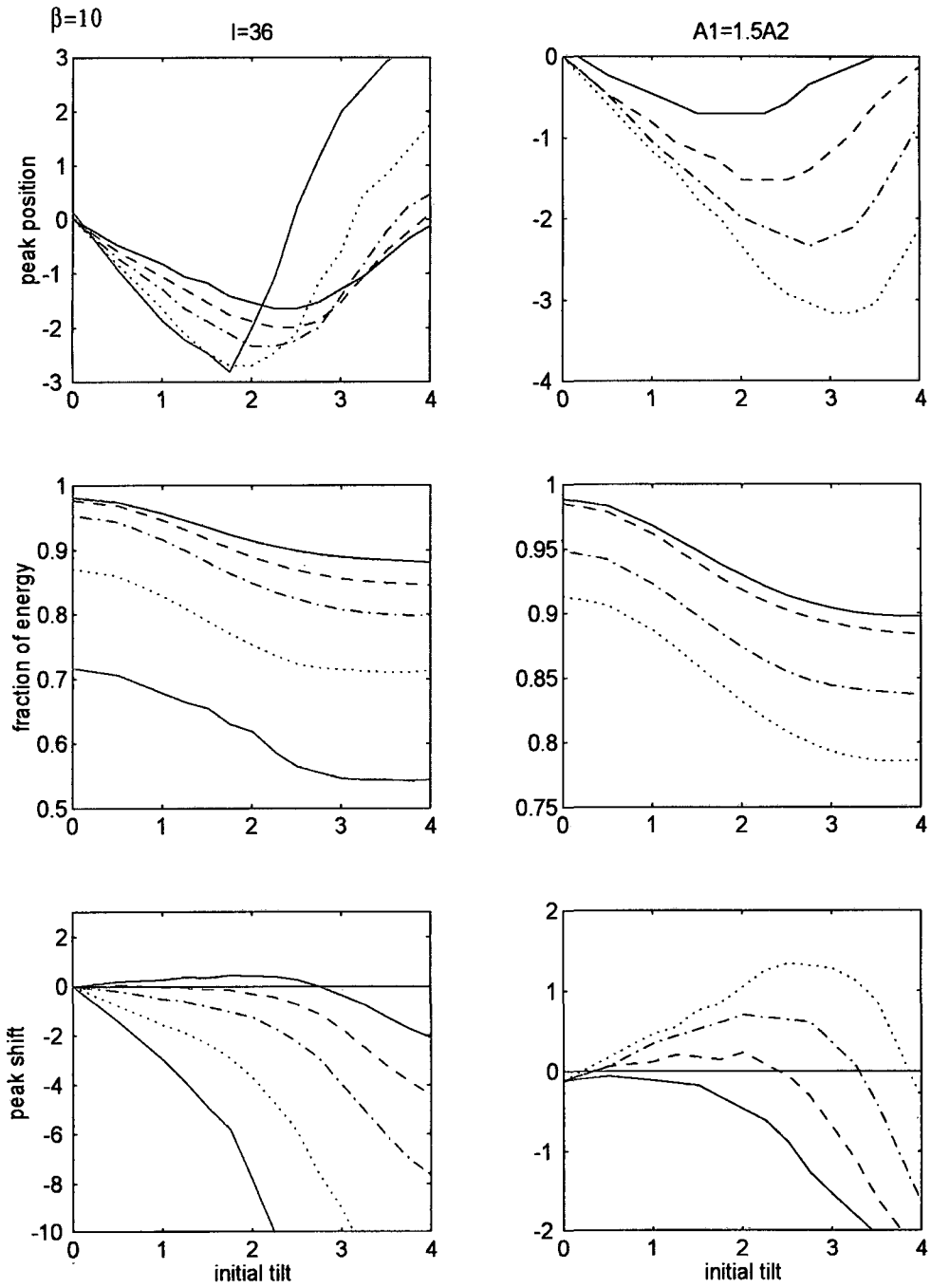
Figure 6-28: Features of the steering for $\beta = 10$. Left: ('g' lines): $A_1 > A_2$; ('m' lines): $A_1 \leq A_2$; ('g'-): $A_1 = 4.12$, $A_2 = 1$; ('g'- -): $A_1 = 4$, $A_2 = 1.4$; ('g'-.): $A_1 = 3.85$, $A_2 = 1.8$; ('g':): $A_1 = 3.5$, $A_2 = 2.4$; ('m'-): $A_1 = A_2 = 3$. Right: same as in Figure 6-23. Color scale as in App. B.
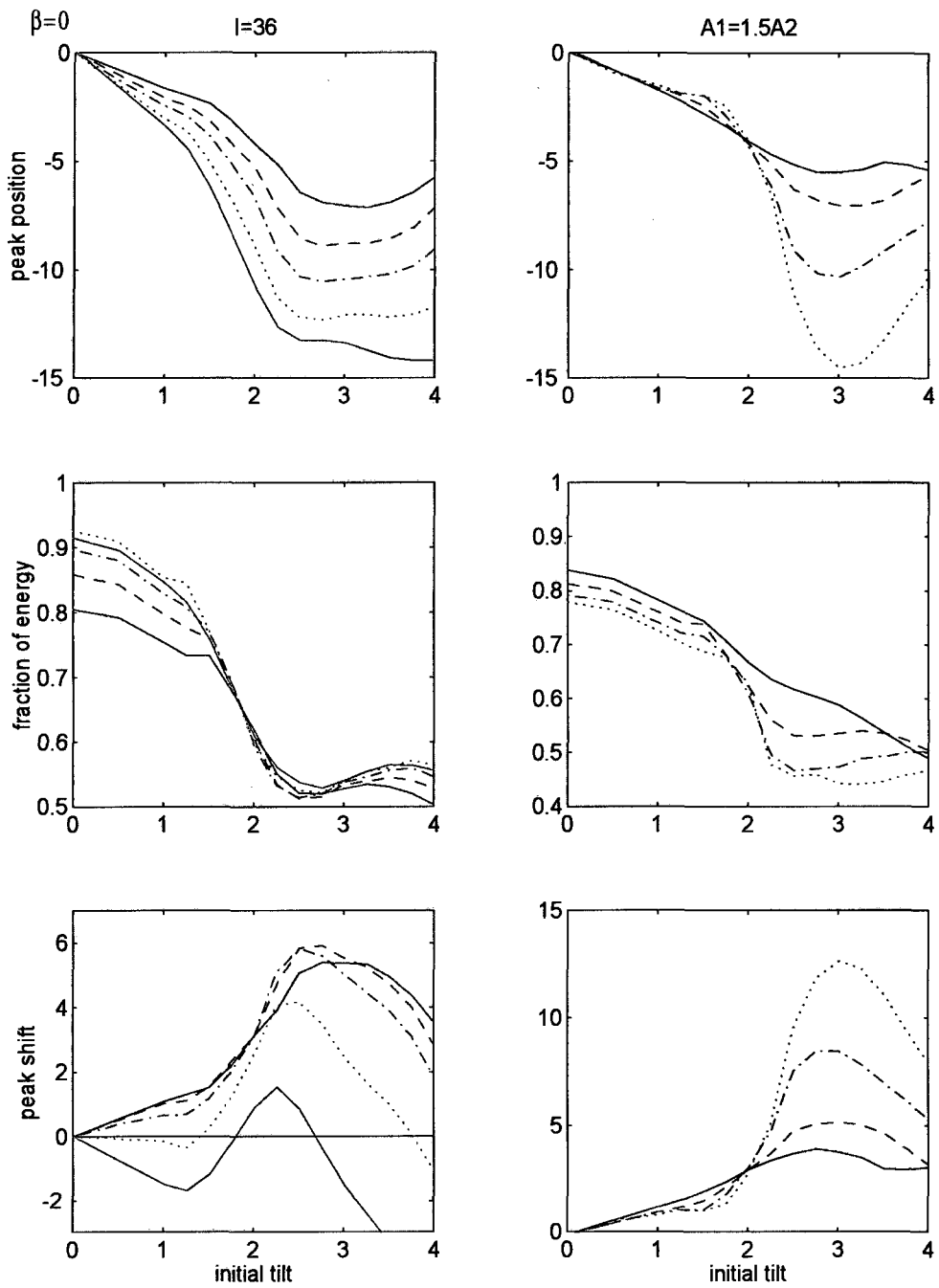
Figure 6-29: Features of the steering for $\beta = 0$. Left: ('g'-): $A_1 = 4.12$, $A_2 = 1$; ('g'- -): $A_1 = 4$, $A_2 = 1.4$; ('g'-.): $A_1 = 3.85$, $A_2 = 1.8$; ('g':): $A_1 = 3.5$, $A_2 = 2.4$; ('m'-): $A_1 = A_2 = 3$. Right: same as in Figure 6-23. Color scale as in App. B.
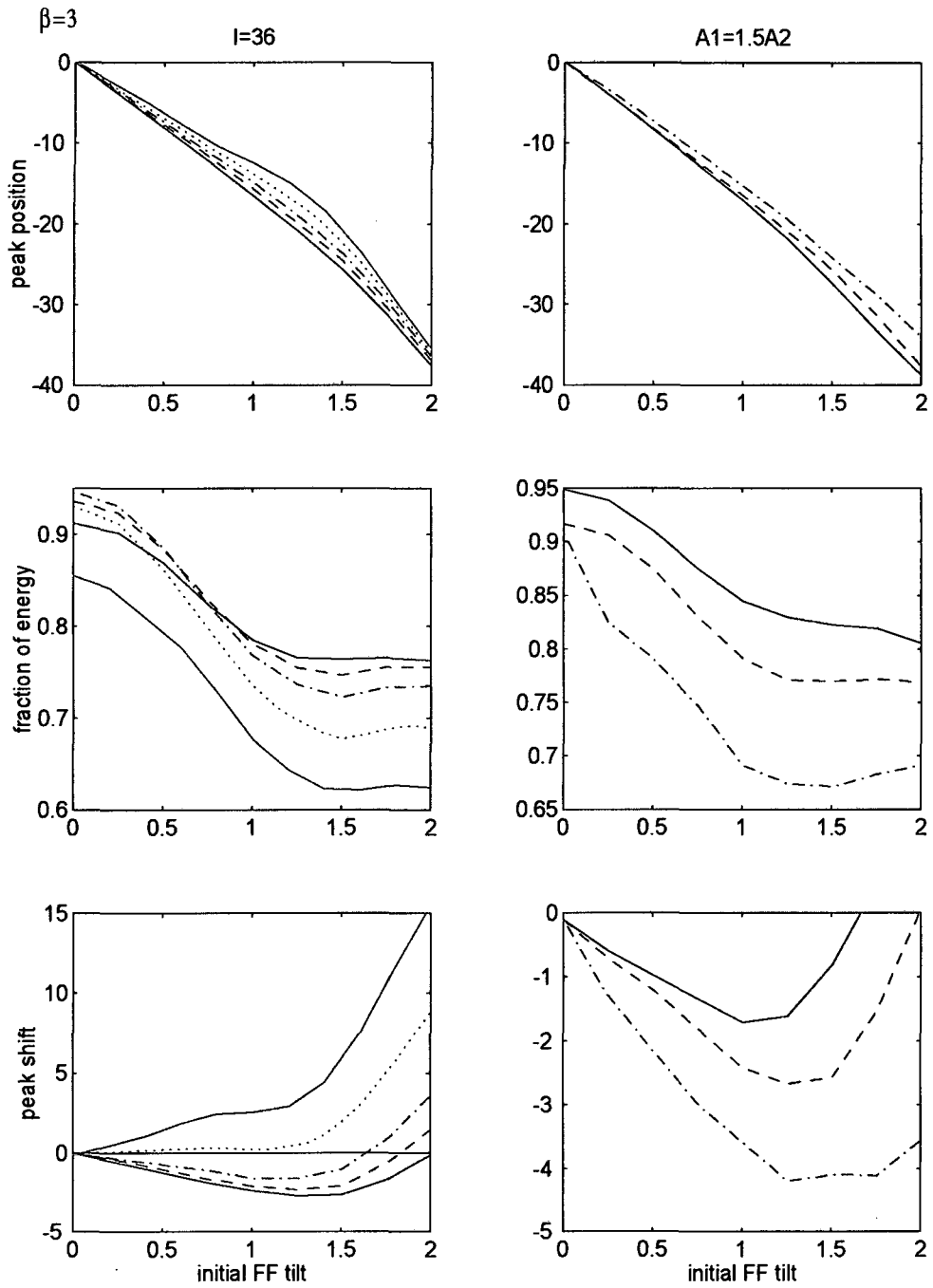
Figure 6-30: Features of the steering with tilted fundamental and $\beta = 3$. Left: ('g'-): $A_1 = 4.12$, $A_2 = 1$; ('g'- -): $A_1 = 4$, $A_2 = 1.4$; ('g'-.): $A_1 = 3.85$, $A_2 = 1.8$; ('g':): $A_1 = 3.5$, $A_2 = 2.4$; ('m'-): $A_1 = A_2 = 3$. Right: same as in Figure 6-23. Color scale as in App. B.
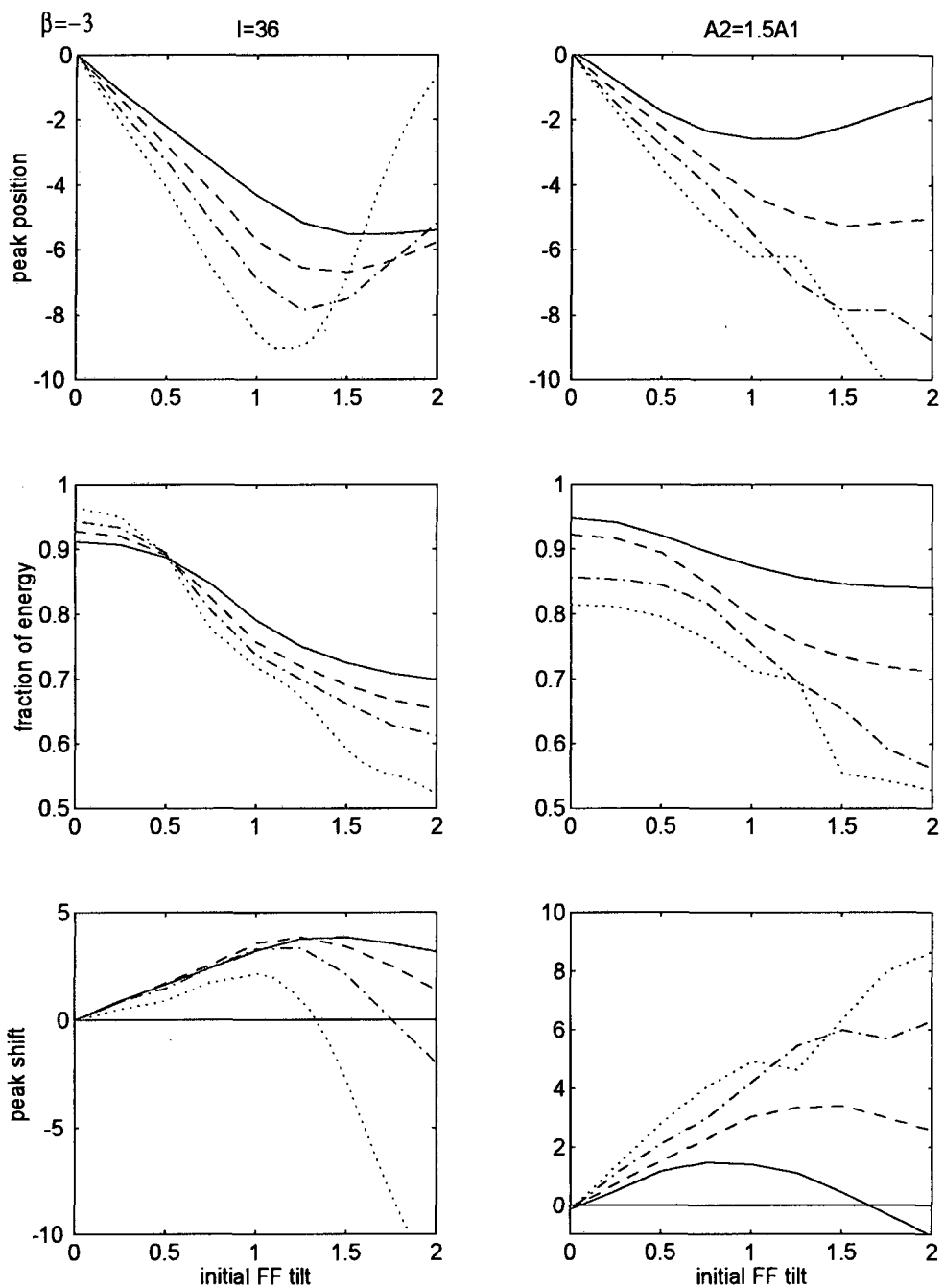
Figure 6-31: Features of the steering with $\beta = -3$, and tilted fundamental. Left: ('g'-): $A_1 = 1$, $A_2 = 4.12$; ('g'- -): $A_1 = 1.4$, $A_2 = 4$; ('g'-.): $A_1 = 1.8$, $A_2 = 3.85$; ('g':): $A_1 = 2.4$, $A_2 = 3.5$. Right: same as in Figure 6-23. Color scale as in App. B.

closely resemble those in Figure 6-23 featuring as well an optimum initial tilt value in terms of soliton deviation obtained which decreases as the momentum injected into the system increases as a result of easier weak beam escaping from the interaction with the non-tilted strong beam. Also better soliton velocity enhancement is achieved through the action of asymmetric radiation when the initial amplitude relation falls further away from the stationary value, that is, the A_1/A_2 amplitude relation increases.

When the tilt is imposed upon the second harmonic the dynamics of soliton formation in the less versatile negative wavevector mismatch case results severely obstructed by the asymmetric energy exchange pattern, so that for high values of the tilt only the use of initial amplitude relations very close to the stationary values allows for neat soliton formation.

The dramatic influence of the sign of the phase front on the final position of the soliton makes interesting the following study of the effect of an initial constant phase mismatch between harmonics ϕ_o. That influence is manifested even when no initial transverse phase variations are imposed into neither of the harmonics, i.e. the system possesses zero momentum, by splitting the beams in the case $\phi_o = \pi$ (Figure 6-32). Such an splitting is due to the change in sign of the phase front distortion undergone by the two harmonics in the initial steps of propagation which leads to opposite travelling energy fluxes at each side of the $s = 0$ point.

The numerical results obtained for different values of the initial relative phase imposed between harmonics, ϕ_o, in Figure 6-33 evidence a change in the soliton shift dependence with respect to the initial tilt which basically consists in an improvement of output position discrimination for $\phi_o < 0$ and a tendency to reduce it even leading to solitons deviation towards the opposite side as that pointed by the initial tilt for $\phi_o > 0$.

Qualitative understanding comes from evaluation of the effect of the initial phase difference in both the transverse energy exchange zones and in the initial phase front distortion undergone by the initially tilted beam.

For a negative ϕ_o value this effect is on one side to bring the zone of initial detrimental energy exchange (second harmonic to fundamental) from the right hand side to the center of the field profiles causing an increase of the energy that results radiated to the right, and in the other side, that the transversal coordinate at the $s > 0$ side of the profiles where the function $Sech(s)\cos(\mu s - \phi_o)$ that approximates the transversal dependence of the phase front
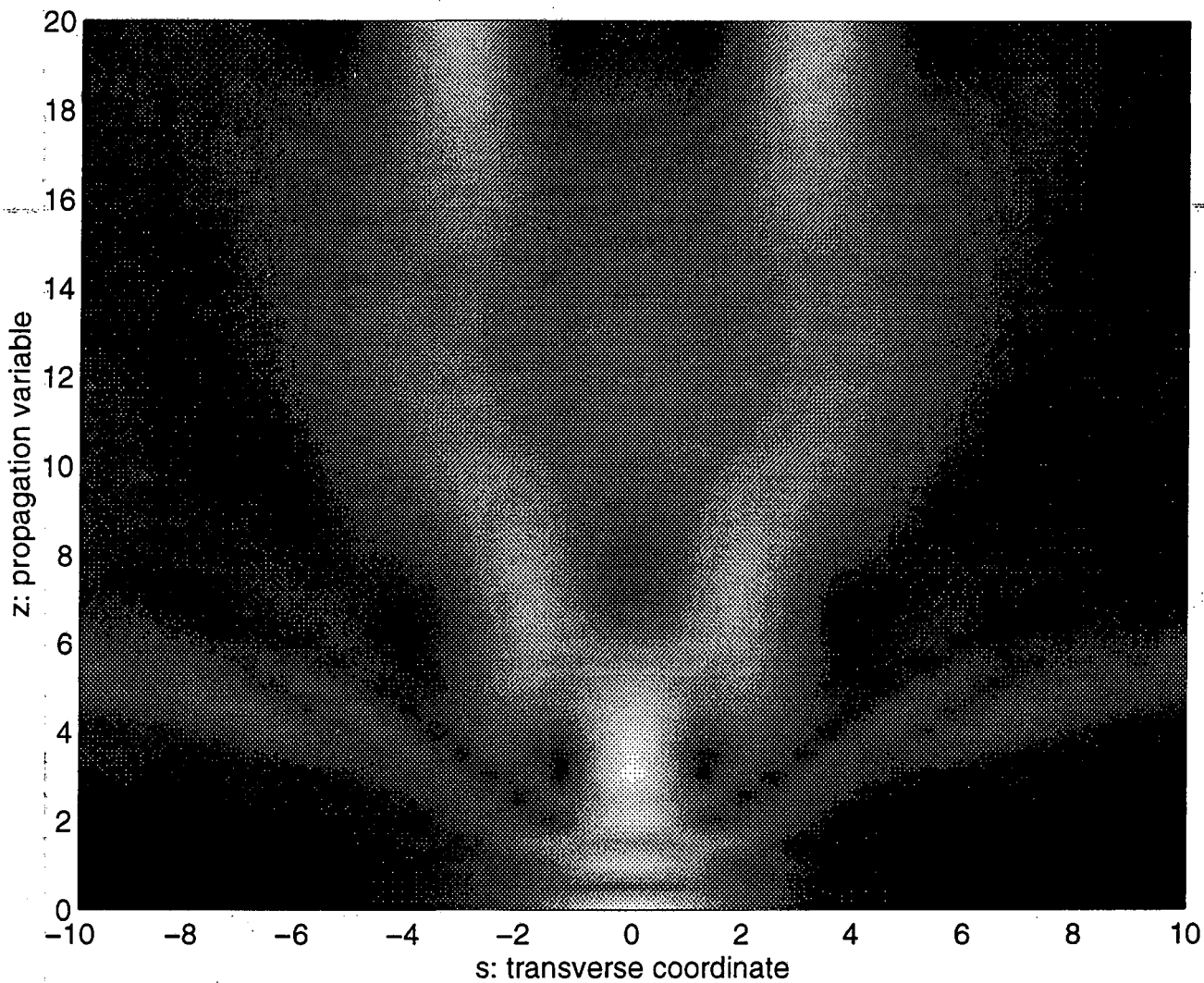
Figure 6-32: Example of splitting due to initial phase differences between the harmonics. Here $\phi_0 = \pi$, $\beta = 3$, $A_1 = 4$, $A_2 = 1$.
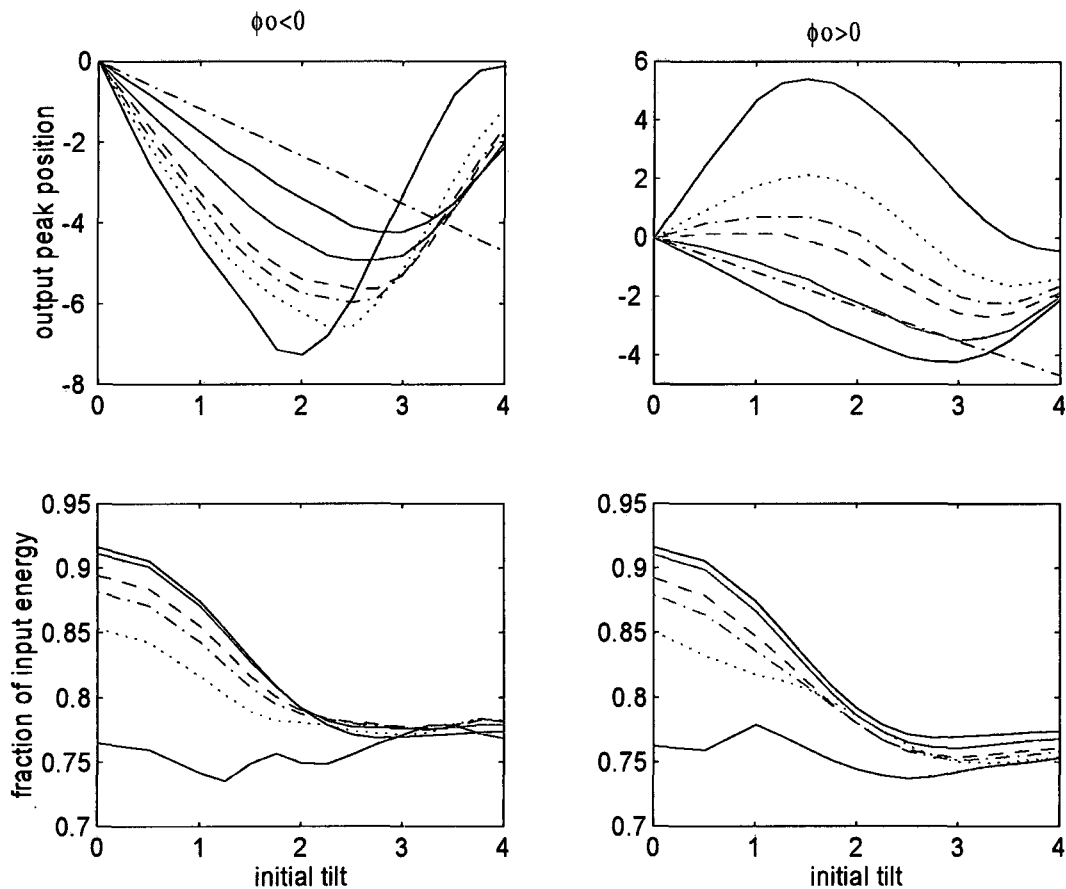
Figure 6-33: Influence of an initial phase difference between harmonics. In all cases $A_1 = 4$, $A_2 = 1$, $\beta = 3$. ('bk'-) shows the $\phi_0 = 0$ case, (bk-.) is the expected position regardless the effect of radiation. Left: ('g'-): $-\pi/10$, ('g'- -): $-\pi/5$, ('g'-.): $-\pi/4$, ('g':): $-\pi/3$, (b-): $-\pi/2$. Right: ('m'-): $\pi/10$, ('m'- -): $\pi/5$, ('m'-.): $\pi/4$, ('m':): $\pi/3$, (b-): $\pi/2$. Color scale as in App. B.

distortion undergone by the second harmonic is minimum, falls closer to the center so that the second harmonic transversal phase front gets considerably sharpened at this point conferring big velocity to the right to the radiation. Greater phase front sharpening and therefore faster right radiation leading to better steering is expected as ϕ_o is made more negative and the minimum of the function $Sech(s)\cos(\mu s - \phi_o)$ approaches the center.

As the plots in Figure 6-33 show, the value of μ for maximum steering, that is to say, the value of μ for which the inclusion of an additional zone of fundamental to second harmonic energy exchange at the $s > 0$ part of the profiles eases the coupling of energy otherwise radiated to the right, must be lower as the initial ϕ_o gets more negative since the values of ϕ_o and μ for relevant left travelling fluxe coming from the right part of the profiles have to verify

$$\phi_o - \mu d_{rfa} < -\pi, \tag{6.11}$$

where d_{rfa} gives the distance from the center of the profiles for a point at the $s > 0$ area to be affected by relevant field amplitudes. That is actually the tendency shown in Figure 6-33.

Following this line of reasoning, when positive initial phase differences between harmonics are considered, the area of energy exchange from second harmonic to fundamental is pushed away from the center of the profiles so that less energy can escape to the right with ensuing steering reduction. As about the phase distortion that results from the nonlinear interaction between the two harmonics and whose transversal dependence is mainly given by the function $Sech(s)\cos(\mu s - \phi_o)$, the addition of a positive ϕ_o moves its minimum at the $s < 0$ side of the profiles so that it progressively gets closer to the center thus leading to more energy radiated to the left while coupling more energy to the right coming from the maximum of $Sech(s)\cos(\mu s - \phi_o)$ getting further away from the center to the $s > 0$ part of the profiles. That is the situation for low values of μ leading to impairment of the steering with respect to the case of harmonics in phase and even soliton deviated to the right.

Bigger values of μ, starting from approximately $\mu = 0.6$, cause radiation to the right to slightly increase as the maximum of $Sech(s)\cos(\mu s - \phi_o)$ returns slowly to the center of the profiles resulting in smoothing of the curve giving greater deviation to the right for the soliton as μ increases. Naturally this swinging of the maximum of the transverse phase front profile

also occurs but in a symmetrical way for $\phi_o < 0$, but its effects there are not that evident since it follows the natural tendency of the steering.

A change in tendency, i.e. greater deviation to the left as μ increases is then observed coming from an increase in the velocity of radiation to the right as the minimum of the function $Sech(s)\cos(\mu s - \phi_o)$ at the $s > 0$ part reaches a significant field amplitudes area and progresses towards the center of the profiles. Further increases of μ cause the point for $\phi_2 = -\pi$ to fall in an area of relevant field amplitudes and couple some of the energy at the $s > 0$ part so that it is no longer radiated. The transverse left travelling soliton results thus slowed down and the tendency of the steering changes again to give soliton more deviated to the right as μ increases starting around $\mu \simeq 3$. The following relationship

$$\phi_o - \mu d_{rfa} < -\pi$$

approximately holds for the values of ϕ_o and μ for which significant coupling of energy at the right part of the profiles takes place.

To complete the analysis of steering control through input tilted beams the effect of a certain Poynting vector walk-off is briefly investigated.

The differentiate nature of Poynting vector walk-off and initial tilts as mechanisms to produce soliton deviation is illustrated in the plots in Figure 6-36. While the former as determining a more probable direction inside the material whereupon it acts directly upon the governing equations, gives rise to a clear and robust steering tendency, the latter as relying only upon initial conditions is susceptible of being strongly modified through the dynamics and hence is more fragile.

Since the energy introduced into the system is continuously pulled out in the direction in which the walk-off points, the effect of initial tilts is through the dynamics progressively minimized so that the range of soliton output positions obtained by changing the initial tilt gets reduced and hence so gets the performance of an steering device based on angle control. However as seen, if the walk-off is kept within moderate values on the range $\delta \sim 1$ and the device is operated so that the tilted input beam points in the same direction of the walk-off, a good output position discrimination is obtained.
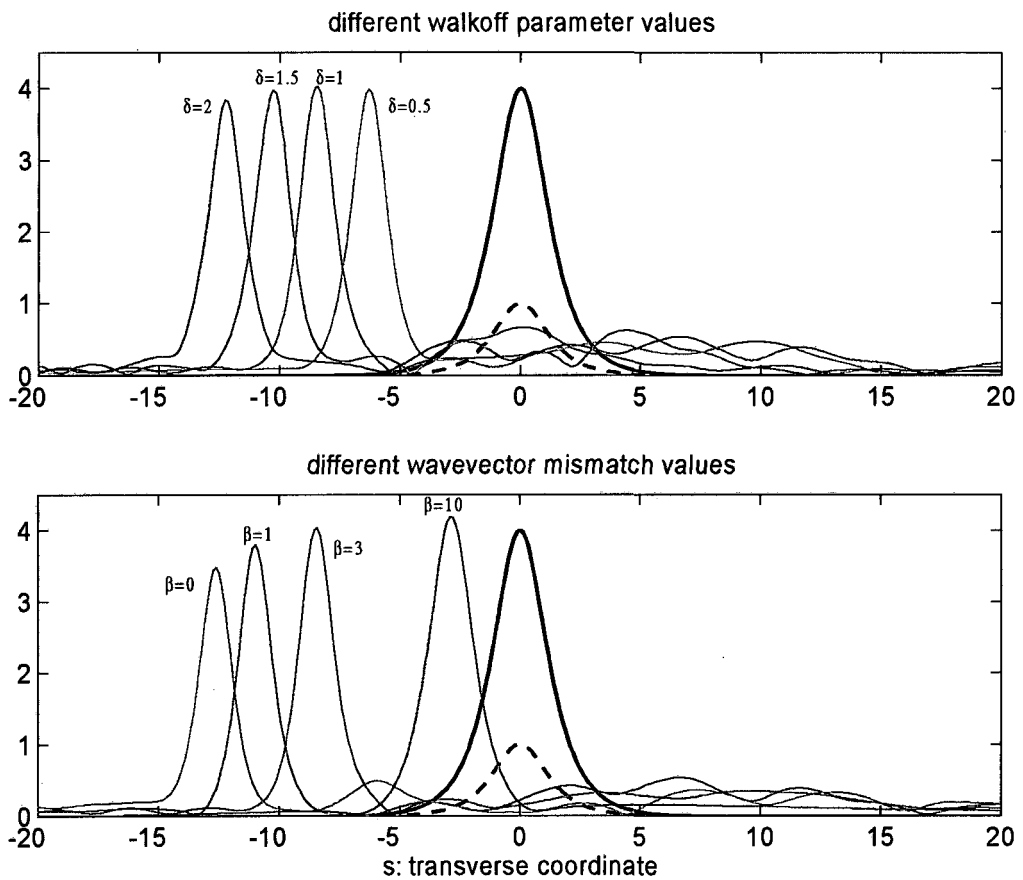
207

Figure 6-34: Examples of steering with both initial tilt on SH and some walk-off. Black thick lines show input amplitude profiles while colored ones are the outputs at fundamental frequency found at 40 diffraction lengths. In both cases $A_1 = 4$, $A_2 = 1$, $\mu = 3$. Top: different δ values with $\beta = 3$. Bottom: different β values with $\delta = 1$.
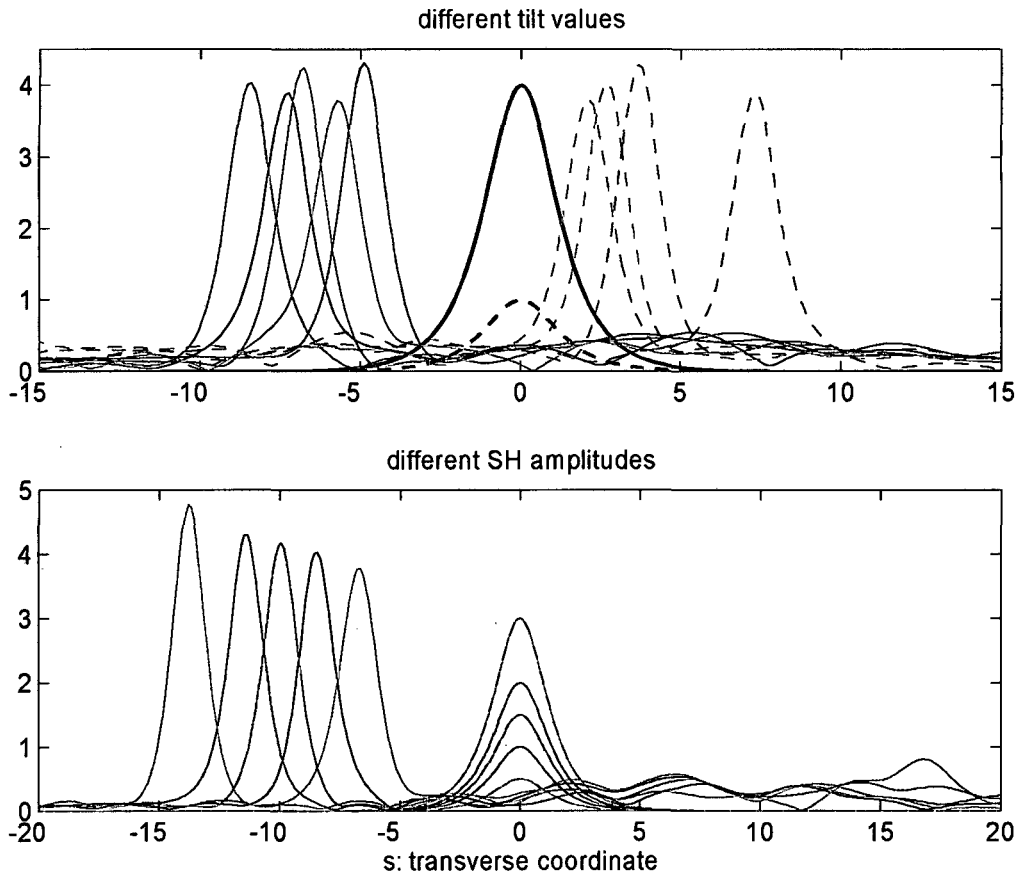
208

Figure 6-35: Same as previous figure showing power and angle control of the steering. In both cases $A_1 = 4$, $\beta = 3$. Top: $A_2 = 1$; (-): $\delta = 1$,(-.): $\delta = -1$; 'bk': 'b':$\mu = 0$, $\mu = 1$, 'g': $\mu = 2$, 'r': $\mu = 3$, 'c': $\mu = 4$. Input profiles shown in black thick lines with (-) for FF and (- -) for SH. Bottom: $\mu = 3$, $\delta = 1$ and input second harmonic as shown by the corresponding black and colored line. Color scale as shown in App. B.
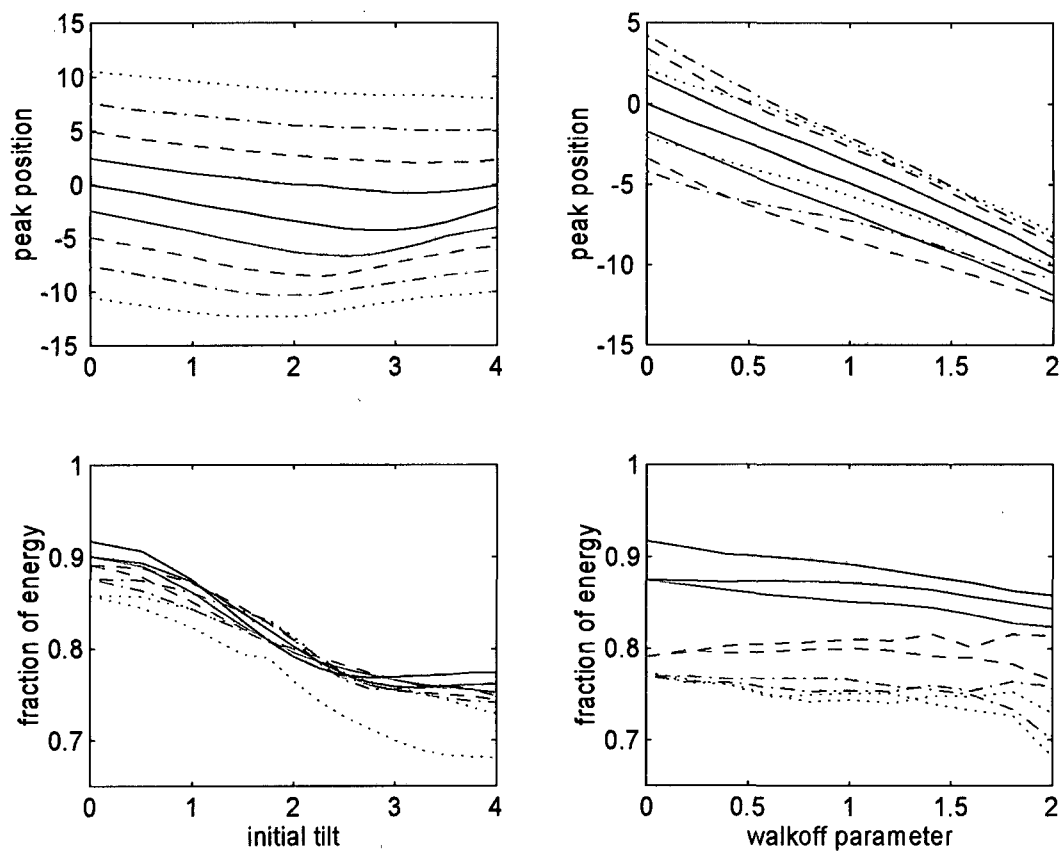
209

Figure 6-36: Effect of some walk-off on input tilts steering. In all cases $A_1 = 4$, $A_2 = 1$, $\beta = 3$. Left $\mu = 3$; ('g'-): $\delta = -0.5$, ('g'- -): $\delta = -1$, ('g'-.): $\delta = -1.5$, ('g':): $\delta = -2$, ('m'-): $\delta = 0.5$, ('m'- -): $\delta = 1$, ('m'-.): $\delta = 1.5$, ('m':): $\delta = 2$. Right $\delta = 1$; ('g'-): $\mu = 1$, ('g'- -): $\mu = 2$, ('g'-.): $\mu = 3$, ('g':): $\mu = 4$, ('m'-): $\mu = -1$, ('m'- -): $\mu = -2$, ('m'-.): $\mu = -3$, ('m':): $\mu = -4$. Color scale as in App. B.

As increasing the transverse velocity initially acquired by the second harmonic, positive δ values ease its escaping away from fundamental resulting in the decrease in energy efficiency and the drop of the maximum steering initial tilt value observed in the plots. On the other side negative δ values as initially slowing down the transverse velocity induced into the second harmonic cause an increase in the maximum steering initial tilt value.

As regarding power control of the steering the soliton output position stabilization effect produced in the presence of walk-off shows interesting implications. It is observed that when the input tilt points in the direction opposite to that determined by the walk-off, the soliton output position basically depends only on the fraction of energy contained into the second harmonic and not on the total energy introduced into the system and it is so in a significant range of wavevector mismatches and with energy efficiencies within reasonable levels. This is good news as for the building up of real devices since one needs not worry about the total power introduced into the system but only about the fraction of this power corresponding to second harmonic which significantly eases the practical setup required.
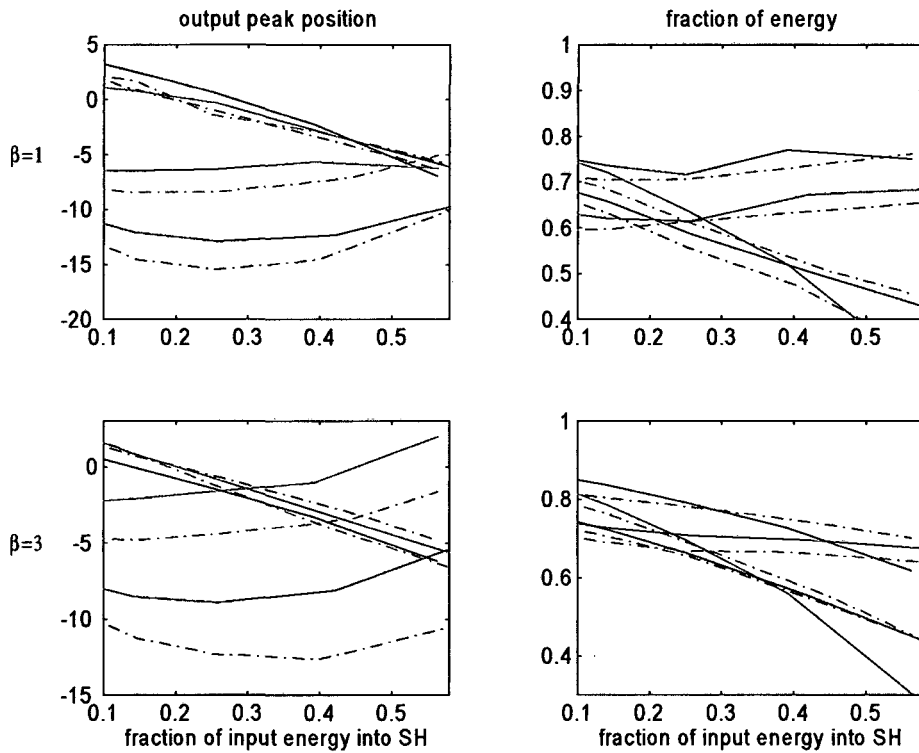
Figure 6-37: Effect of some walkoff on power controlled steering for $\beta = 1$ (top) and $\beta = 3$ (bottom) and different power values. In all cases $\mu = 3$. $\delta = -1$ (g-): $I = 8$, (g- -): $I = 18$, (g-.): $I = 36$, (g:): $I = 50$. $\delta = 1$ (m-): $I = 8$, (m- -): $I = 18$, (m-.): $I = 36$, (m:): $I = 50$. Color scale as in App. B.

6.2.2 Conclusions

Soliton steering through input weak tilted beams has been analyzed in this section. Although the main effects have been shown to occur also in negative wavevector mismatch configurations, the study has concentrated on $\beta > 0$ setups in which a weak tilted second harmonic beam is used to control the soliton steering. The expected transverse velocity of the soliton, v, is given by

$$v = -\frac{\mu}{2}\frac{I_2}{I},\tag{6.12}$$

where μ is the initial second harmonic tilt value, and I_2 and I respectively the second harmonic and total energy flows. From the observations, the following remarks have been selected as conclusions.

Regarding soliton steering controlled through initial angular tilts:

- small values of the initial tilt, μ, produce through the initial energy exchange asymmetry some radiation whose direction opposes that of the tilt and hence enhance soliton deviation while big μ values ease the second harmonic walking the fundamental off before efficient nonlinear interaction allowing for momentum sharing has taken place thus reducing the soliton shift;

- the initial tilt value for maximum soliton deviation ,μ_{opt}, depends on the behavior of radiation so that basically:

$A_1/A_2 \downarrow$		$\mu_{opt} \downarrow$ (and more marked tendency as $\beta \uparrow$)
$\beta \uparrow \longrightarrow I_1/I_2\vert_{STAT} \uparrow$	(SH finds it easier to walk FF off)	$\mu_{opt} \downarrow$
$I \uparrow \longrightarrow I_1/I_2\vert_{STAT} \downarrow$	(FF manages to control SH initially)	$\mu_{opt} \uparrow$

,

- soliton shifts of around 5 beam widths,η, with energy efficiencies, $I_{SOLITON}/I_{INPUT} \sim$ 0.8, have been shown to be achieved with initial tilt values up to $\mu = 4$, corresponding for typical conditions, i.e. $\lambda \sim 1\mu m$ and $\eta \sim 15\mu m$, to input angles of about $\theta \sim 1 - 2^0$,

wavevector mismatches within the range $\beta \sim 0 - 10$, and normalized energy flows up to $I \sim 70$.

As for power controlled steering, it is woth remarking that increases of total energy flow as reducing the nonlinear interaction length ease the interharmonics initial coupling of momentum, thus increasing the soliton velocity. The increase is less evident for initial high A_1/A_2 amplitude relations as an energy flow increase entails a reduction in the $I_1/I_2|_{STAT}$ value. The soliton deviations obtained were on the range of 10 beam widths with normalized input powers up to $I \sim 50$, input angles about $\theta \sim 1^0$ and wavevector mismatches within the range $\beta \sim 0 - 10$.

Wavevector mismatch dependence for the inputs of interest in this section, namely $A_1/A_2 \downarrow$ is summarized through,

$$\beta \uparrow \longrightarrow I_1/I_2|_{STAT} \uparrow \quad \begin{array}{c} \text{(little effect} \\ \text{of radiation)} \end{array} \longrightarrow \begin{array}{c} v \downarrow \\ I_{SOLITON}/I_{INPUT} \uparrow \end{array} .$$

The effect of initial phase differences between the harmonics, ϕ_0, was shown to verify:

- for $\phi_0 < 0$, basically same dependence curve as for in phase inputs with better soliton output position discrimination.

- or $\phi_0 > 0$, less output soliton position discrimination and different dependence curve with respect to input tilt. The soliton may even be found travelling against the initial tilt.

Moderate Poynting vector walk-off, δ, values pointing in the same direction as the tilt yield good output position discrimination when the initial tilt angle is used as the control of the steering, while when the fraction of power in the second harmonic is the control parameter, opposite directions determined by δ and μ cause the soliton deviation to be independent of the total power injected into the waveguide.

6.3 Input gratings

Right after angular tilts the simplest practical way of having a beam phase modulated one can think of is through the use of phase gratings.

Gratings are periodic structures which find many applications in optics technology such as mode coupling, spectroscopy or holography among others. The wavelength of light incident upon the grating, λ, relative to the periodicity of the grating, Λ, and to the grating depth, d, which represents the distance between the grating's input and output (see Figure 6-38), determines the grating's mode of operation. When $d << \Lambda^2/\lambda$, the grating is said to operate in the *Raman-Nath* or *optically thin* grating regime. In this case no significant wave interaction occurs inside the grating and all diffraction orders are produced. Conversely, when the grating is operated in *Bragg* regime, due when $d >> \Lambda^2/\lambda$, multiple diffractions occurring inside the grating favour certain angles of propagation. As a result, two main diffraction orders are found after the grating which is then said to be *optically thick*. Filters, spectroscopes and angle selectors make use of the latter mode of operation, while optically thin gratings are preferred to act upon the wave phase without affecting the spatial power distribution [153]. Clearly enough then, the choice in the steering experiments shall be optically thin gratings.

Defined as a *periodical structure*, the grating concept englobes a wide variety of systems among which the most popular are *diffraction gratings* such that the diffraction orders after the grating are achieved by making the wave go through an array of transparent slits periodically spaced in a non-transparent material, and *phase gratings* featuring a periodic variation of refractive index. The latter offers a wider variety of different spatial phase modulations of the incident beam and in particular sinusoidal-like spatial modulations are rather easily obtained.

Hence in this section, assuming an *optically thin phase grating* arranged in a direction perpendicular to that of fields incidence is located at the input face of the quadratically nonlinear planar waveguide as Figure 6-38 shows, the solitary waves steering control and dependence upon the system and input main parameters are studied.

In a first subsection, the characteristics of practically feasible gratings are revised with an eye to determine useful ranges for normalized parameters to be used in the simulations, for then move on to a brief analytic study of the possibilities offered by sinusoidal spatial modulations and its implications to the steering of solitary waves existing in quadratically nonlinear media.
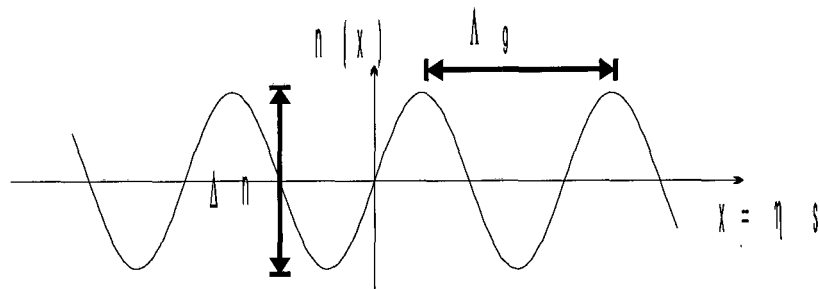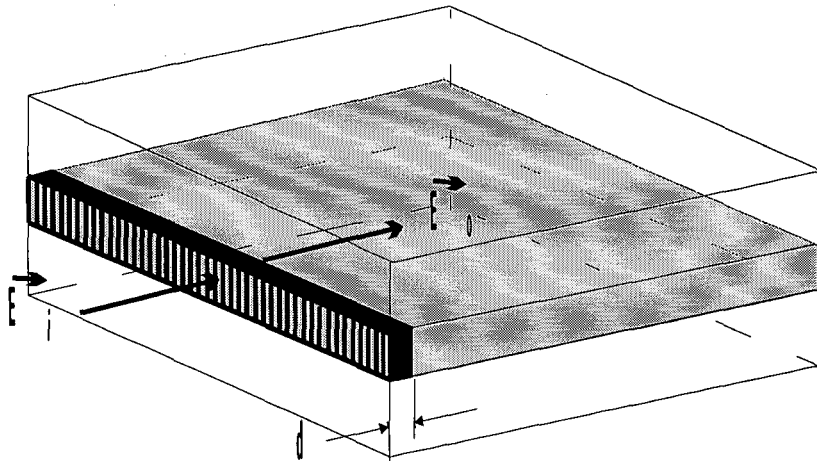
Figure 6-38: Sketch of the practical setup simulated in the numerical experiments showing the input phase grating with indication of its main parameters (top) and the typical refractive index distribution (bottom).

Last section presents the results of the numerical simulations and the section is ended up with some conclusions.

6.3.1 Gratings fabrication and main parameters

A wide variety of methods can be used to construct a phase grating. All that is required is the effective index be varied periodically. In the simulations presented here the periodic function followed by the refractive index distribution will be assumed to have sinus-like variation as sketched in Figure 6-38, illustrating as well the main parameters defining a grating, namely the *refractive index difference* Δn, the *spatial period* Λ, and the *grating depth* d. The relation between the fields just before the grating, E_i, and just after the grating, E_o, is expressed through

$$E_o\left(x, z = d\right) = E_i\left(x, z = 0\right)\exp\left(j\phi\left(x\right)\right) = E_i\left(x, z = 0\right)\exp\left(jk\Delta nd\sin\left(2\pi\frac{x}{\Lambda} + \theta_0\right)\right), \quad (6.13)$$

where k is the propagation constant of the input light and θ_0 accounts for shifts of relative position between fields beam peak and the zeros of the sinusoidal function defined by the refractive index.

In the simulations use is made of normalized quantities so that the phase modulation is expressed

$$\phi\left(x\right) = \phi_A\sin\left(2\pi ps + \theta_0\right), \quad (6.14)$$

where s is the usual normalized quantity for the transverse coordinate such that $s = x/\eta$, with η beam width, and p represents the normalized spatial frequency of the grating. The relation between normalized parameters in the simulation and real parameters follows

$$\phi_A = 2\pi\Delta n\frac{d}{\lambda}, \quad (6.15)$$

$$p = \frac{\eta}{\Lambda}. \quad (6.16)$$

The condition for Raman-Nath type diffraction actually sets a limit on the amplitude of the phase modulation that such structures may achieve through restriction to grating depths that verify $d << \Lambda^2/\lambda$, that is $d << \eta^2/\left(\lambda p^2\right)$, which under typical conditions, say $\eta \simeq 15\mu m$ and $\lambda \simeq 1\mu m$ for p values on the order of $p \simeq 0.2$, as used in the simulations, means $d \lesssim 1mm$.

217

However in practice the grating should be even shorter, on the other of a wavelength or so, for the change in refractive index not to affect significantly the fields propagation through for instance alterations in the β value.

If simply the input face of the crystal is etched through the use of a patterned mask, made up perhaps of a photolythographic material illuminated through holographic interference as Figure 6-39 shows, one obtains a *corrugated grating*. The refractive index difference in this case equals the refractive index of the material upon which the grating has been written so that $\Delta n = n_0 > 1$ and practically there is no restriction on the amplitudes of the phase modulation that can be achieved.

Other methods as *in-diffusion* of dopants or *ion-exchange* [153], although no such accurate refractive index distribution is achieved, may also be used to write the phase grating at the input face of the material.

Anyway whether corrugated or in-diffused, once the grating writing process ends, little chances save going through the whole process again to alter its properties are left. Hence, these written gratings will be considered in the simulations as a means of steering control through the power contained in the input harmonics.

Another technique for the writing of gratings takes advantage of both the *photoconductive* and the *Pockels or electro-optic effect* present together in many materials used in photonics technology such as for example $LiNbO_3$ which thus are known as *photorefractive materials*. Two interfering light beams incident upon the materials' surface create an optical field distribution which through the photoconductive effect is reproduced by the distribution of bound charges which thus creates a static electric field affecting the refractive index distribution through the Pockels effect. Needles to say, care should be taken to ensure that the working wavelengths fall well outside the range of significant photorefractive phenomena.

Besides an easy though slow procedure of erasing and rewriting the grating, this method provides feasibility of a wide variety of different setups if a photorefractive material with a Pockels effect which is selective in frequency is available so that significant modulation of the refractive index only affects one of the two harmonics. When this is not possible the setup shown in bottom row of Figure 6-45 is an option for getting only one of the beams phase modulated which obviously is expected to offer more inconveniences from a practical point of view.

218

Electrically switchable gratings are obtained through exploitation again of the *Pockels effect* by placing a periodic metal structure known as *interdigital electrode* on the surface of the guide. Such an arrangement gives rise to a periodic change in sign of the electric field beneath each pair of electrodes [154], [155].

Another chance to the obtention of an electrically-switchable grating is provided by combination of *piezoelectricity* and *acoustooptical* properties which luckily enough are again owned by usual optical materials such as $LiNbO_3$. The first of the properties is required for obtaining a pressure wave out of a radio frequency applied voltage while the second one determines the optical refractive index displayed by the material to vary following the sound wave electrically created. The spatial period of the grating thus obtained is $\Lambda = v_s/f$ where v_s stands for the velocity of sound in the material and f is the electric voltage radio-frequency which is in the hundreds of megahertzs. The configuration whose setup is roughly sketched in Figure 6-40 adds the possibility of the dynamic variation of both the spatial frequency and the maximum refractive index change of the grating respectively through changes in the radio-frequency in a range only limited by excessive acoustic propagation losses at frequencies above $\simeq 1GHz$, and in the power of the voltage applied [154], [155].

The following table obtained from *Chang, 1976* summarizes the properties relative to acoustooptical phenomena of some materials:

Material	$v_s\,(m/s)$	$M_2\,(10^{-12}s^3/Kg)$
Fused silica	5960	1.51
$LiNbO_3$	6570	6.95
$PbMoO_4$	3630	35.8
TeO_2	4200	34.6
$GaAs$	5150	104.19

The acoustooptical figure of merit displayed in second column, M_2, is such that the maximum optical refractive index change produced by an acoustic beam of total power P and cross section A is given by

$$\Delta n = \sqrt{M_2 \frac{P}{2A}}. \tag{6.17}$$

To get a feeling on the amplitudes of the phase modulation that can be achieved take
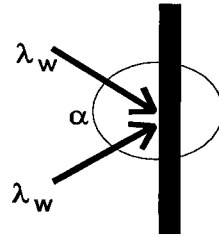
Figure 6-39: Holographic technique.

piezoelectric
+
acoustooptic
material

f,P $\rightarrow$ ACOUSTIC   OPTICAL
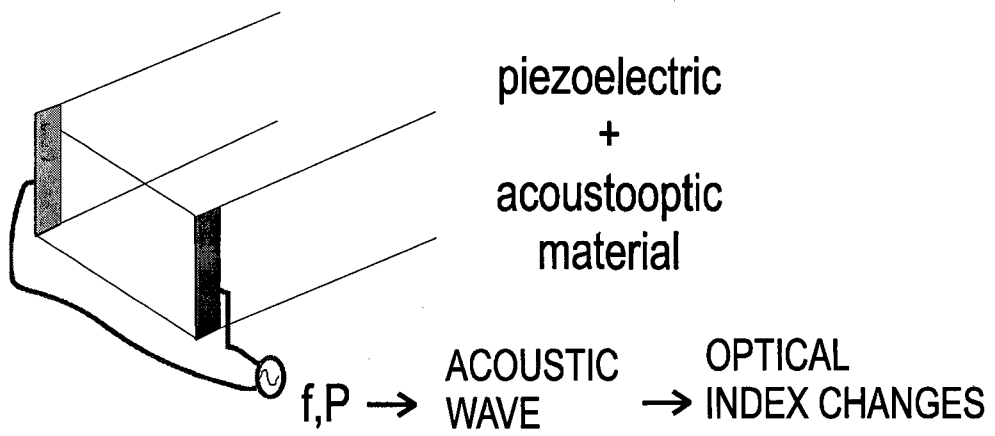   WAVE $\rightarrow$ INDEX CHANGES

Figure 6-40: Switchable grating.

$LiNbO_3$ as an example and a reasonable total acoustic power of about $P = 1W$ applied upon a rectangular cross sectional area giving a grating depth $d = 1\mu m$ and a y direction side of $l = 10\mu m$ which is enough to cover the thin quadratic nonlinear waveguide. For a light wavelength on the order of $\lambda \sim 1\mu m$ one obtains

$$\phi_A = 2\pi\frac{d}{\lambda}\sqrt{M_2\frac{P}{2(d \times l)}} = 2\pi\sqrt{\frac{6.95 \times 10^{-12}}{2 \times 10^{-11}}} \sim 3.7, \tag{6.18}$$

but other values are also achievable through variation of the acoustic power or the cross sectional area over which the stress is induced into the material.

As for an order of normalized spatial frequencies, the velocity of sound in $LiNbO_3$, $v_s = 6570m/s$, gives for a radio-frequency of about $f = 100MHz$ a spatial period of $\Lambda = 65.7\mu m$ corresponding for $\eta = 15\mu m$ to a normalized spatial frequency in the simulations of $p \sim 0.23$.

Well aware of the possibilities offered by input gratings, investigation of how the phase modulation they inflict upon the input fields affects the solitary wave formation and propagation inside the quadratically nonlinear waveguide is carried out in next section.

6.3.2 Analysis of input phase modulations

It has been shown that the net effect of placing a phase grating featuring a refractive index distribution that varies sinusoidally in the transverse direction at the input face of the $\chi^{(2)}$ planar guide is phase modulating the input beams. Following the usual notation for the normalized fields in the $\chi^{(2)}$ problem they can be expressed

$$a_i^{(g)}(s, \xi = 0) = a_i(s, \xi = 0)\exp\left(-j\phi_{A_i}\sin(2\pi p_i s + \theta_i)\right), \tag{6.19}$$

where the superindex distinguishes input fields with grating at the entrance face of the waveguide from those in the absence of grating.

By using standard Bessel function expansion of the modulation term, the input fields can also be expressed

$$a_i^{(g)}(s, 0) = a_i(s, 0)\sum_{m=-\infty}^{m=\infty} J_m\left(\phi_{A_i}\right)\exp\left(-jm(2\pi p_i s + \theta_i)\right). \tag{6.20}$$

Such an initial beam distribution when propagating in a linear medium will result splitted up in many subbeams travelling in different angles determined by tilts at multiples of the spatial frequency of the grating, $2\pi p_i$ each carrying a fraction of the total energy that depends on the Bessel function of the order of the phase tilt multiplicity evaluated at the amplitude of the phase modulation.

Conversely, in the quadratic nonlinear medium as a result of nonlinear interaction the energy tends to gather in a single subbeam chosen through the dynamics depending both in input and system parameters. The splitting up picture provided by the linear case renders useful however to understand many of the features displayed by the nonlinear propagation.

In Figure 6-41 the colored lines while pointing in the direction followed by each subbeam have modulus proportional to the fraction of initial energy they carry for a spatial frequency of $p = 0.2$. As seen the higher the multiplicity of a given subbeam the faster it walks the z axis off. Following the rule

$$J_{-m}\left(\phi_{A_i}\right) = (-1)^m J_m\left(\phi_{A_i}\right). \tag{6.21}$$

In the range of interest $\phi_{A_i} \lesssim 3.5$, the amplitude of the rays going to the right in Figure 6-41 alternate in sign whereupon interfere destructively. Basically the distribution of energy between the subbeams is characterized by a flow of energy from the straight ray towards the two first subbeams as ϕ_{A_i} increases until it is reached the $\phi_{A_i} \simeq 2.4$ value for which the two first subbeams attract practically all the energy in equal shares such that no energy goes in the straight direction. Above this value energy returns to the straight direction but now with a negative amplitude and energy is transferred to higher multiplicity orders.

Figures 6-42 and 6-43 compare the characteristics of linear and nonlinear propagation showing how helpful the linear picture results. Destructive interference of the subbeams at the right hand side of the profiles causes the energy there to be dragged up towards more energetic left hand side whose subbeams add up in constructive interference. When above $\phi_{A_i} \simeq 2.4$ the straight subbeam amplitude turns negative, the energy at the right hand side of the profiles becomes more difficult to couple to the beam created by the constructive interference of the subbeams at the left hand side and the net result is an increase in radiation to the right as the ϕ_{A_i} value is increased (Figure 6-44).

The transverse velocity with which the beam resulting from the nonlinear coupling among
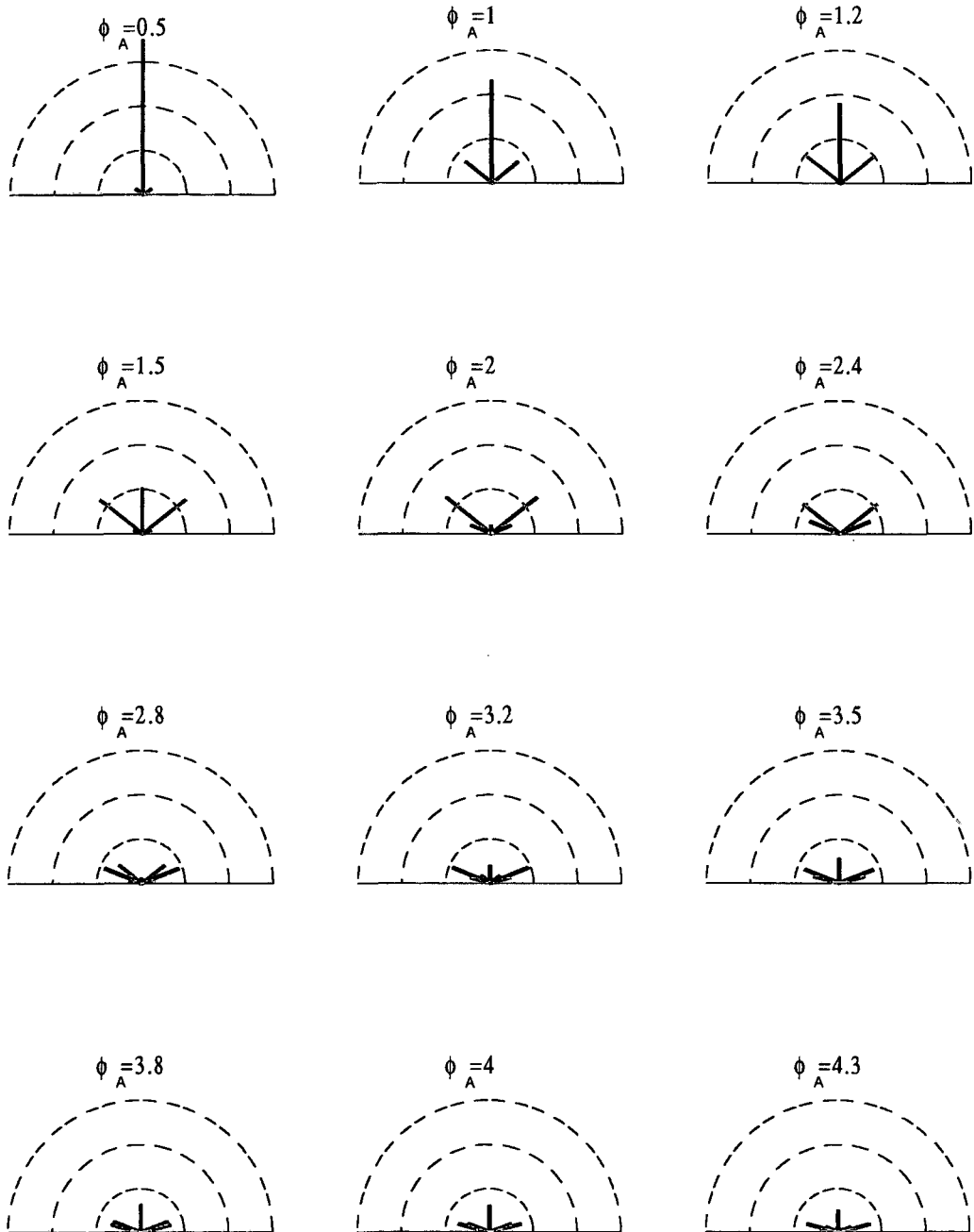
Figure 6-41: Relevant subbeams generated in a linear medium as a consequence of a sinusoidal phase modulation for various values of the amplitude of the modulation (ϕ_A). The lines show angle of propagation and have length proportional to the fraction of energy carried. Color depends on the order of the subbeam according to 0th: 'g', 1st: 'm', 2nd: 'b', 3rd: 'r' and 4th: 'c'. Color scale as in App. B. In all cases $p = 0.2$.
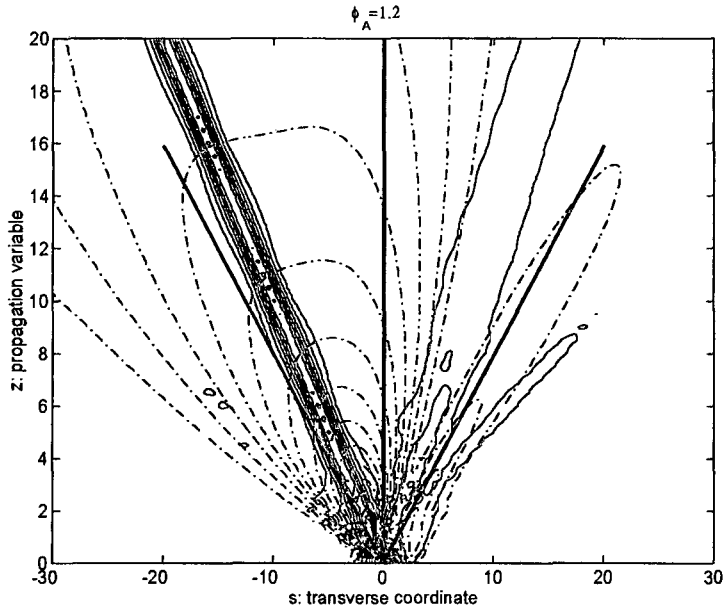
Figure 6-42: Linear ('black'-.) and nonlinear ('red'-) propagation of the fundamental field for the set of parameters $A_1 = 4$, $A_2 = 0$, $\phi_A = 1.2$, $p = 0.2$, $\beta = 3$. Straight lines indicate the direction of the subbeams in a linear medium.
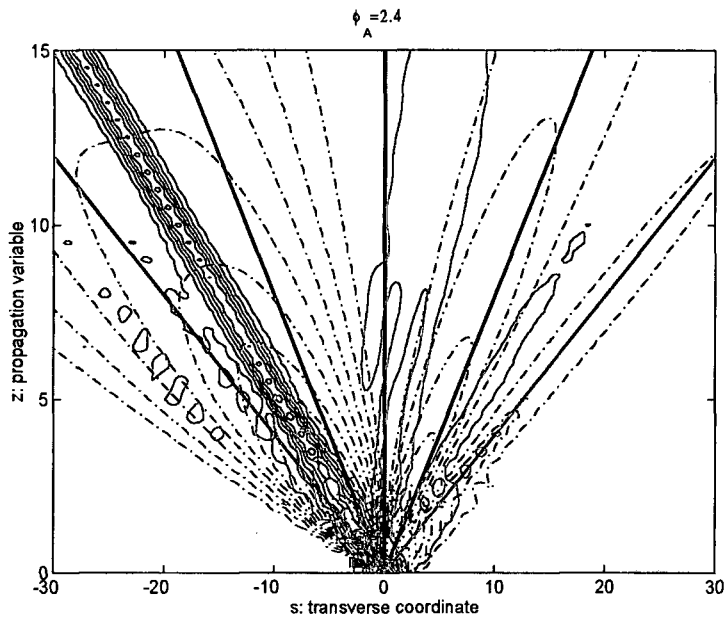
Figure 6-43: Same as in previous figure but for $\phi_A = 2.4$.

the many subbeams walks the z axis off will be given by the total momentum and the total energy following as it was derived in (6.3)

$$v = \frac{\mathcal{J}}{I},$$ (6.22)

and in turn the total momentum steams from the phase modulation according to

$$\mathcal{J} = \frac{1}{2} \int \left(2U_1^2 \phi_{1_s} + U_2^2 \phi_{2_s} \right) ds.$$ (6.23)

Assuming that the fields are launched perpendicular to the grating and that they lack any transverse phase modulation, ϕ_{1_s} and ϕ_{2_s} are due to the effect of the grating only so that

$$\phi_{i_s} = \phi_{A_i} 2\pi p_i \cos \left(2\pi p_i s + \theta_i \right),$$ (6.24)

and

$$U_i = |a_i \left(s, \xi = 0 \right)|.$$ (6.25)

The momentum thus in generic form reads

$$\mathcal{J} = -2\phi_{A_1} \pi p_1 \int U_1^2 \cos \left(2\pi p_1 s + \theta_1 \right) ds - \phi_{A_2} \pi p_2 \int U_2^2 \cos \left(2\pi p_2 s + \theta_2 \right) ds.$$ (6.26)

As a trade off between practical utility and feasibility and good performance characteristics the results shown here correspond to three basic setups presented in Figure 6-45, which will be referred to as *only FF*, *FF+SH* and *only SH* signifying which are the harmonics who get the phase modulation with the particularity in the first situation that the other harmonic is not even provided. Recall that the configuration where only the second harmonic gets the phase modulation could more efficiently be constructed by exploiting a selective in frequency photorefractive effect but for the sake of a more graphical displaying the fundamental and second harmonic have been distinguished in different inputs to the planar waveguide united by means of an Y-branch. The figure is completed with some simulations showing the possibility to achieve power control of the steering. In all cases the second harmonic is considered a weak beam as compared with the fundamental or it is not even provided, which leads to consideration

225

of positive wavevector mismatch configurations.

The expected velocity of the beams is obtained by calculating the momentum for each specific configuration

$$\mathcal{J}_{onlyFF} = 2\phi_A \pi p \int U_1^2 \cos\left(2\pi p s + \theta\right) ds, \tag{6.27}$$

$$\mathcal{J}_{FF+SH} = 2\phi_A \pi p \int \left(U_1^2 + U_2^2\right) \cos\left(2\pi p s + \theta\right) ds, \tag{6.28}$$

$$\mathcal{J}_{onlySH} = \phi_A \pi p \int U_2^2 \cos\left(2\pi p s + \theta\right) ds. \tag{6.29}$$

For the sech-like beams considered in the simulations, namely

$$U_1 = A_1 Sech\left(s\right), \tag{6.30}$$

$$U_2 = A_2 Sech\left(s\right), \tag{6.31}$$

the expected velocities in each case are

$$v_{onlyFF} = \phi_A \pi p \int Sech^2\left(s\right) \cos\left(2\pi p s + \theta\right) ds, \tag{6.32}$$

$$v_{FF+SH} = \phi_A \pi p \int Sech^2\left(s\right) \cos\left(2\pi p s + \theta\right) ds, \tag{6.33}$$

$$v_{onlySH} = \frac{\phi_A \pi p A_2^2}{2A_1^2 + 2A_2^2} \int Sech^2\left(s\right) \cos\left(2\pi p s + \theta\right) ds. \tag{6.34}$$

6.3.3 Numerical experiments

First and second configurations as featuring a total independence of the transverse velocity upon the initial amplitudes do not provide any chances for the power control of the steering if both total momentum and total power in the system are perfectly conserved. Difficulties in reaching the stationary amplitude relation when only launching the fundamental produce some energy losses which due to the asymmetric phase profile imposed, mainly have transverse direction to the right so that both the reduction of total energy and the increase in the total momentum finally carried by the soliton as a consequence of asymmetric radiation thus produced cause its speeding up towards the left. The effect is more pronounced for big values of the initial

226

away from the stationary amplitude values and hence the slight shift observed in Figure 6-45, top row. The launching of the second harmonic as approaching the stationary values favours the coupling of energy into the steered soliton while reducing the chances for power steering control as seen in the plots in middle row.

Actual power steering control is therefore only achieved in third configuration with peak deviations that reach 7 beam widths and power efficiencies on the 80% range (Figure 6-46). The recurrent trade-off between maximum deviation and energy coupled to the soliton is also here evident.

Because the calculated transverse velocities display explicit dependence upon the parameters of the grating, i.e. p and ϕ_A, the three configurations are in principle eligible for constituting the basis for the building of setups in which the steering control in achieved by means of a *switchable grating.*

Concerning optimum values of these two parameters, since the dependence upon ϕ_A is purely proportional, for maximizing beam deviation one should want it to be as large as possible. On the other side though, is energy lost during the evolution towards the stationary state which is expected to grow. On the search for an optimum value it is useful to resort to the splitting up linear picture (Figure 6-41). Negative sign for the amplitude of the straight beam above $\phi_A \simeq 2.4$ as hindering the coupling of energy at the right hand side of the profile to the soliton formed to the left produces an increase in radiation to the right which both enhances the soliton deviation and reduces energy efficiency, just as the curves in Figure 6-47 show.

More complicated is the dependence upon the spatial frequency of the grating as appearing also inside the integral. That an optimum value should exist is clear considering the sketch in Figure 6-48.

Starting from a very low spatial frequency such that in the transverse interval corresponding to relevant field amplitudes the phase modulation is viewed as a simple tilt, the calculated transverse velocity increases as the spatial frequency does as in the pure linear tilt case provided the most relevant part of the amplitude profile is sensible only to the negative slope of the phase modulation. As the spatial frequency is increased till a portion of positive slope enters the transverse area for relevant field amplitudes, the momentum should start to decrease.

For calculating such an optimum spatial frequency value find the derivative of the expression

for the transverse velocity with respect to p and equate to zero to get

$$\int Sech^2(s)\left(\cos\left(2\pi ps\right) - 2\pi p \sin\left(2\pi ps\right)\right) ds = 0. \tag{6.35}$$

This expression may be simplified using

$$\cos\left(x\right) - x\sin\left(x\right) = \sum_{n=0}^{\infty}\left(-1\right)^n x^{2n}\frac{2n+1}{(2n)!}, \tag{6.36}$$

to give

$$2 + \sum_{n=1}^{\infty}\left(-1\right)^n \frac{2n+1}{(2n)!}\left(2\pi p\right)^{2n}\int Sech^2(s)\,s^{2n}ds = 0. \tag{6.37}$$

The ntegrals are found in the tables

$$\int Sech^2(s)\,s^{2n}ds = 2\left(2^{2n}-2\right)\left(\frac{\pi}{2}\right)^{2n}|\mathcal{B}_{2n}|, \tag{6.38}$$

together with the property of Bernouilli numbers

$$\mathcal{B}_{2n} = \left(-1\right)^{n-1}|\mathcal{B}_{2n}|. \tag{6.39}$$

Finally one obtains

$$1 - \sum_{n=1}^{\infty}\left(2^{2n}-2\right)\frac{2n+1}{(2n)!}\left(\pi^2 p\right)^{2n}\mathcal{B}_{2n} = 0 \tag{6.40}$$

By using Boltzano approximation considering up to 10 terms in the summation, an optimum value for the spatial frequency of the grating of $p \simeq 0.19$ was obtained. Good accuracy of the result was confirmed as further additions of terms of the summation modified the result at the order of the third decimal digit.

The results in Figure 6-49 confirm the expectations for steering control with switchable gratings, featuring a broad scanning range of about 20 beam widths for first and second configurations and around 5 beam widths in third configuration with energy efficiencies of about 80%. Some examples of fields outputs obtained are shown in Figure 6-50.

Therefore if for power control of the steering the use of third configuration is advised, when considering a switchable grating first and second configuration should be the choice for a greater

range of angle scanning at the output of the waveguide.

Finally tolerances upon eventual variations of the wavevector mismatch or presence and variation of a certain Poynting vector walk-off are briefly outlined with the aim of demonstrating the robustness of the steering method here analyzed and its eligibility for constituting the basis of practical setups, Figures 6-51, 6-52.

As the expected velocity as given by (6.22) only depends upon conserved quantities, the wavevector mismatch dependence of the steering is determined by the behavior of radiation. Thus, in top row of Figure 6-51 as only the fundamental field is launched, for moderate β values the increase in $I_1/I_2|_{STAT}$ eases the initial momentum keeping and increases the steering with energetic solitons. The exception are the $\beta = 0$ and $\beta = 10$ cases in which the enhancement of the steering seems to come from prevailing radiation to the right as low energetic solitons are produced.

Even when amplitude values close enough to the stationary ones are supplied in the third setup considered, radiation is produced due to asymmetric $\Delta\phi$ transverse distribution caused by only the second harmonic to feel the phase distortion introduced by the input grating, hence the soliton shifts displayed in bottom row.

In middle row instead, since both fundamental and second harmonic fields are launched with amplitude values and relative phase values that ressemble the stationary ones, little effect of radiation leads to almost independence of the soliton position with respect to the wavevector mismatch value in the configuration.

As about presence of a certain Poynting vector walk-off as adding a new term for the expected velocity with respect to (6.22), namely

$$v = \frac{\mathcal{J}}{I} - \delta\frac{I_2}{I},$$

(6.41)

basically the tendency displayed is some deviation to the left when $\delta > 0$ and to the right when $\delta < 0$.
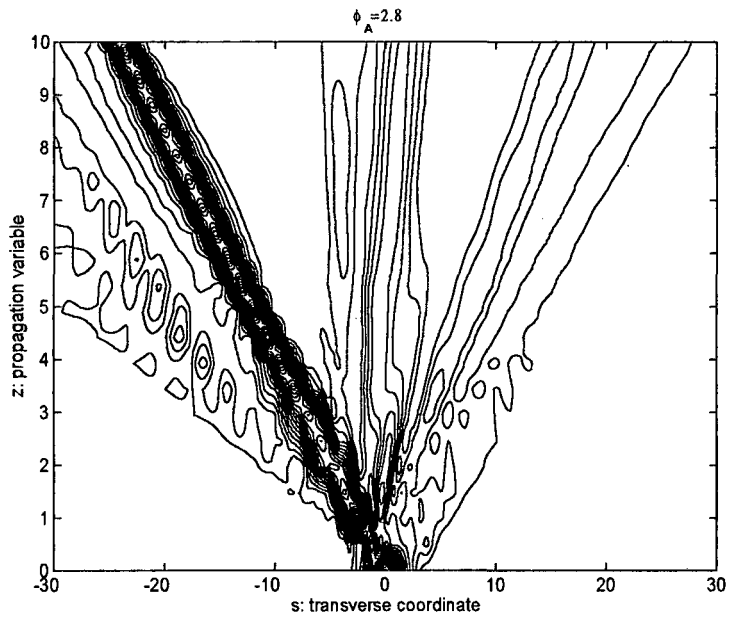
229

$\phi_A = 2.8$

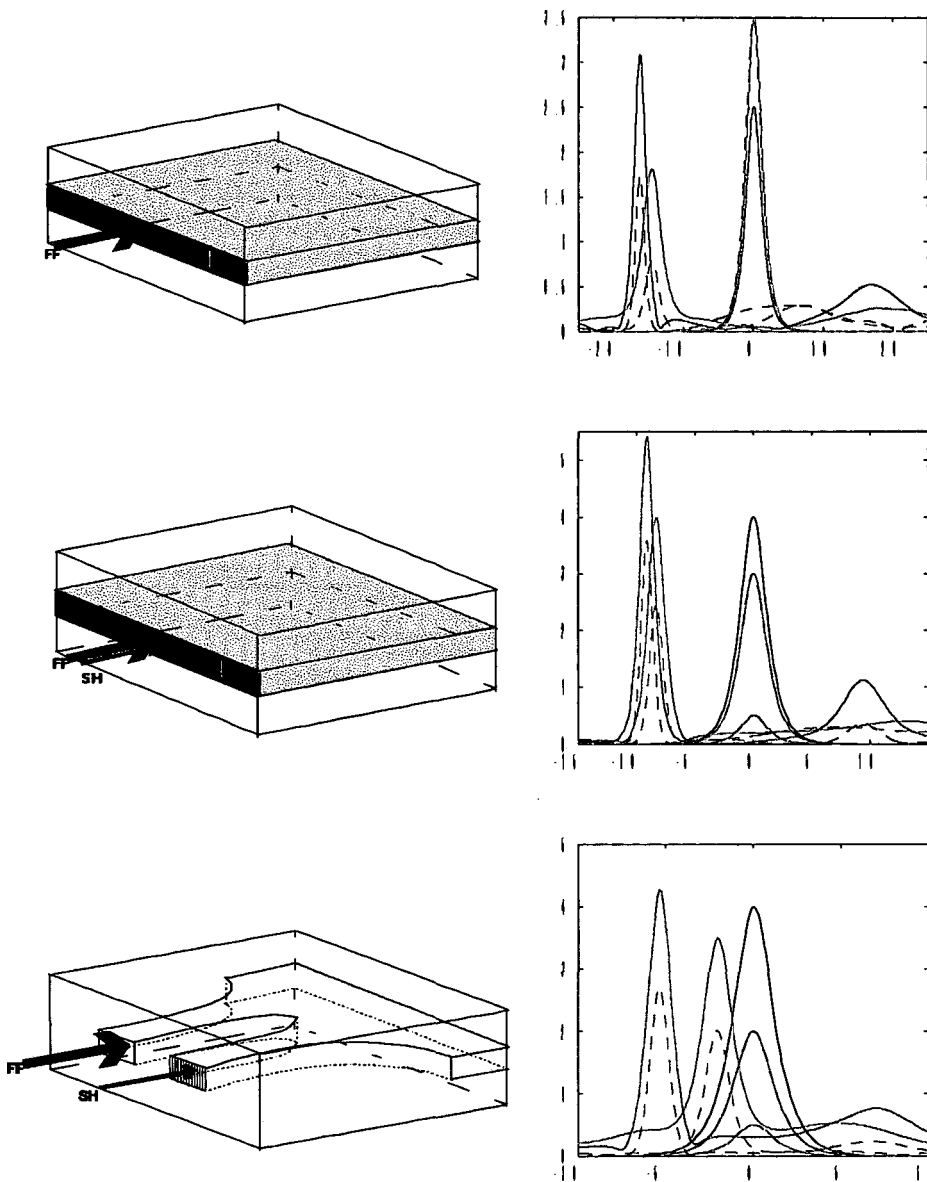Figure 6-44: Same as in Figure 6.42 but for $\phi_A = 2.8$.

Figure 6-45: Sketchs of the three different setups considered in this section along with some simulations showing power controlled steering with $\beta = -3$. The input amplitudes in each case are given by the corresponding black asn colored lines with (-) for FF and (- -) for the SH.
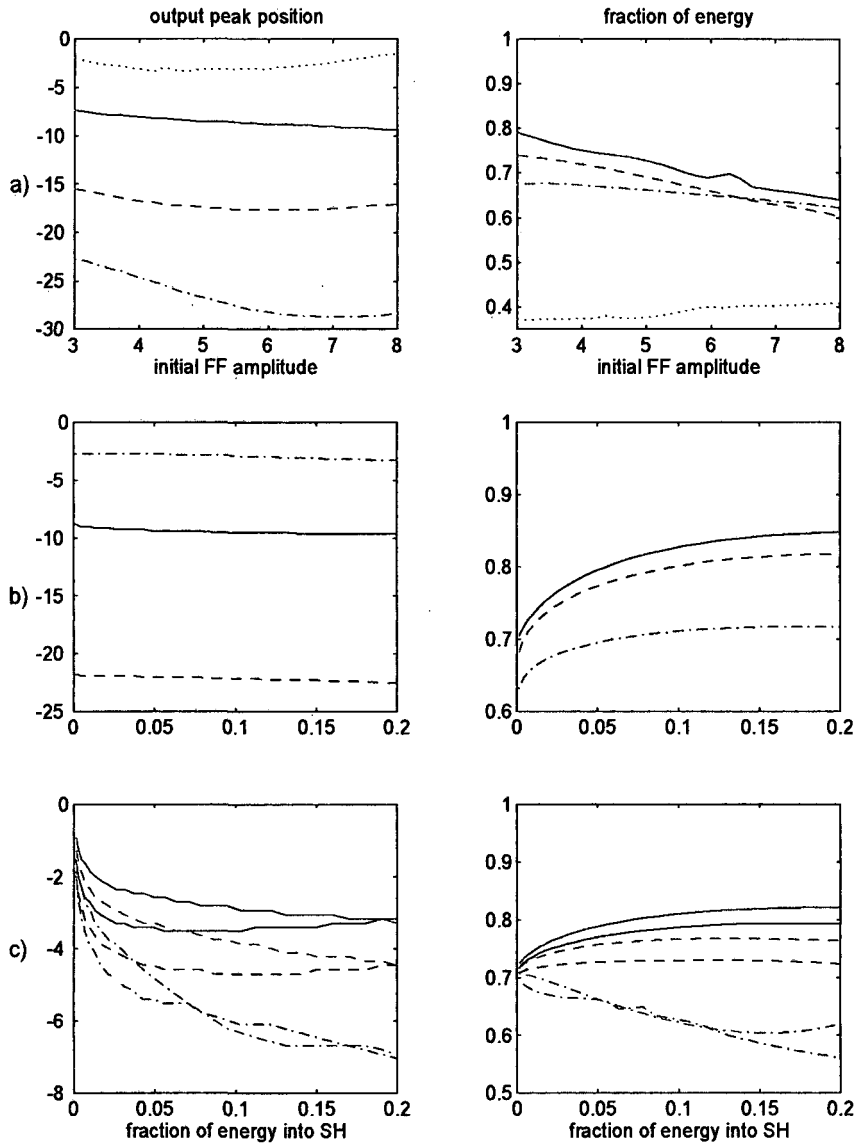
Figure 6-46: Peak position and fraction of energy coupled to the soliton found at the output of the 40 diffraction lengths long waveguide. $A_1 = 6$, $A_2 = 0$, $\beta = 3$, $\delta = 0$, $p = 0.2$, $\phi_A = 2.4$ unless stated otherwise. a) only FF case: (-): $\phi_A = 0.5$, (- -): $\phi_A = 1.2$ (-.): $\phi_A = 1.5$ and (:): $p = 0.6$, $\phi_A = 1$; b) FF+SH case: (-): $\phi_{A_2} = 2\phi_{A_1} = 1$, (- -): $\phi_{A_2} = 2\phi_{A_1} = 2.4$, and (-.): $p = 0.6$, $\phi_{A_2} = 2\phi_{A_1} = 1$; c) grating for SH only: ('m'-): $\phi_A = 1$, ('m'- -): $\phi_A = 1.5$ ('m'-.): $\phi_A = 2.4$; and $p = 0.6$, ('g'-): $\phi_A = 1$, ('g'- -): $\phi_A = 1.5$ ('g'-.): $\phi_A = 2.4$. Color scale as in App. B.
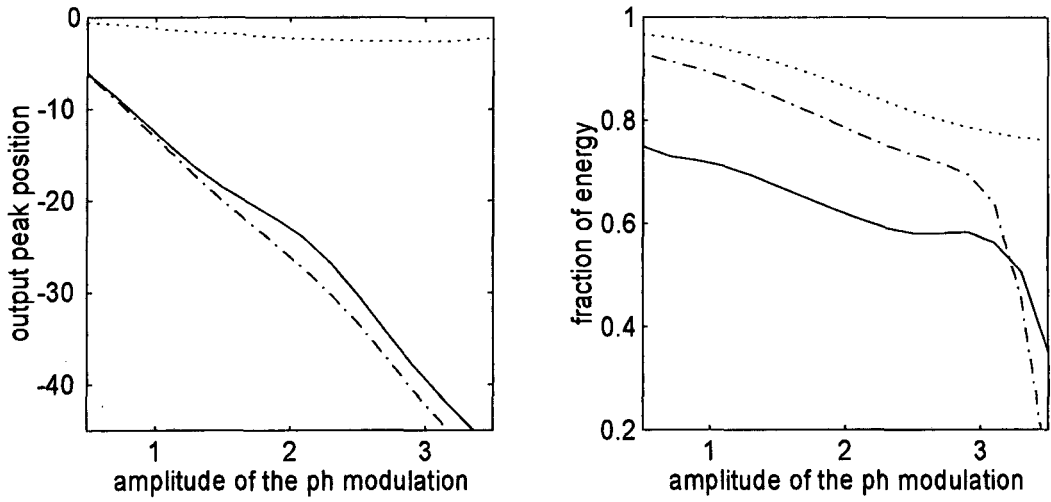
Figure 6-47: Features of the steering dependence upon the amplitude of the phase modulation. In all cases $\beta = 3$, $p = 0.2$, $A_1 = 4$. (-): *only FF* (-.): *FF + SH* $A_2 = 1$, (:): *only SH* $A_2 = 1$.
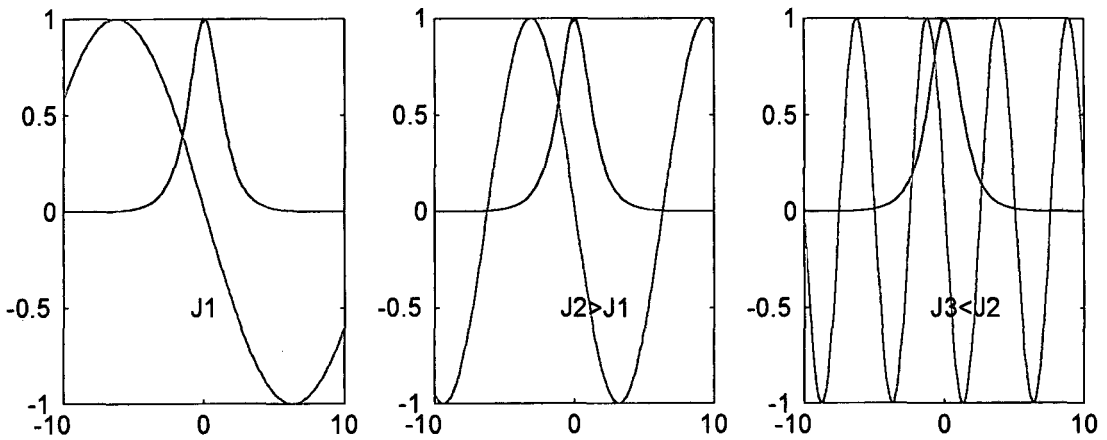
Figure 6-48: Illustrative of the dependence of the total momentum acquired by the beam on the spatial frequency of the input grating.
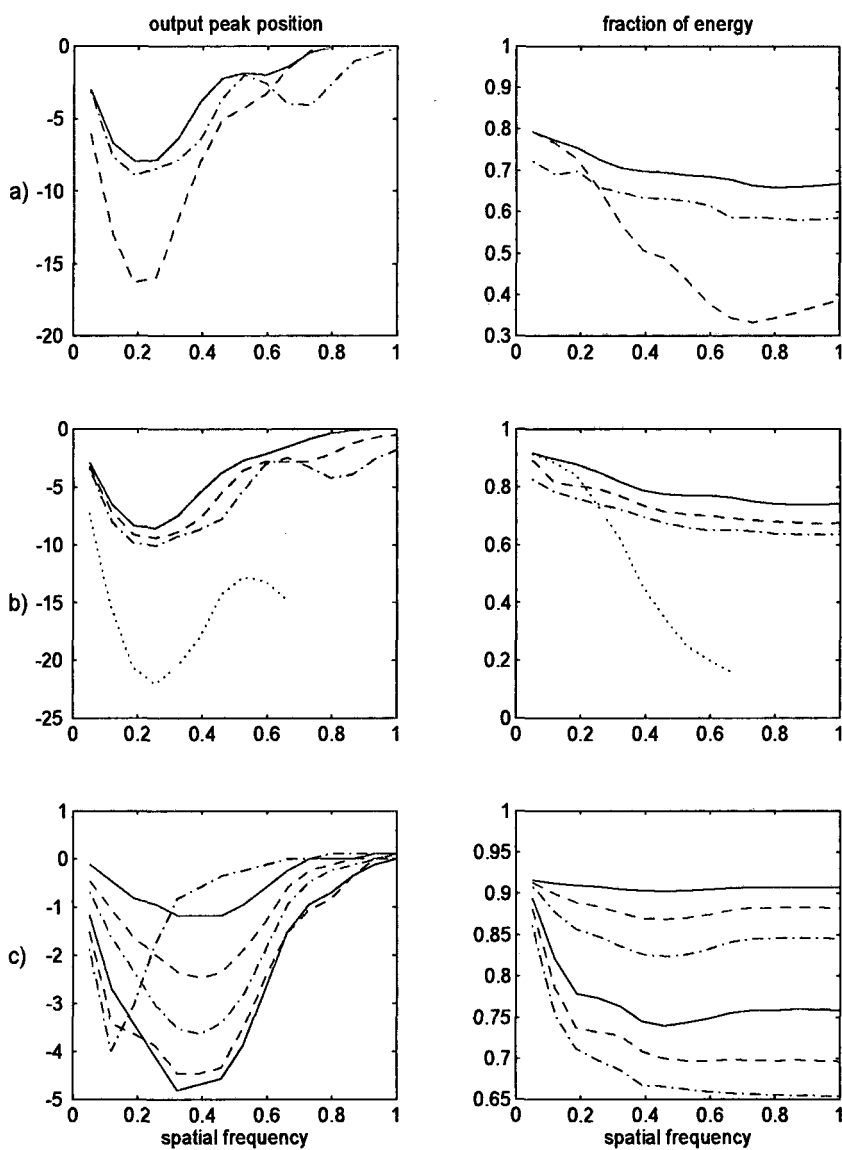
Figure 6-49: Peak position and fraction of energy coupled to the soliton found at the output of the 40 diffraction lengths long waveguide. $A_1 = 4$, $A_2 = 1$, $\beta = 3$, $\delta = 0$, $p = 0.2$, $\phi_A = 2.4$ unless stated otherwise. a) only FF input case: (-): $A_1 = 4$ $\phi_A = 0.5$, (- -): $A_1 = 6$, $\phi_A = 0.5$, (-.): $A_1 = 4$, $\phi_A = 1.5$ b) FF+SH case: $\phi_{A_2} = 2\phi_{A_1} = 1$, (-): $A_1 = 4$, $A_2 = 1$, (- -): $A_1 = 6$, $A_2 = 1.5$, (-.):$A_1 = 8$, $A_2 = 2$, and (:): $\phi_{A_2} = 2\phi_{A_1} = 1$, $A_1 = 4$, $A_2 = 1$; c) grating for SH only: ('m'-): $\phi_A = 0.5$, ('m'- -): $\phi_A = 1$, ('m'-.): $\phi_A = 1.5$ ('g'-): $\phi_A = 2.4$, ('g'- -): $\phi_A = 3$, ('g'-.): $\phi_A = 3.8$. Color scale as in App. B.
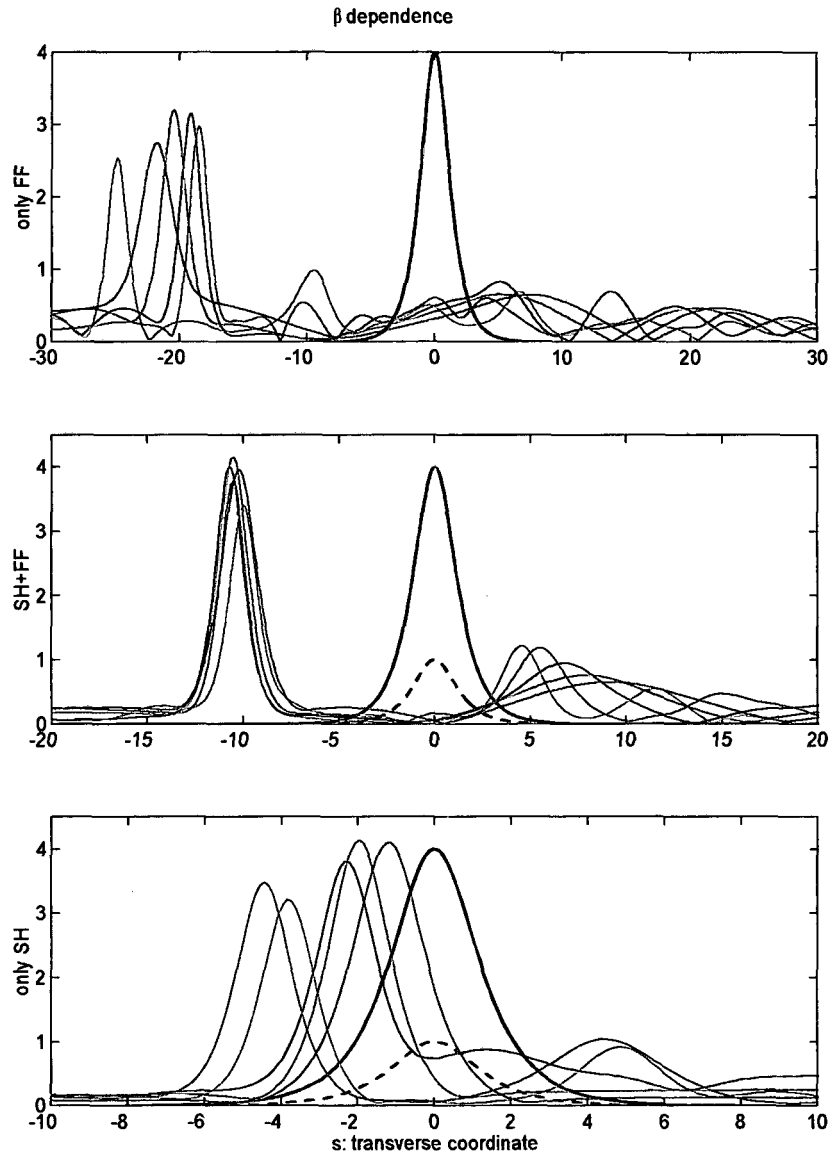
234
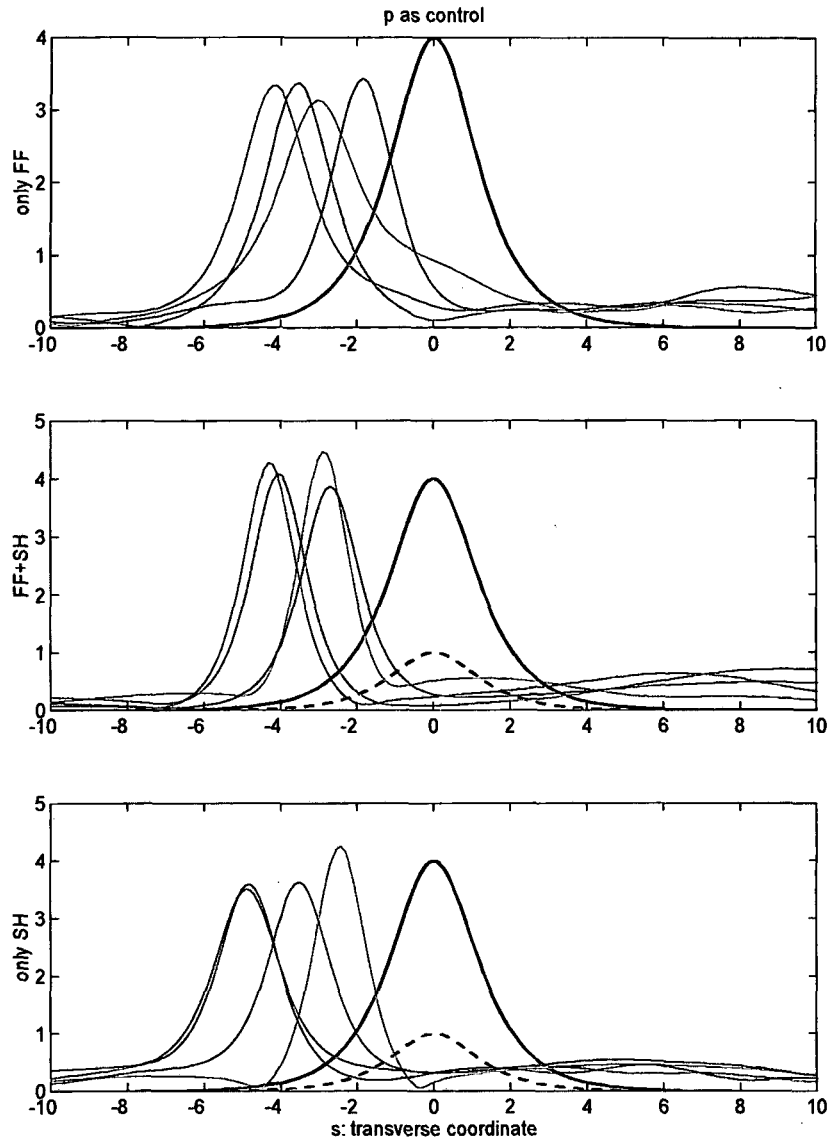
Figure 6-50: Input and outputs of a 20 diffraction lengths waveguide (40 diffraction lengths for *only SH* results) for the three setups considered showing steering control through the switchable grating. Unless stated otherwise $A_1 = 4$, $A_2 = 1$, $\beta = 3$. ('m'): $p = 0.1$, ('g'): $p = 0.2$, ('r'): $p = 0.3$, ('b'): $p = 0.4$. Top: $\phi_A = 0.5$, middle: $\phi_A = 1$, bottom: $\phi_A = 2.4$. Black thick lines show the input field amplitudes with (-) for FF and (- -) for SH. Color scale as in App. B.
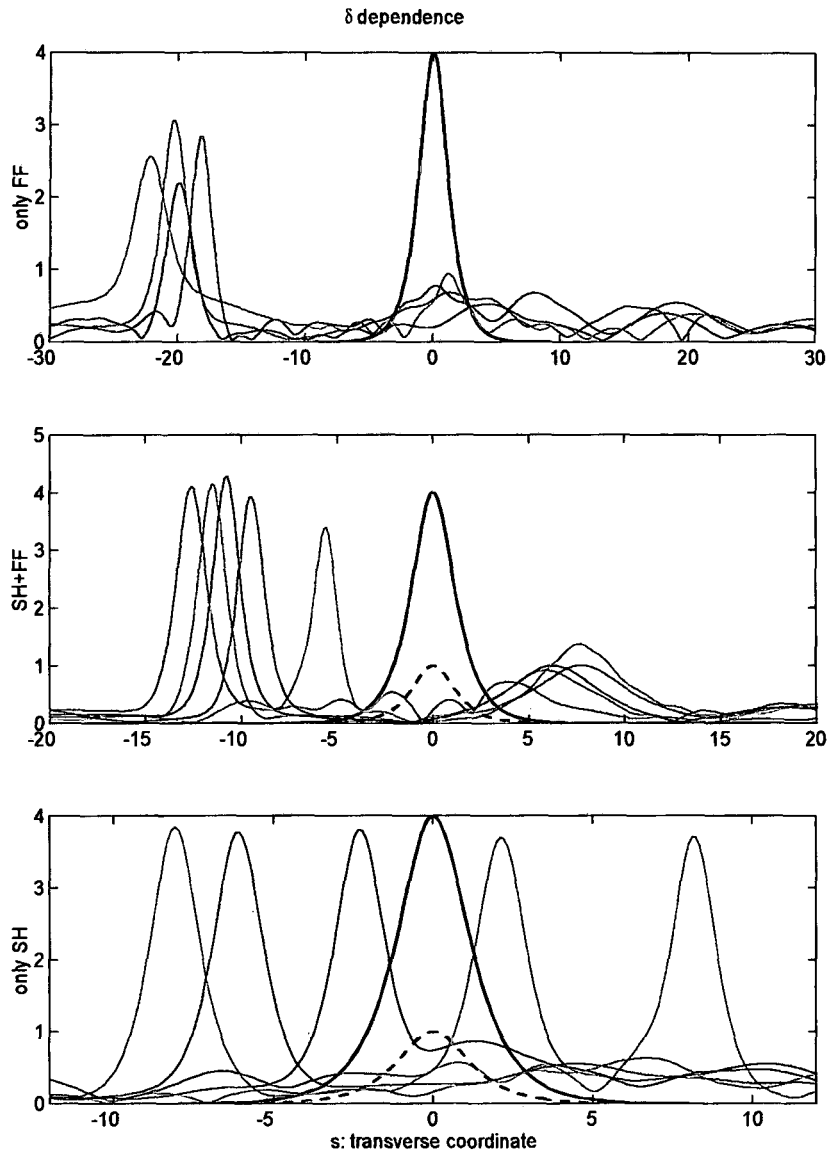
Figure 6-51: Input and outputs of a 20 diffraction lengths waveguide (40 diffraction lengths for *only SH* results) for the three setups considered showing dependences of the steering effect upon the wavevector mismatch. Unless stated otherwise $A_1 = 4$, $A_2 = 1$, $p = 0.2$, $\phi_A = 2.4$. ('m'): $\beta = 0$, ('g'):$\beta = 1$, ('bk'): $\beta = 3$, ('r'): $\beta = 6$, ('b'): $\beta = 10$. Black thick lines show the input field amplitudes with (-) for FF and (- -) for SH. Color scale as in App. B.

Figure 6-52: Input and outputs of a 20 diffraction lengths waveguide (40 diffraction lengths for *only SH* results) for the three setups considered showing dependences of the steering effect upon the wavevector mismatch. Unless stated otherwise $A_1 = 4$, $A_2 = 1$, $p = 0.2$, $\phi_A = 2.4$. $\beta = 3$ ('m'): $\delta = -1.5$, ('g'): $\delta = -1$, ('g'): $\delta = -0.5$, ('bk'): $\delta = 0$, ('c'): $\delta = 0.5$, ('r'): $\delta = 1.5$. Black thick lines show the input field amplitudes with (-) for FF and (- -) for SH. Color scale as in App. B.

6.4 Power dependent splitting

The complicated dynamics undergone by fundamental and second harmonic fields once launched into the quadratic material determines under certain circumstances total beam break up of the input beams. That effect already outlined in section 3.6.3 will in the present section be analyzed in detail. Beam break up produced by initial $\phi_0 = \pi$ differences was already explained section 6.2 and therefore the present section shall concentrate on splitting encountered with in phase input beams.

Along with extensive numerical simulations demonstrating the effect, a simple picture that qualitatively describes the mechanism causing the splitting and elucidates dependences upon system and input parameters is derived. Emphasis is lied in practical application building aspects and some hints to the design of practical setups that exploit the properties of the splitting effect are given.

Recalling the analysis of the dynamics in section 3.6.3, when launching into the waveguide bright profiles whose peak values for each harmonic resemble those for the stationary solution, since initially nonlinear interaction prevails over diffraction, the beams peak will reach the $\Delta\phi \sim 0$ nonlinear phase locking around a local energy value which is higher than required taking into account the total energy contained in the beam in other words, the locking is achieved with a transverse characteristic that is sharper than the one of the stationary solution corresponding to the value of the peaks. That causes the beams to evolve into an oscillating state in which through the focusing and defocusing periods undergone the peak results locked to slightly higher local energy values reducing the variation in every period.

A quite distinct situation is encountered when initially diffraction prevails over nonlinear interaction. In this case the beams peak may achieve the locking $\Delta\phi \sim 0$ with local energy values which are lower than the corresponding to the total energy in the beams. The $\Delta\phi$ deviation from locking brought about during the focusing period will thus be too slowly recovered by the peak allowing during subsequent defocusing, a great deal of energy escape towards the profile tails. The locking will then take place with a lower local energy value in peak whereupon a net injection of energy towards the profile tails is set up which eventually allows for formation of two solitons at each side of the center.

For total beam break-up therefore what it is needed is an initial reduced contribution of

nonlinear interaction terms that keeps the beams peak from achieving the nonlinear phase locking long enough for significant effect of diffraction to take place.

That condition has been found to be verified either by only injecting the fundamental in which case as seen in section 3.6.2, initially $\Delta\phi \sim -\pi/2$ so that, in $\Delta\phi_\xi$ only linear terms are relevant, recall (3.88)

$$\Delta\phi_\xi = \frac{U_{1ss}}{U_1} - \frac{1}{4}\frac{U_{2ss}}{U_2} + 2U_2\cos(\Delta\phi) - \frac{U_1^2}{U_2}\cos(\Delta\phi) + \beta = 0, \qquad (6.42)$$

or else by injecting a very weak fundamental beam whereupon a very small $U_1^2 U_2$ product reduces the initial energy exchange velocity and hence that of nonlinear phase matching achievement.

Further initial detachment form phase locking condition takes place in the first case when a negative β is considered, whereas in second case since energy exchange from second harmonic to fundamental is required and then $\Delta\phi > 0$, the splitting is found in positive β configurations. See the examples in Figure 6-53.

The first case, i.e. exclusive injection of the fundamental field, characterized by initial total absence of nonlinear interactions (see (6.42)), is the one allowing for splitting in $\beta = 0$ configurations whereas contribution of the third term in (6.42) eases quick peak equilibrium recovering and avoids splitting. The position of peaks found at the output of a 40 diffraction lengths waveguide along with the energy coupled to each beam is plotted in Figure 6-54 showing neat three soliton formation with little losses due to radiation and a neat switching effect around $A_1 \sim 5.5$ corresponding to a normalized power of about $I \sim 60$.While the fields evolution in Figure 6-53 c) seems to clearly respond to the splitting mechanism just explained, the quick and well defined beam separation in d) seems to be due to a different effect.

The splitting shown in 6-53 c) which will be generically referred to as *smooth splitting* occurs between two energy bounds and for low $|\beta|$ values following the mechanism explained above, see Figures 6-57-6-58. The lower energy bound can intuitively be connected with quick enough phase locking condition reaching in center so that it occurs in the period when diffraction prevails over nonlinear interaction. As energy is increased, nonlinear interaction can be fast enough so that it manages to counterbalance diffraction before the locking takes place thus
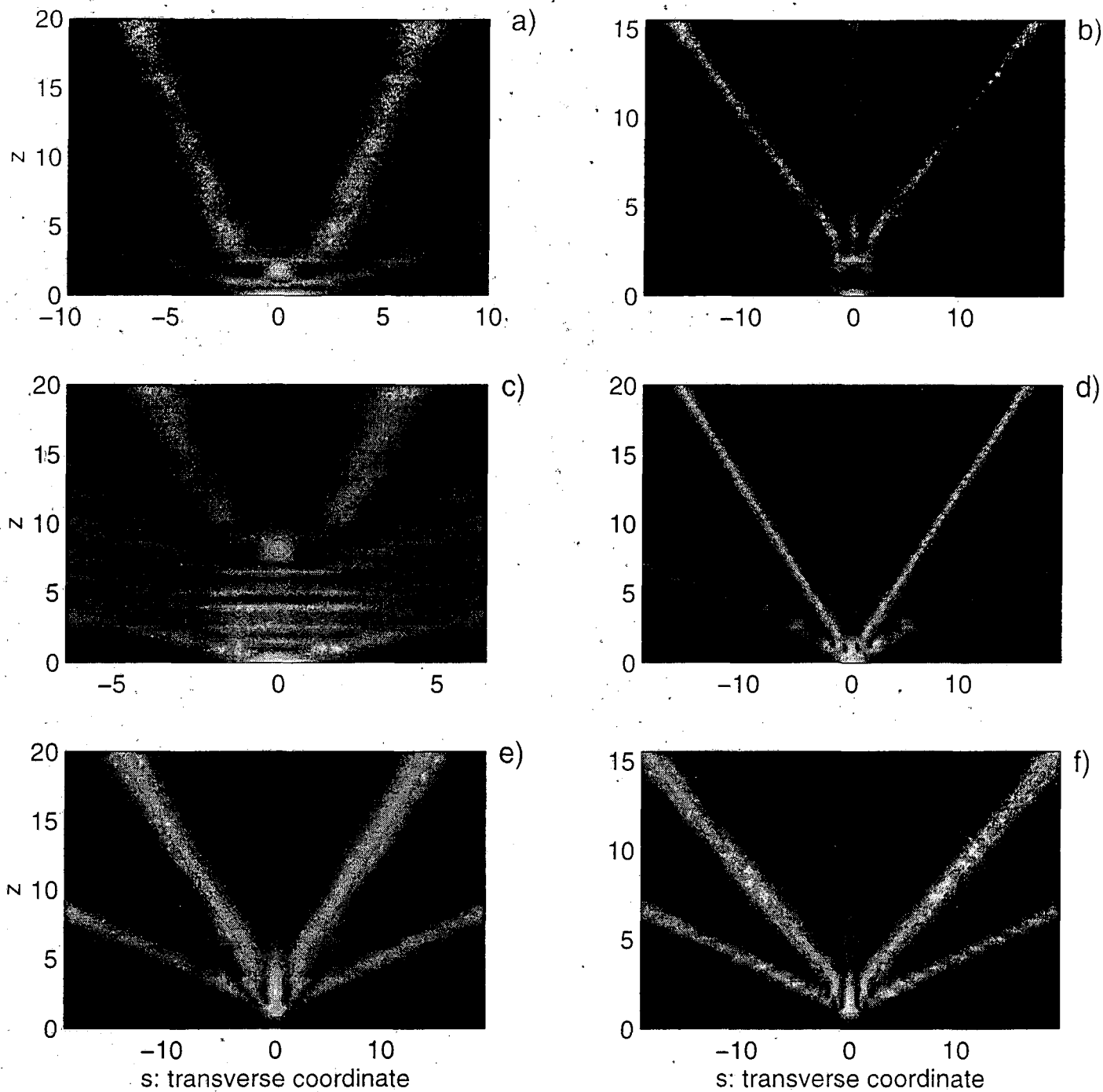
Figure 6-53: Examples of beam splitting. In all cases the fundamental beam evolution is shown. a) $\beta = -1$, $A_1 = 6.5$, $A_2 = 0$; b) $\beta = 0$, $A_1 = 5$, $A_2 = 0$; c) $\beta = -2$, $A_1 = 6.5$, $A_2 = 0$; d) $\beta = -2$, $A_1 = 10$, $A_2 = 0$; e) $\beta = 3$, $A_1 = 0.1$, $A_2 = 4$; f) $\beta = 6$, $A_1 = 0.1$, $A_2 = 6$.

preventing the splitting for power values above a certain threshold.

The splitting occurring for higher $|\beta|$ values and high input powers and that gives rise to great separation between the two solitons produced at the very firsts steps of the propagation, hereafter referred to as *sharp splitting*, can be shown to respond to a somewhat different mechanism which involves consideration of lateral bumps creation which was discussed in the dynamics section. See Figures 6-55-6-56.

For very high $|\beta|$ values as strongly determining a $\Delta\phi$ value monotonic evolution, even transverse points containing significant amounts of local energy are likely to get stuck around a $\cos(\Delta\phi) < 0$ area whereupon the nonlinear negative contribution to the phases causes the energy in those points to result washed away towards other transverse points in the profile. This effect is related to the increase of radiation produced as a consequence of larger difference between the stationary solution and the initial conditions considered here as the $|\beta|$ value is increased.

For high energy values, too sharp transverse profile stationary solution requirements for peak, further desequilibrated from its phase locking condition due to energy dragged from amplitude valley, hinders balanced oscillation state formation in center. On the other hand in the profile 'tails' where the energy received from the amplitude valley is helping to achieve the phase locking condition, as featuring lower peak amplitude values, the stationary solution transverse profile requirements result greatly loosened down so that they more easily form a soliton.

The differences between the two classes of splitting are evidenced in Figures 6-59 and 6-60 featuring the $\Delta\phi$ evolution in a transverse point close to center for smooth and sharp splitting cases. The plots show that sharp splitting is characterized by significant injection of energy into the peak taking place when fairly close to center profile points undergo $\cos(\Delta\phi) < 0$ values which immediately and unrelentlessly lead to the splitting.

One might think then that if energy is increased further even half the energy alloted to each lateral bump should require too sharp and hence each lateral bump must split up into other two as it is actually also seen to happen, Fig. 6-55.

Despite being produced through a quite messy dynamics evolution with energy being struggled back and forth between wings and center, fairly neat solitons emerge from the beam

241

breaking up with detachments from center that go from 5 to 20 beam widths. Energy efficiencies are within reasonable ranges, in all cases about 30% of the input energy is alloted to each soliton, allowing to think in interesting practical applications.

The effect for negative β of a weak slightly tilted signal beam was investigated yielding the result in Figure 6-61 As seen, both the number of solitons produced as well as the energy coupled to each can be controlled through control of the tilt angle of the small second harmonic signal.
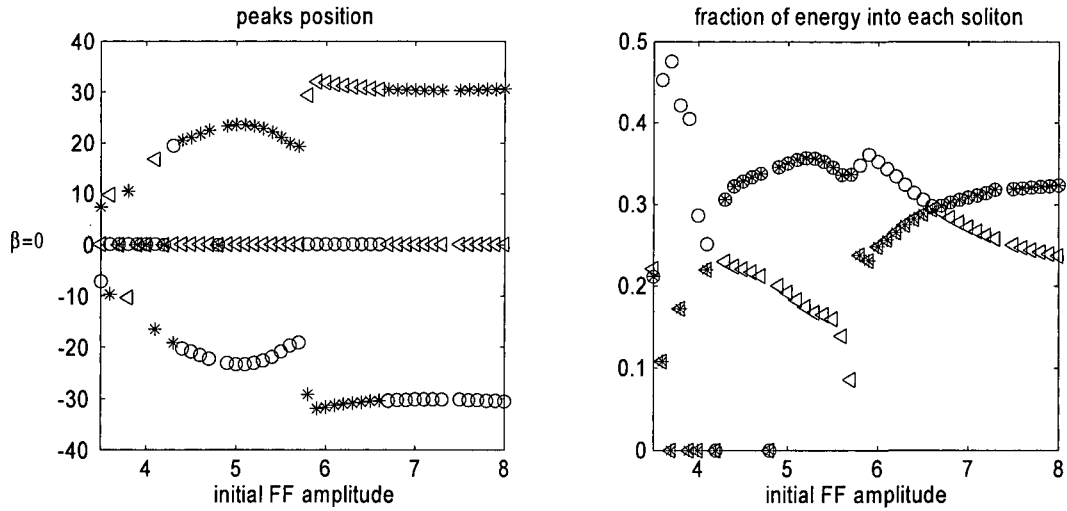
Figure 6-54: Position of the peaks found at the output of a 40 diffraction lengths waveguide (left) and fraction of input energy coupled to it (right) as a function of the input fundamental amplitude. Here $\beta = 0$ and the second harmonic is not provided, i.e. $A_2 = 0$.
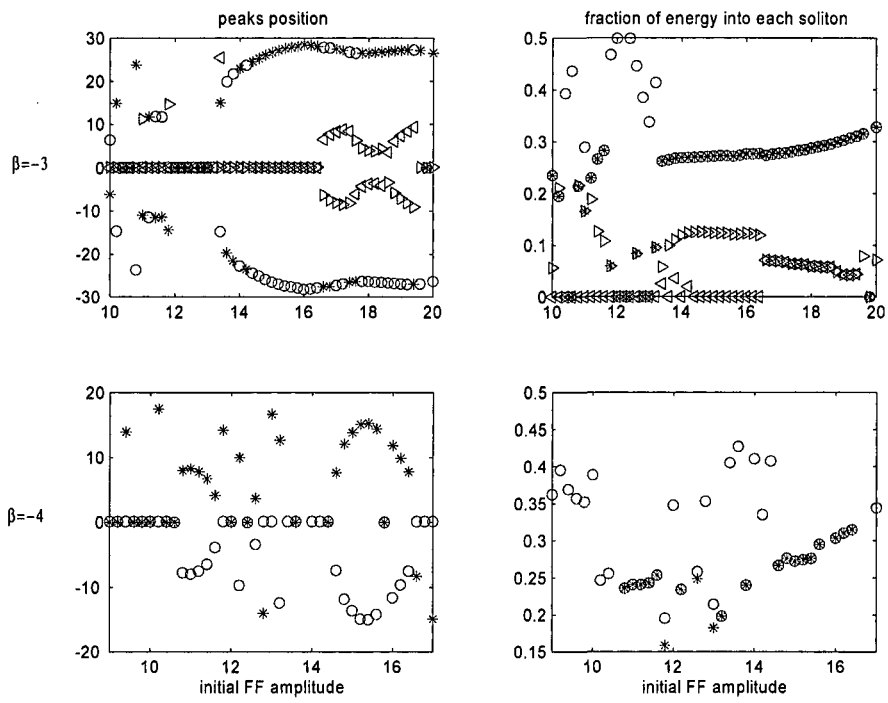
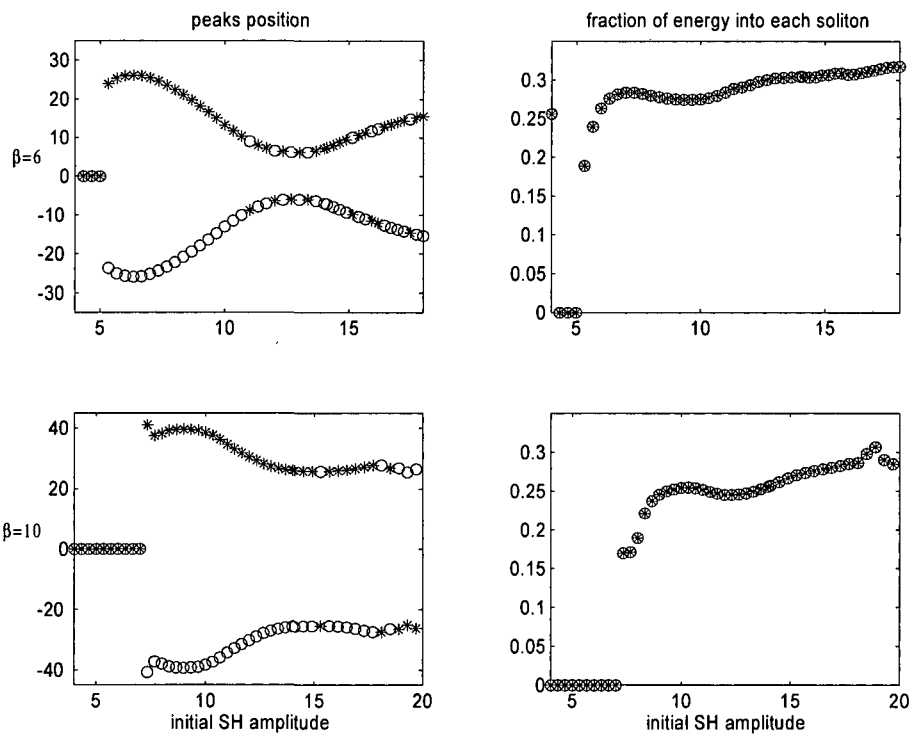Figure 6-55: Same as Figure 6-54 but for $\beta = -3$ (top) and $\beta = -4$ (bottom).

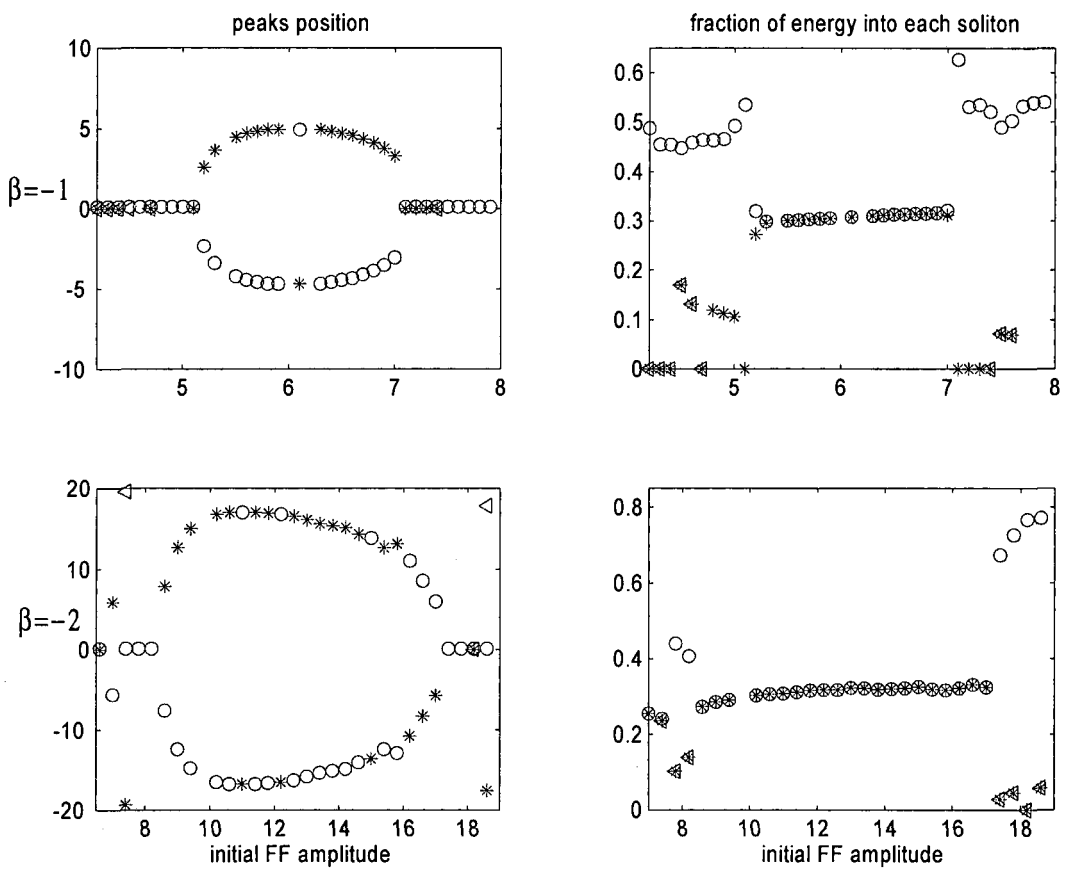Figure 6-56: Same as Figures 6-54 but for $\beta = 6$ (top) and $\beta = 10$ (bottom).

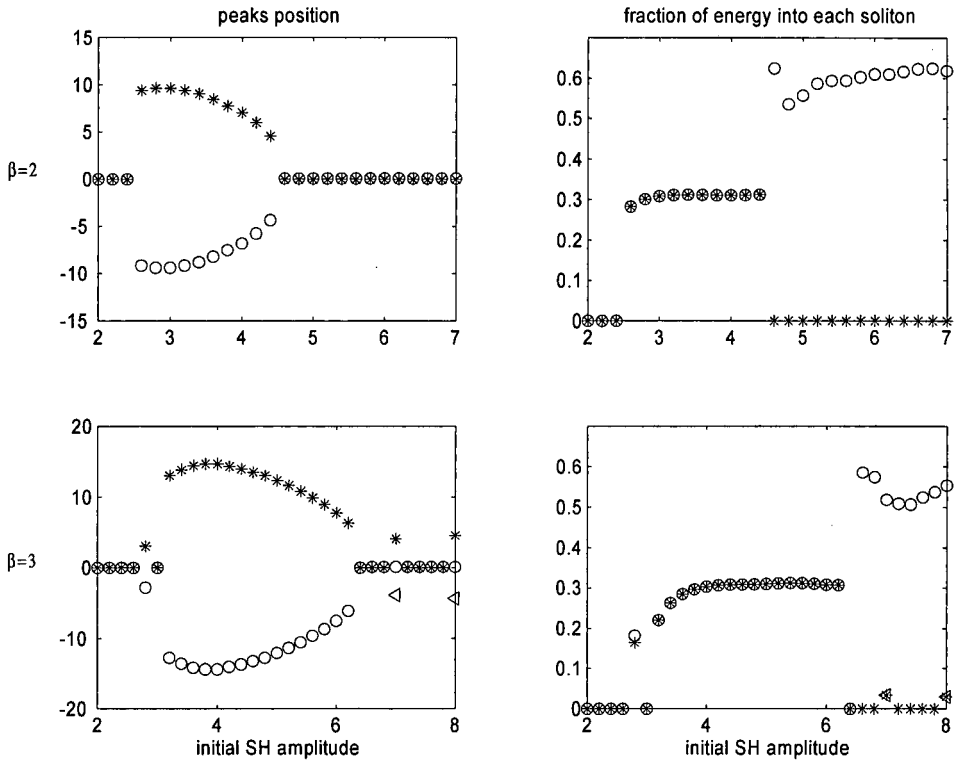Figure 6-57: Same as Figure 6-54 but for $\beta = -1$ (top) and $\beta = -2$ (bottom).

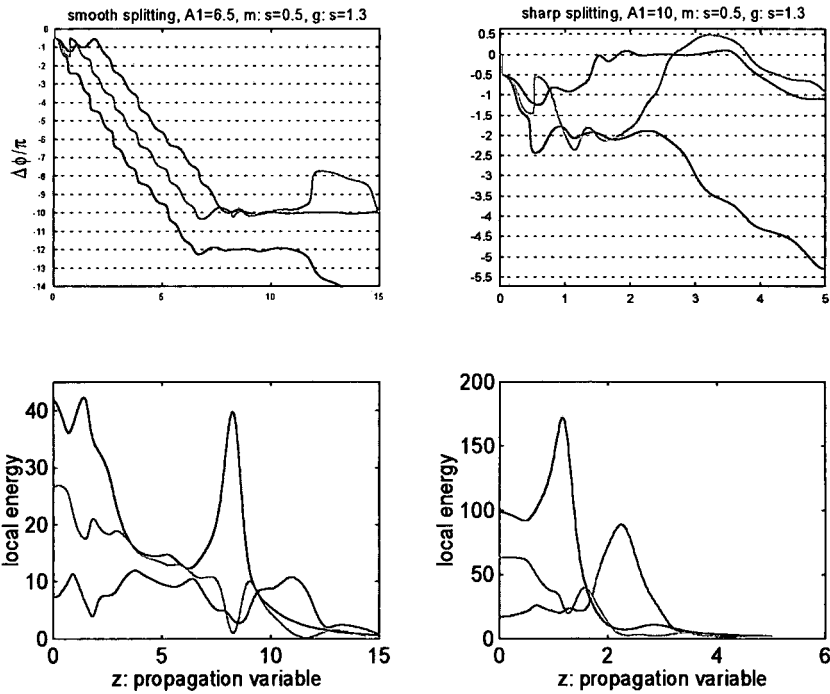Figure 6-58: Same as Figures 6-54 but for $\beta = 2$ (top) and $\beta = 3$ (bottom).

Figure 6-59: Nonlinear phase mismatch and local energy evolution, top and bottom rows respectively, in different transverse points: ('bk'): peak; ('m'): $|s| = 0.5$; ('g'): $|s| = 1.3$; illustrating the differences between smooth and sharp splitting, respectively at left $A_1 = 6.5$, and at right $A_1 = 10$. In all cases $\beta = -2$, $A_2 = 0$. Color scale as in App. B.
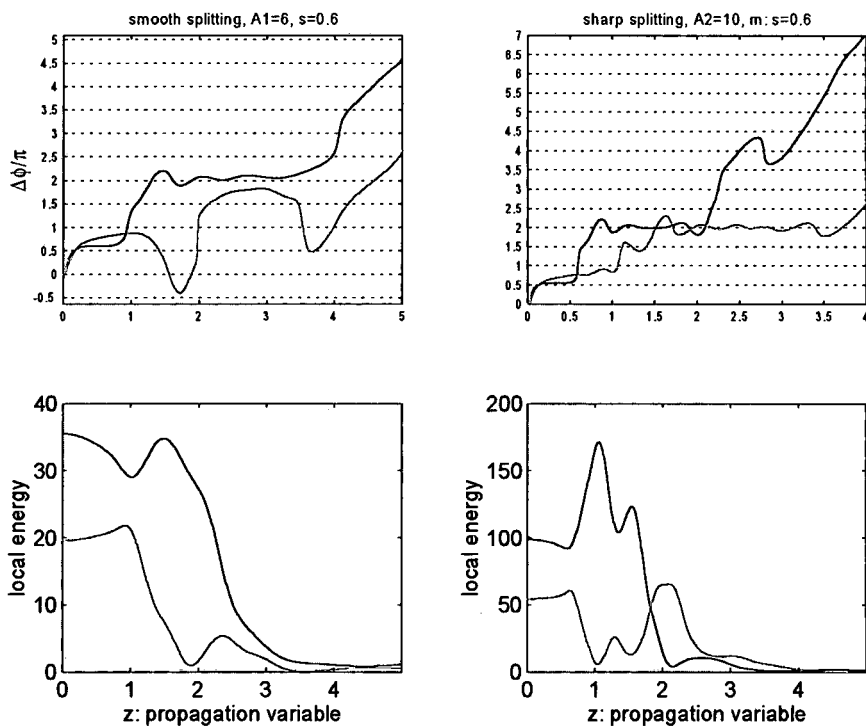
Figure 6-60: Same as in previous figure but for ('bk'): peak; ('m'): $|s| = 0.6$. Smooth splitting at left, $A_2 = 6$, and sharp splitting at right, $A_2 = 10$. In all cases $\beta = 6$, $A_1 = 0.1$.
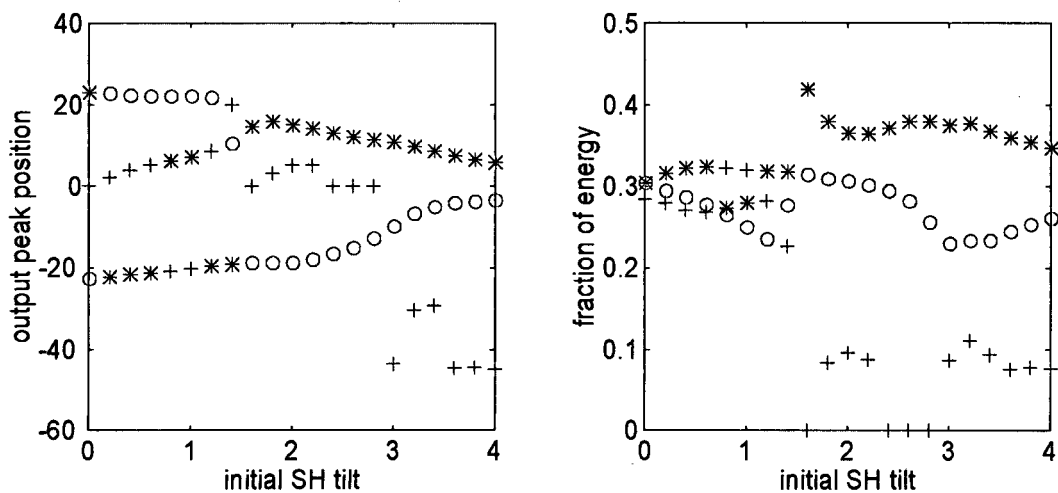

Figure 6-61: Peaks position (left) and energy coupled to each peak (right) for different values of an initial tilt imposed on a weak second harmonic beam. Parameters are $\beta = -1$, $A_1 = 6$ and $A_2 = 0.5$.